Image processing-based techniques for process parameter characterization in Plasma Transferred Arc Additive Manufacturing (PTA-AM) process

by

Raviraj Gajbhiye

A thesis submitted in partial fulfillment of the requirements for the degree of

Master of Science

Department of Mechanical Engineering

University of Alberta

Abstract

The plasma transferred arc additive manufacturing (PTA-AM) process is a recently established additive manufacturing (AM) technique for manufacturing large parts for the resource industries. In the PTA-AM process, the build quality of the 3D part is governed by various processing parameters, including but not limited to plasma arc current, stand-off distance (SOD) and powder flow rate. The PTA-AM is challenging for in-process monitoring due to the complex interaction among the plasma arc, powder stream and substrate. Any instability in these processing parameters affects the overall build quality of the component, inducing non-conformance to geometrical properties. In the AM field, various high-speed imaging techniques are used to investigate the correlation between the processing parameter variation contributing to quality fluctuations of the final 3D product. This thesis presents the *in-situ* image processing methodologies to quantify and analyze the process aspects of the emergent PTA-AM system. Firstly, the single-track multi-layer bead deposition experiments of WC-reinforced NiCrBSi composites are carried out on a PTA-AM system and recorded with a high-speed camera. The optimized SOD has been determined from image analysis, contributing to the uniform deposition with quality deviation. The image analyzed SOD is validated with the experimentally determined SOD. This information is also used to evaluate the impact of powder variation on bead layer height. Secondly, the proposed *in-situ* image processing technique has been employed to describe the relationship between powder stream distribution and build geometry variation. In addition, the effect of plasma arc current on bead layer geometry (height and width) is also investigated. The Analysis of variance and t-tests has checked the significance of build quality dependence on powder and plasma arc variation. It is well-known that the powder flow behaviour (the particle trajectories and velocities) under the

plasma arc region is a complex but crucial physical phenomenon that affects the geometric dimensions and the bead deposition characteristics in PTA-AM. Therefore, we proposed another image processing methodology to investigate the powder stream behaviour under the influence of the plasma arc region. In the findings, variation in trajectories and impact velocities of individual powder particles due to plasma arc has been observed. Using the single-particle trajectory model, we validated that the results are within the theoretical range. Later, based on calculated impact velocities of powder particles, the parametric study was conducted to predict the spreading and solidification of molten powder particles on the substrate. Using dimensionless numbers, the parametric effect of hydrodynamic forces (Weber and Reynolds number) and thermophysical forces (Stefan and Peclet number) on the impinging melted powder particles is also studied.

Preface

This thesis is an original work by Raviraj V Gajbhiye under the supervision of Dr. Prashant R Waghmare and co-supervision of Dr. Ahmed Jawad Qureshi.

Chapter 2 of this thesis has been accepted to the peer-reviewed journal: International Journal of Advanced Manufacturing Technology for publication as "Gajbhiye R.; Rojas M.; Waghmare, P; Qureshi, A., In-situ image processing for process parameter-build quality dependency of plasma transferred arc additive manufacturing."

Chapter 3 of this thesis has been submitted to the peer-reviewed journal: International Journal of Heat and Mass Transfer for publication as "Gajbhiye R.; Qureshi, A.; Waghmare, P, Maximum spreading of molten powder particle in plasma transferred arc additive manufacturing process."

Raviraj Gajbhiye was responsible for the design methodology, conceptualization, data analysis, investigation, interpretation, and manuscript writing. Dr. Waghmare was the primary supervisory author of all the works presented here by Raviraj Gajbhiye and was involved with the conceptualization, assessment of results, manuscript editing of chapter 3 and providing the resources. Dr. Qureshi was the co-supervisory author of all the works presented here by Raviraj Gajbhiye and was involved with the conceptualization, data interpretation, analysis of the results, and manuscript editing of chapter 2. Dr. M. Rojas was involved with conducting the necessary experiments for the work.

Dedicated to –

Dr. Babasaheb Ambedkar

&

My parents: Mrs. Kausal V. Gajbhiye and Mr. Vijay C. Gajbhiye, and my elder sister Pradnya

Gajbhiye, for their innumerable sacrifices, endless love, and constant support.

Acknowledgement

I am delighted that I get this opportunity to extend sincere gratitude towards everyone who has helped me accomplish these three years of M.Sc. at the University of Alberta. This was only an upward journey for me, with many obstacles, but I could surpass them towards completing my work only due to the endless support of my supervisors, colleagues, family, and friends.

I cannot thank enough Prof. Prashant Waghmare, who gave me this opportunity and accepted me under his supervision for M. Sc. in Mechanical Engineering at UofA. His guidance was not just limited to my academic work, but it was all-around. He helped me immensely with his constant moral support, critique, and belief in me. I have had the opportunity to work under him closely and could imbibe a few of his very essential traits of professionalism, which I am sure will help me in the real world. I am very thankful for the financial support Prof. Waghmare could provide during my years as a grad student.

I extend sincere gratitude towards Prof. Ahmed Qureshi for providing me a chance to work for him in this exciting research area. It gave me a new horizon to reach academically and thereby made me confident to choose a trajectory for my career. His endless support and guidance throughout the hours of need had been very vital.

I am very thankful to the lab members who never denied help when I approached them. Many thanks to Ryan Bailey for training and guiding me with the lab equipment and for always being present for resolving queries. I am very thankful to my lab-mates, Abrar Ahmed and Sumaiya Farzana, for their time and help with the valuable guidance and suggestions in clearing out my doubts whenever I was in need. Big thanks to all the members of *i*SSELab including for their

Table of Contents

List of Tables

List of Figures

1   Introduction

Recent years have witnessed an influx of unprecedented attention for additive manufacturing (AM) due to the three key advantages: versatility of design, competence to enable mass customization, and abridging the product lead time [1]. AM process, also prevalently known as rapid prototyping or 3D printing, works on the principle of building up the cumulative layers of material to transform the computer-aided design (CAD) model into a physical component of the desired shape [2]. This concept changed the conventional approach of building the objects by removing mass through subtractive methods like CNC drilling and milling machines. Compared with conventional manufacturing (CM) processes, the benefits of AM processes can be boiled down to three aspects. First, AM can be used to make highly complex parts that are unattainable through the CM process. Second, the AM processes enhance the buy-to-fly ratio by decreasing the amount of waste material, reducing the parts' final price. Third, the AM process can substantially reduce energy consumption and protect the environment by lowering the weight of parts created due to material adaptations or innovative designs. The AM process lends itself to developing a wide range of materials, including metals, plastics, alloys, and composites. Combining these factors has led to an increase in the commercial exploitation of AM, and many sectors have begun to seize the opportunity. AM is mainly used in the aerospace, automotive, machine tool industries, medical and dental care in terms of applications. Nearly 150 companies in these fields use it [3]. Gartner publishes an annual report for the AM industry that details the hype cycle for every technology in the AM market. Over the past 25 years, revenues for all AM products and services worldwide have grown by 25.4% annually, from $295 million to $5.1 billion [4]. This growth was observed across all markets, including desktop 3D printers and industrial metal part AM. According to the estimate,

$230-550 billion could be delivered by 2025 [5]. The primary markets identified are consumer goods worth $100-300 billion and parts for medical and aerospace products worth $100-200 billion [6].

1.1 The motivation of the research

The potential to improve materials efficiency, enable greater engineering functionality, reduce material waste, enhance production times, and reduce part cost has made AM a desirable manufacturing tool for various industries. The characteristics of printing an AM part, however, depend on the AM process that is selected. AM consists of seven major divisions, and directed energy deposition (DED), which is propitious metal AM class, is one of them. The ability of DED to create new components and repair damaged parts makes it very popular in many industries. The Plasma-based DED is particularly well suited for printing the more byzantine and large shapes, such as nozzles, gaskets, and pumps. The in-house developed plasma transferred arc additive manufacturing (PTA-AM) system recently confirmed that it could build wear and abrasion resistant parts for the oil, mining, and gas sector. Although this system shows tremendous potential, ensuring the repeatability of the process and the reproducibility of parts is still judged as one of the biggest challenges to ensure a broad application of this technology in real-world industries. Therefore, the process must be improved and characterized, including a more profound understanding of process parameters' influence on the geometrical properties of the printed parts. Additionally, an assessment of complex phenomena such as interactions among the process parameters (plasma arc and powder flow interactions) needs to be done to characterize their combined effect on the final printed parts. The simulation or numerical-based work and *ex-situ* experimental-based literature exist on the process parameter and printed part correlation in the

laser-based DED process. However, no studies have been found regarding the visual proof of bead geometry variation due to process parameter influence and *in-situ* image processing-based characterization of build quality dependency on process parameters in regular PTA-AM systems.

1.2 Aim of the present work

Based on the problems mentioned in the previous section, the main goal of the research is to characterize the processing parameters of the PTA-AM system and investigate their effect on the geometrical properties of the bead deposition. To achieve this goal, the following objectives are decided in this research work:

1. Develop the *in-situ* image processing-based technique to describe the process parameters-build quality dependency in the PTA-AM system. The processing parameter such as stand-off distance (SOD), powder flow, and plasma arc current is considered in the study. The first objective is to determine the effect of SOD variation on the bead quality. The second goal is to confirm the stability in powder flow distribution for the constant powder feed rate. Additionally, the third objective is to quantify the plasma arc current effect on the bead geometry (height and width).

2. Apply the image processing method in the PTA-AM process, with the intent to understand the governing physical phenomena, such as powder particles-plasma arc interaction and their effect on in-flight particle motion path and velocity. The last objective is to investigate the parametric effect of powder particles' motion dynamics on their spreading and solidification during their impingement on the substrate.

1.3 Literature review

This part of the thesis will discuss the brief idea about additive manufacturing and its classification. Later, the potential applications and the challenges of the AM will be covered. Finally, this chapter also covers the thesis outline.

1.3.1 Additive manufacturing (AM)

Additive manufacturing refers to a manufacturing technique that fabricates three-dimensional components by progressively accumulating thin layers of material on one another guided by design from the computerized 3D model. The general AM process begins with designing the 3D CAD model of the component to be printed, converting the CAD model to STL format, slicing the 3D model into 2D multi-layers using slicing software, and forming the 3D geometry of the component by printing each 2D profiles layer by layer via selective deposition path [7]. A historical analysis of AM unveils that stereolithography apparatus was developed in the 1980s for first-ever prototype production purposes [8]. In addition, the first commercialized AM system called the SLA-1 system was launched by 3D Systems Inc. during that period to produce the 3D objects. A technology like this was created to make engineers' ideas a reality. The rapid prototyping process is one of the earliest AM processes. As this technology expanded to manufacturing the final product, it became known as rapid manufacturing. Different terms have been used to describe AM, such as layered manufacturing, additive fabrication, 3D printing, digital manufacturing, and freeform fabrication [9]. With AM, designers can manufacture complex shapes (creating a greater level of design freedom), separate components can be consolidated into a single part, and sustainable products can be produced without incurring environmental impact, which is not possible or convenient with

traditional manufacturing [10]. As per ASTM Standard F2729-12, an AM is the "process of joining materials to make objects from 3D model data usually layer-by-layer, as opposed to subtractive manufacturing technologies such as traditional manufacturing" [11], [12]. AM contrasts with conventional manufacturing methods (CM), which use subtractive or formative manufacturing procedures. Figure 1-1 shows how AM methods differ from CM methods in terms of manufacturing techniques.
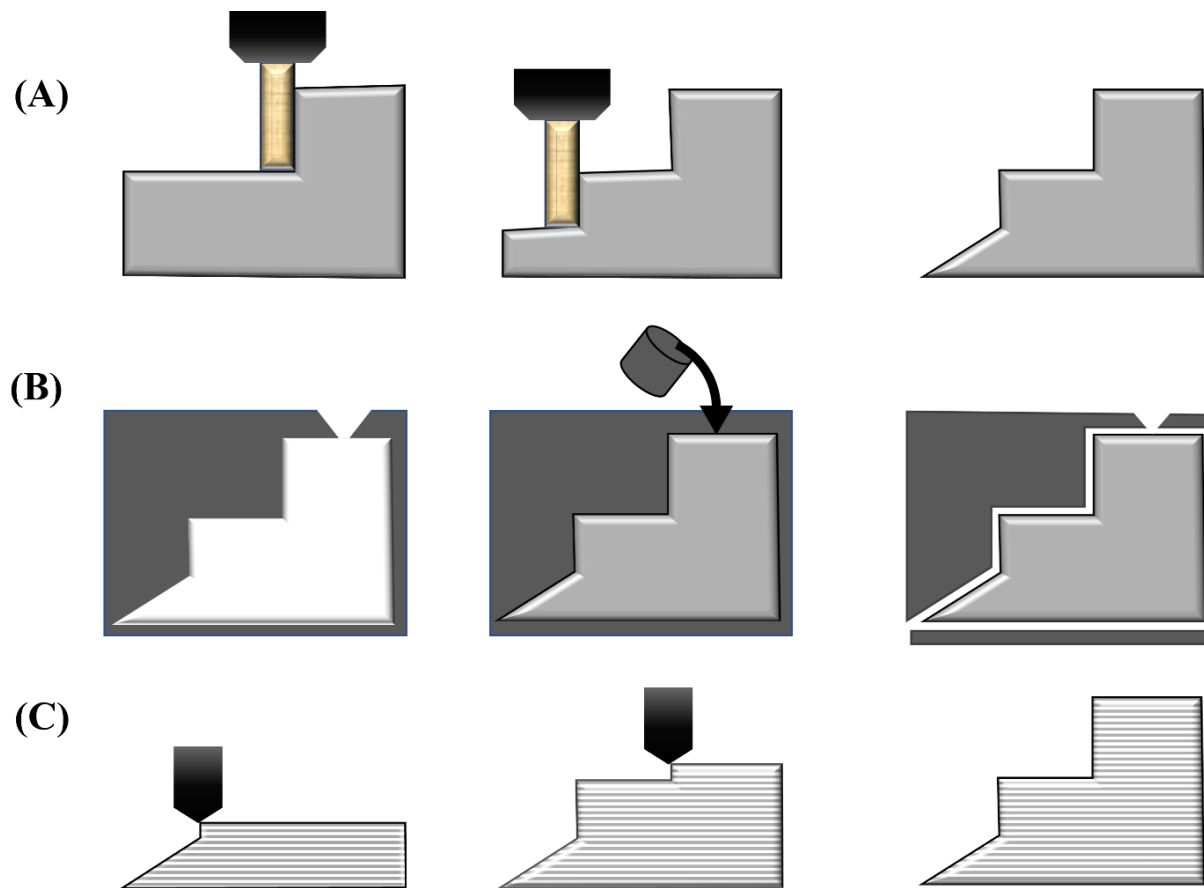
Figure 1-1 Comparison between A) Subtractive manufacturing, B) Formative manufacturing, and C) Additive manufacturing.

In subtractive manufacturing, the material is subtracted from a block to create a final shape through several machining passes. A significant side effect of this process is that significant amounts of waste are created, not always recycled. There are also machining costs and tool wear associated with this process. Formative manufacturing refers to processes such as die-casting, injection molding, and pressing. Components produced by these processes create less waste than those produced by subtractive manufacturing; however, they usually require additional machining tools for post-processing to achieve the required surface finish. Molds or dies are most commonly used during formative manufacturing. Since these tools are customized for each manufactured part, formative manufacturing is generally only cost-effective at large scales. Additionally, molds and dies wear out over time and must be restored or replaced before being used again [13]. In AM, the material is deposited layer by layer to manufacture parts with a near-net shape. While traditional manufacturing processes impose many constraints on product designs, additive manufacturing offers designers more flexibility to optimize their designs for lean production, eliminating waste by its very nature, as shown in Figure 1-1 (c). In addition, AM allows for complex geometries to be built that would not be possible with CM methods. Furthermore, AM's ability to design topologically optimized designs could enhance a product's functionality, reducing the use of energy, fuel, and natural resources, thus reducing its environmental impact [14].

The success of a printing process in AM is determined by selecting print parameters and the material [15]. To date, several AM processes have fabricated fully consolidated parts using various materials with mechanical properties that are considerably better than those of their CM counterparts [16]. A wide range of materials is presently used for 3D printing, including polymers, ceramics, concrete, and metals. Acrylonitrile butadiene styrene (ABS) and Polylactic acid (PLA)

are the main polymers in AM employed to print composites. Ceramics are primarily applied in 3D printed scaffolds. Concrete is the crucial material utilized in the AM of buildings. Advanced metals and alloys are usually used in the aerospace sector because traditional methods are more complicated, costly, and time-consuming [3]. It is also applied in the biomedical, automotive, and defense industries. Metal AM provides excellent autonomy for building complex geometries of multi-functional components, which can simultaneously provide the solution to structural, protective, and insulation engineering problems [3]. In particular, titanium and its alloys, nickel-based, aluminum-based, cobalt-based, and magnesium alloys, have been an option for AM. These are high-performance materials commonly used in various industries [17], [18]. These metallic materials are distinguished by long lead-time and high machining costs based on CM methods. As a result, AM offers significant economic benefits by manufacturing very complex structures at lower costs and near-zero material waste.

The interest and investments in AM technologies have risen significantly recently, which is no surprise as this layer-wise additive method is a refined concept that allows for complex geometric shapes to be manufactured with a wide range of materials [10]. With AM processes' expanding knowledge and potentials, the advantages of designing and fabricating using AM are making the business case further fascinating [3]. A wide variety of AM techniques is available; they differ in the manner in which the layers are deposited to build the parts with required properties, in their operating principles, and the material to be employed. In addition, when selecting a technique, the most important factors to consider are the component and material specification, the application, technology constraints, accuracy, quality of completion, and post-processing. Each AM technique

has its pros and cons. AM systems are categorized according to the feedstock material, energy source, and size of deposit geometry [19], [20].

1.3.2 Additive manufacturing methods

The "American Society for Testing and Material (ASTM) standard F2792" classified the AM process into seven categories. The standards were developed to address the lack of process categorization in the AM world, which makes it challenging to identify similarities and differences between processes [21]. Figure 1-2 summarizes the different AM processes in the form of a flowchart [21].
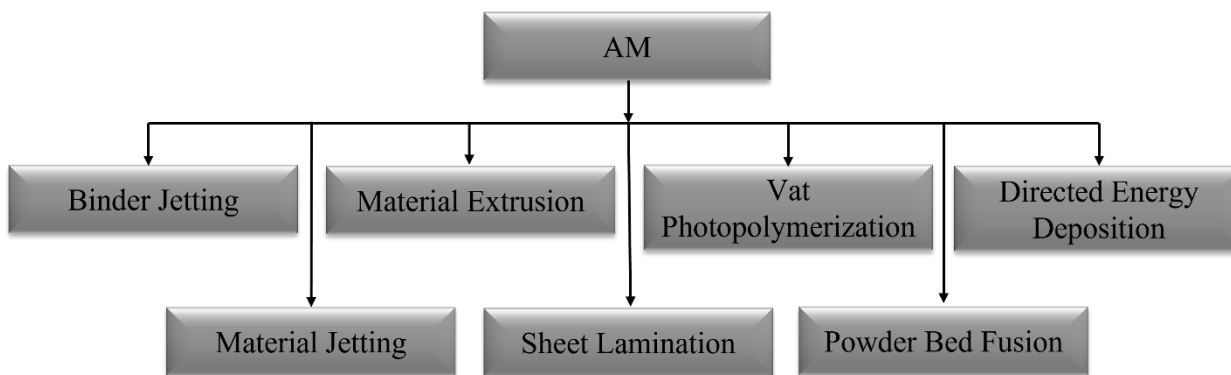
Figure 1-2 Classification of Additive manufacturing processes

1.3.2.1   Binder Jetting

Binder jetting is one of the AM processes developed in the 1990s by the Massachusetts Institute of Technology (MIT), but it was commercialized only in 2010 [22], [23]. This process typically uses two materials: the powder bed (metal, polymer, sand, and ceramics), of which the part is to be printed, and a liquid binder material, which glues the powder particles and then bonds the layers

together. The process is reiterated until the part is entirely printed. Binder jetting is similar to any other AM process that takes place for printing an AM part. However, the binder jetting process involves various post-processing steps such as de-powdering, curing, sintering, and annealing, which takes longer than the actual printing and may incur high costs [12], [24], [25]. In addition, the parts produced using this process are delicate with restricted mechanical properties. One of the advantages of the process is that the parts can be made without support structures. The built part can be used unbounded powder bed as a support structure [26]. Applications of this AM process are observed in the fabrication of molds and cores for sand casting patterns, colored parts, and prototypes [27], [28].

1.3.2.2 Material Jetting

Material jetting is another AM process developed in 1984, creates 3D printed parts on the build platform by dispensing the liquid droplet materials using ink-jet print heads [29]. This process prints the layer of liquid drops on the build platform and then hardens it with ultraviolet light before adding the next layer. Multiple printheads can be operated to print the objects with different materials; thus, objects with different properties and qualities can be created [27]. Since this process relies on the drop deposition technique, only materials with low melting points, such as photopolymers, resins, or wax-like materials, can be used due to their viscosity limitations [29]. The material jetting process can print with a resolution of 10-30 microns (based on material, drop deposition speed, and printer speed), making the layer barely perceptible to the human eye. These flexible abilities make the process attractive for the application of jewelry, medical devices, the automotive industry, and the aerospace sector [30].

1.3.2.3   Material Extrusion

The material extrusion method causes the material to move through an extrusion die due to pressure force, producing an extruded material with a uniform cross-section and a desired diameter [31]. In 1988, the co-founder of Stratasys Ltd., Scott Crump, used this extrusion-based process, who developed the AM technique called Fused Deposition Modeling (FDM) to print the 3D objects by mechanically extruding the melted material through the nozzle or orifice (such as polymer-based filaments, thermoplastics) onto the substrate [31]. The FDM is relatively cheap and simple to use compared to other AM. In addition, it is an excellent alternative to the CM methods in a certain way; however, FDM is a slow process and can exhibit geometrical inconsistencies. The correctness and quality of final products in FDM are limited by the nozzle's inlet dimensions [32], [33]. FDM application is found in various sectors: aerospace, automotive, and medical [34].

1.3.2.4   Sheet Lamination

The sheet lamination techniques create the 3D objects by bonding material sheets together. Layer-by-layer bonding between sheets is achieved by using different mechanisms such as adhesive bonding, clamping, thermal bonding, and ultrasonic welding [27]. Sheet lamination includes two subclasses: Laminated Object Manufacturing (LOM) and Ultrasonic AM (UAM). In 1986, Helisys Inc. developed the AM system using LOM, and it was patented in 1987 [10]. LOM involves layering plastic material with heat and pressure and then cutting it into the desired shape using a laser. In UAM, ultrasonic welding bonded metallic sheets with an additional CNC machining process [27]. A large object can be manufactured since no chemical reaction is required. Melting of material is not required in the sheet lamination process, making it a low-energy process. LOM offers several advantages, such as low internal tension, low part fragility, great surface detailing,

and lower material, equipment, and processing costs [35]. However, this AM process cannot produce the same geometrical complexities as other AM processes [2].

1.3.2.5 Vat Photopolymerization

Van photopolymerization is one of the AM processes, also known as stereolithography apparatus (SLA), and is used for creating 3D objects with liquid polymer resin [2], [35]. Photopolymer resin is cured by UV light to fabricate models, prototypes, and patterns. The layers are consequently cured until the 3D part is completed. Different polymer grades can be utilized in the process. An SLA method, developed by Charles Hull in 1984, became the first commercial AM process. SLA can build at a relatively high speed (1–3 cm/hour), and the minimum layer thickness depends on the curing depth. This method has several downsides, such as support structures requirement, processing errors caused by over-curing, and expensive supplies and materials. Since this technology relies on photopolymerization, it can only be applied to photopolymers [36].

1.3.2.6 Powder Bed Fusion

The powder bed fusion (PBF) method begins by transporting the thin layer of powder material across the build platform using a roller mechanism. An energy source, i.e. laser or electron beam, is instructed to selectively dose energy to the powder bed to melt and fuse the material [27]. The powder bed slowly moves down as each layer is completed, reiterating the process until the desired shape is attained. Selective Laser Melting (SLM) and Electron Beam Melting (EBM) are two different metal PBF processes most commonly employed in the AM industry, as shown in Figure 1-3. EOS GmbH (Germany) and Arcam Ab (Sweden) developed them in 1995 and commercialized them in 2005, respectively [10]. Both types of PBF fabricate the 3D objects with high density, high

surface finish, and similar mechanical properties of formed parts. The processes differ regarding the atmosphere for printing, toolpath planning, powder properties, and recoating techniques [37].
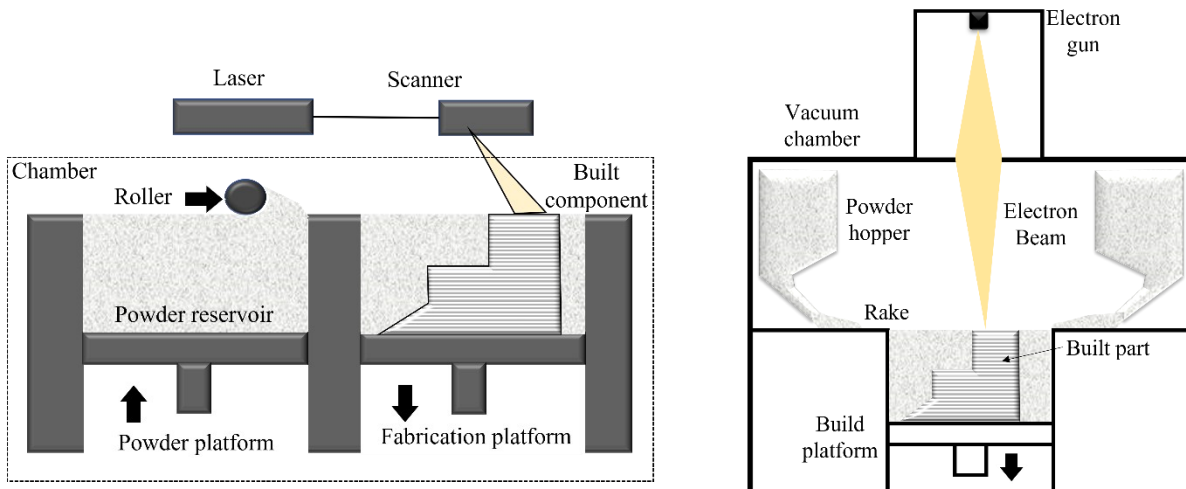
Figure 1-3 Schematic of powder bed fusion equipment (a) Selective Laser Melting and (b) Electron Beam Melting

As its name implies, SLM uses lasers to melt and fuse metal powders. The whole process takes place within a closed chamber that often contains an inert gas such as N2 or Ar, based on the reactivity of the powder material to be employed [38]. A chamber filled with inert gas keeps the process from being contaminated by oxygen. Substrate plate heating can be used to minimize cooling rates and prevent 3D parts from cracking. SLM is regarded as the best AM process due to its ability to process a broad range of advanced metals and alloys. Some of the most significant benefits of SLM include utilizing a wide range of materials, producing parts with multi-functional properties, and creating near-neat shape parts ready to use. However, SLM has some drawbacks: its relatively slow process, severe size restrictions, high energy requirements, and high initial costs. Process parameters optimization is time-consuming [39].

SLM and EBM are almost identical processes; both use layer-by-layer technology; however, the EBM process has some differences, such as using an electron beam instead of a laser beam to melt and fuse powder particles. The powder bed is maintained at a high temperature, and overnight cooling is required after the build is completed. With an EBM process, more parameters are accounted for, making the process more challenging than the SLM process. The EBM process is operated in a vacuum atmosphere, in contrast to the inert atmosphere used during the SLM process. The EBM process can process brittle materials as intermetallics and high entropy alloys without crack formation in the objects by carefully selecting the proper temperature of the powder bed. Each layer is processed using the electron beam multiple times, resulting in a much longer processing time than an SLM process. Additionally, the whole chamber becomes hot enough after the printing process that it may necessitate considerable cooling before the printed object can be removed from the chamber [23] [39].

1.3.2.7   Directed Energy Deposition

Direct energy deposition (DED) is another highly developed AM technique that is particularly widespread for its potential to print AM parts and remanufacture or repair the parts by adding the material to already constructed parts [2], [29]. DED system uses the concentrated energy source and stream of feedstock material which intersect at any common focal point where the thermal energy melts the feedstock material. A melted material is deposited, fused to the substrate, and subsequently solidified after moving the energy source. Depending on the applications, geometry size, and build quality, the energy source could be a laser, an electron, or a welding arc [2], [29]. Various DED systems are classified according to feedstock material and energy source. Figure 1-

4 presents a flowchart of the different DED categories [40]. Based on the feedstock type, powder-feed and wire-feed DED systems are available.
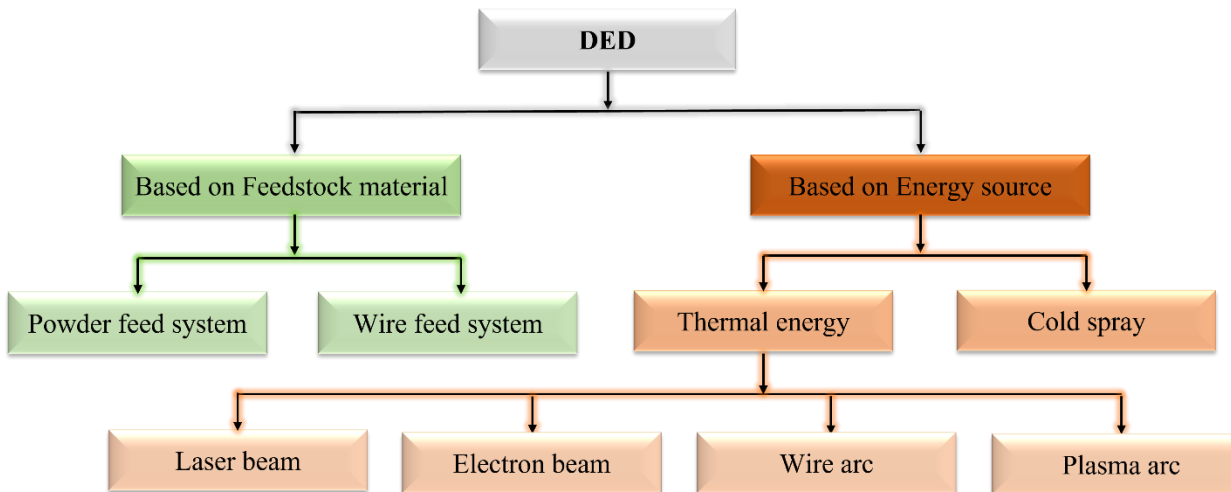
Figure 1-4 Categorization of Directed Energy Deposition (DED) methods

The thermal-based DED and kinetic energy-based DED (cold spray) are available based on the energy used. Thermal-based DED could be further divided into the laser, electron-beam, plasma, and electric arc-based DEDs, which are discussed as follows.

a. Laser-based DED

In this DED-AM process, the laser beam is directed on the substrate to create the molten pool. Simultaneously the powder stream is fed into the exact spot where the laser is focused. As a result, the deposited powder material melts, and layer by layer deposition forms the 3D parts on the substrate. This process is completed in a closed chamber using argon gas to protect the molten metal from oxidation. A CAD model is used to direct laser movement using toolpath plans based on the 3D shape of the model [39], [41]. As the system is designed, either the laser source or the

substrate table moves to deposit subsequent layers. Laser-engineered net shaping (LENS) is one of the laser-based DED AM processes [2], [39]. The LENS method was developed at Sandia National Laboratories in 1995 and is currently being commercialized by Optomec. LENS can fabricate parts from multi-materials of different grades [42]. The printed part's rapid cooling and local melting make the well-refined grains microstructure, and the part is usually 30% stronger than those constructed through casting. Parts can be repaired using this method since selective restoration is possible in the damaged area.
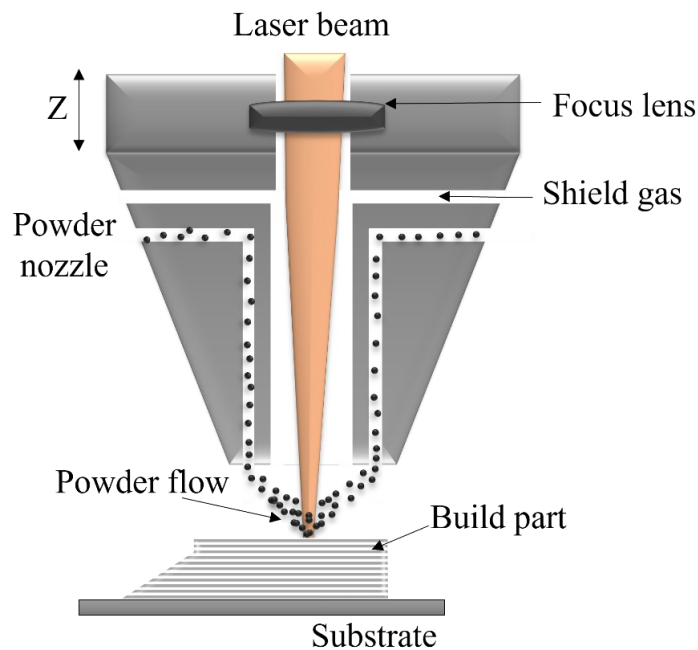
Figure 1-5 Schematic of Laser Engineered Net Shaping process (LENS)

b. Electron beam-based DED

Electron beam freeform fabrication (EBF^3) is another DED-AM process for constructing structural metal parts [2][39]. EBF^3 employs an electron beam as a high-power energy source in the vacuum chamber to melt the continuously supplying feedstock material on the substrate (Figure 1-6). Wire-

based feeding is used due to the complexity of feeding powder in the vacuum environment due to the ionization of the carrier gas that helps deliver the powder [43].
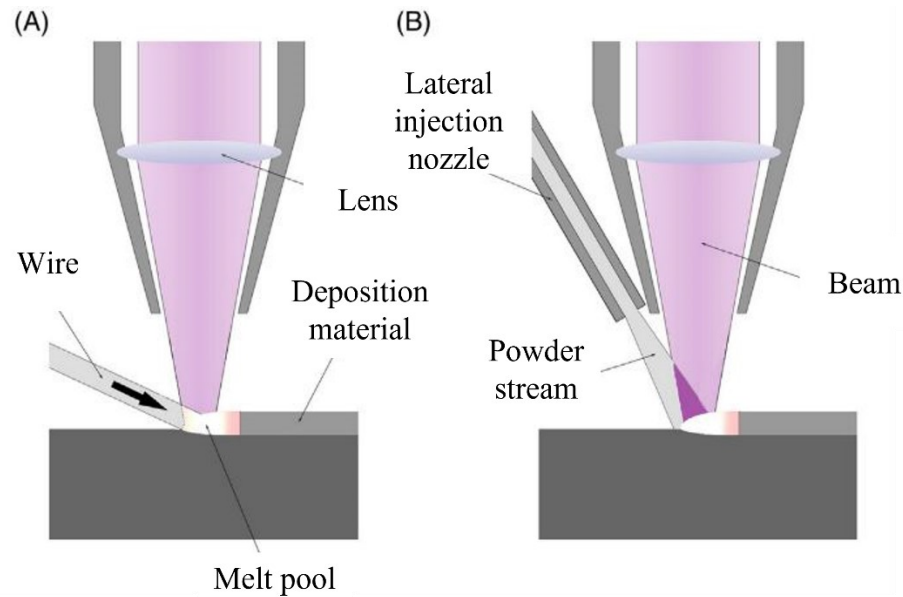
Figure 1-6 Electron beam DED based on feedstock material as an (A) wire and (B) powder [2]

Vacuum-based processes provide a clean environment and eliminate a consumable shield gas, generally used in laser-based DED systems. In addition, EBF^3 can print very reactive metal parts due to no connection with atmospheric gases, the printing of highly reflective alloys, and electrically conductive metal, including copper and aluminum. However, the prerequisite of a vacuum environment hinders large-scale 3D parts production. EBF^3 is nearly 100% efficient in terms of feedstock consumption, and in terms of energy, it is nearly 95% efficient [43]. EBF^3 requires the whole build volume to be confined in a vacuum during the process. This substantially escalates the cost and time of the process as compared to DED-AM systems that only require shielding gas flow or an inert environment [44].

c. Wire + Arc DED

Wire + arc additive manufacturing (WAAM) is also classified in the category of DED system as per ASTM F2792 12a [21]. It combines arc welding and wire feeding system for AM purposes.
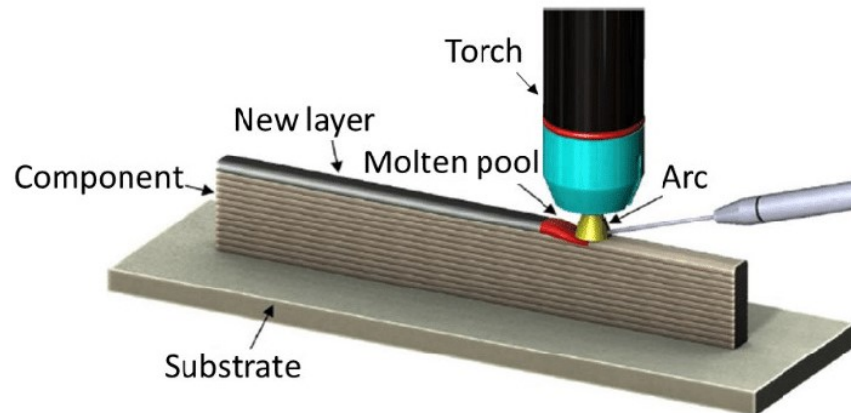
Figure 1-7 Schematic of Wire+arc additive manufacturing [45]

The process uses the electric arc as a thermal energy source to melt the continuously feeding wire as a feedstock material. The layer-by-layer deposition of melted wire builds the near net shape parts[46]. A multi-axis table or a robot arm is used to operate the system. WAAM is gaining popularity because it offers a more cost-effective alternative to the CM method for comparatively large 3D metal parts with low to medium geometric complexity [47]. Electric arc systems are highly efficient and can be operated with a range of heat inputs and deposition rates. Pulsing the arc and changing the waveform and frequency of the arc can be used further to manipulate the deposition of material [48]. It is well known that the microstructural properties vary due to thermal history during the manufacturing process. However, the idiosyncratic WAAM thermal cycle, which includes cyclic heating and cooling, produces the parts with meta-stable microstructural properties and inhomogeneous composition [17].

d. Plasma arc-based DED

In the 1960s, the plasma arc welding (PAW) process was adopted for surface modification in the overlays industry, which led to the development of plasma transferred arc (PTA) [49]. It can be considered that the PTA system is the derivative of the PAW system. Although both these plasma-based welding processes utilize non-consumable tungsten electrodes, there is a significant difference between them: PTAW uses wire feedstock material, while PTA uses powder feedstock that requires argon gas to carry the powder stream to the plasma arc region [50].

Plasma transferred arc (PTA) is a fascinating technique for layer deposition of blown powder in the AM industry. PTA is comprised of the newly named 3D Plasma Metal Deposition (3DPMD) group that belongs to the DED category [47]. The PTA-AM depends on the current as well as voltage to create plasma arcs [51]. The required current value is inputted in the system, which controls the current flow between the plasma torch and the substrate. On the other hand, voltage is governed by the pressure difference between the plasma torch and the substrate, and it can be varied by adjusting the distance. The plasma arc is created as the current ionizes the inert gas (such as argon) between the plasma torch and the substrate [37]. In the PTA-AM system, the powder stream is transported from the powder hopper to the substrate via a plasma torch containing the non-consumable electrode and the plasma arc. As the powder stream enters the plasm arc region, it melts and impinges on the substrate. The melted pool solidifies as the torch moves over it, leaving a solid deposit behind [37]. The process is reiterated until the 3D object is printed.

Compared to other AM, the PTA-AM method has significant advantages because it allows us to fabricate specimens with larger dimensions than those produced with PBF techniques. Furthermore, the high feed rate may result in a higher production rate than other AM technologies

[52]. It also offers the advantages of the refined microstructure of deposit, a small area affected by heat, and low distortion. PTA-AM permits printing 3D parts with homogenous, functionally graded materials, which is impossible in other laser-based and electron beam-based AM methods. PTA-AM is also capable of processing powders with a wide distribution range, from 45-150 microns. PTA-AM does not suffer from the different microstructures of powders of different sizes since powders are fully melted during this process. Nevertheless, the powder size distribution is more critical for the LENS method since the powder is sintered instead of melted [37].

1.3.3 Applications of AM

Over the past few years, advanced AM techniques have significantly progressed, yielding applications to an ever-wider range of industries. In contrast to subtractive manufacturing, AM lends itself particularly well to manufacturing small quantities of intricate parts [53]. A report stated that reducing the amount of materials and energy used in the current manufacturing methods could significantly mitigate climate change. It is certainly true that industry emits nearly 30% of total greenhouse gas emissions [54]. The majority of industrial greenhouse gas emissions are attributed to the processing of materials. It is evident that the AM techniques can reduce the amount of energy and resources required for manufacturing processes, reduce the amount of material needed in the supply chain, and enable environmentally friendly practices [55].

In the aerospace industry, the components usually have complicated geometries and are made from advanced metal and superalloys, which are complex, expensive, and time-consuming [57]. Complex aerospace components include multiple simple parts joined with various fasteners (bolts, welds, and brazes). However, such assemblies are less reliable and require more inspection,

Figure 1-8 Exhaust mixer for gas turbine produced by LENS [56]

tooling, and maintenance than a single component. AM is an effective tool for consolidating parts. This allows for better feature integration as well as more excellent reliability [53].

The buy-to-fly ratio in aerospace is an essential contributor to the high manufacturing costs, as it denotes the ratio between the raw material's weight and the final component's weight. In this scenario, the material usage and the fabrication cost can be substantially enhanced with AM freeform fabrication facilities and lower the buy-to-fly ratio nearer to 1:1 [53]. Moreover, aerospace production runs are generally small, limited to a maximum of a few thousand parts. This makes AM technologies ideal for aerospace applications as AM is more cost-effective for custom parts and small batches [53]. For example, Figure 1-8 shows1:6 scale exhaust mixer of gas turbine for Bell helicopters manufactured by Optomec using the LENS process [56]. In the automotive industry, product development is significant, but the process is often expensive and time-consuming. Since AM technology allows for a shortened product development cycle and lower manufacturing and product expenses, it has been an essential tool for the automotive industry. Additionally, AM methods have been employed for the small production run of structural and functional components like driveshafts, engine exhausts, gearbox parts, brake systems for luxury

cars, and low-volume motor vehicles [56][58]. Racing vehicles are often made from lightweight alloys with complex structures and low production volumes. Companies and research institutions have profitably applied AM technology to produce functional components for racing motor vehicles. For example, Arcam [59] used EBM- based AM technique with Ti6Al4V material to fabricate racing car parts such as suspension parts and engine parts, especially with lattice structures and gearboxes (Figure 1-9).

Figure 1-9 Racecar gearbox produced by EBM [59]

According to the latest Wohlers' report [60], AM market has expected to grow from $6.1 to $21 billion by 2020, and the biomedical market shares 11% of the overall AM market. In recent years, advances in AM technology, biomedicine, biological sciences, biomaterials have demonstrated the potential of applying AM technologies in the biomedical field to products such as orthopedic implants, artificial organs, tissue scaffolds, and medical devices [61]. The AM flexibility enables engineering novel materials, for instance, semicrystalline polymeric composites used to produce extremely complex shapes [62]. From implants to drug dosage, biomedical applications must be tailored to individual patients. AM offers a wide range of patient-specific biomedical products,

ranging from hearing aids to biomedical implants [63] and custom orthotics to prostheses [64]. Research institutes and universities are also studying the use of AM for biomedical implants. A Ti6Al4V implant (Figure 1-10) was designed with tailored mechanical properties that mimic the bone structure, and the EBM-based AM technique has fabricated it [65].

Figure 1-10 Hip stems with mesh, hole and solid configurations fabricated using EBM [65]

The DED-based AM processes have recently been employed to repair and remanufacture the high-value damaged components [54]. It has been revealed that conventional repair methods face several challenges, including high residual stress, distortion of the repaired part, low flexibility in geometry, and extensive post-machining. The DED process is excellent for repairing and remanufacturing automotive and aerospace components. DED has more advantages than conventional welding, including less heat input, less warpage, less distortion, lower dilution values, higher cooling rates, great metallurgical bonding within deposited layers, and high accuracy. DED is effectively used in diverse industries to repair various parts, including the crankshaft, driveshaft, four-stroke pistons, and turbine blades [54].
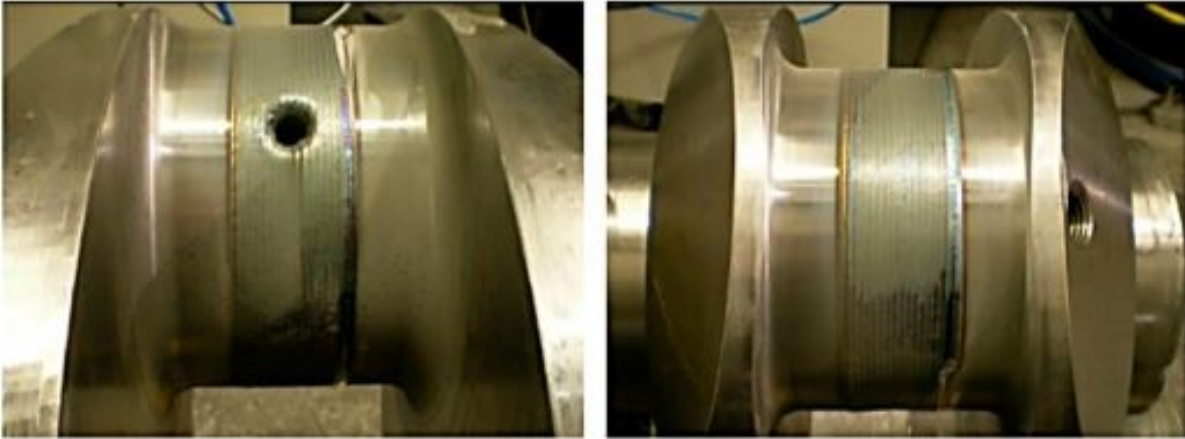
Figure 1-11 Marine diesel crankshaft repaired using DED system [54]

1.3.4 Challenges in AM

The advent of additive manufacturing has led to the invention of many new products and applications. Nevertheless, there are challenges to overcome before this tool can truly be utilized. AM presents various challenges, comprising fabrication timeliness, material challenges, production cost, dimensional and geometrical accuracy, and manufacturing parameter optimization. This thesis aims to research the variation in geometry of the printed beads based on the manufacturing parameters used in the AM process. Furthermore, it focuses on the flow of metal powders and their interaction with the energy source.

With reference to dimensional and geometrical accuracy, the main challenge in the AM processes is understanding the physical properties of a deposited part which is the function of numerous manufacturing parameters such as energy source (laser/plasma/electron beam power), powder/wire feed rate, stand-off distance (distance between torch and substrate), table travel/scanning speed, and gas flow rate (central, carrier /shielding). Another challenge is

investigating the physical phenomena among these parameters, such as laser/plasma-powder flow interaction, powder/wire melting due to arc current, molten metal deposition into a molten pool, liquid metal flows into the pool through surface tension gradient, deformation of the molten pool due to arc pressure and molten pool solidification [66]. Due to many processing parameters and these complex physical phenomena, optimizing the AM process to achieve the near-net-shape part is complex. It is crucial to identify the correlation between geometry deviation and the processing parameters as it affects the final product's geometry (size and shape) and quality. A high degree of dimensional accuracy is crucial for products such as biomedical products that have to fit perfectly into patients' bodies and reverse engineering where exact dimensions are needed to fit the damaged parts. A turbine blade's dimensional accuracy is also vital for energy efficiency and vibration prevention [66].

The variation in quality and geometry of deposited parts can arise due to several reasons. However, poor choice of selecting the process parameter can significantly deviate the quality and geometry dimensions. The heat input parameter is a fundamental variable in the AM process that changes the deposited part's width and height and affects the microstructural properties. Determining how much heat is required to melt/sinter the delivered material from the feeding system is challenging. Insufficient heat input may encourage improper melting of the feedstock, resulting in undesirable effects on the final part dimensions and surface quality. A similar undesirable effect of excess heat is poor surface finish and excessive deformation of the deposited layer. Furthermore, residual stresses caused by AM processes' continuous rapid heating and the cooling cycle can yield substantial part distortions that significantly impact the final product's functionality [37].

Powder/wire feeding rate into the heat source (plasma/laser) affects the deposition geometry and the deposition rate. A critical factor in achieving a stable bead height is to control the powder feeding rate. The powder feeding rate also affects the temperature of the powder particles that hit the substrate. As part of the laser-based DED AM process, the shape of the gas-powder stream, powder-laser interaction, as well as particle velocity and distribution are key factors influencing clad quality, clad geometry, and powder entrapment [67].

1.4 Thesis outline

The thesis structure and subsequent chapter topics are discussed in this section. This thesis is focused on analyzing the dependency of bead quality on processing parameters of the PTA-AM process, which involves the influence of plasma arc current,

In chapter 2 (Accepted in International Journal of Advanced Manufacturing Technology), we have presented the in-situ image processing technique to investigate the dependency of quality of bead on the processing parameters, including plasma arc current, powder flow distribution (powder particle count), and stand-off distance (SOD). We also used the statistical tests (ANOVA and two-tailed t-test) to determine the significance of built geometry dependency and powder particle count. The validation of optimized SOD and uniformity in powder flow for the stable and uniform bead is also presented in this chapter.

In chapter 3 (Submitted in the International Journal of Heat and Mass Transfer), the image processing technique has been discussed to analyze the powder flow behavior under the influence of plasma arc current. The variation in individual powder particles velocity and their trajectories due to plasma arc velocity is investigated. The dynamics of the powder particle motion are

validated with the theoretical single powder particle trajectory model. In the later section of this chapter, using a theoretical model, the parametric study has been presented to investigate the parametric effect of powder impact motion on the spreading and solidification of molten powder particles during their impingement on the substrate.

The final chapter concludes the whole thesis work and describes the potential future to extend upon the research.

References

[1]   M. Bhuvanesh Kumar and P. Sathiya, "Methods and materials for additive manufacturing: A critical review on advancements and challenges," Thin Walled Struct., vol. 159, no. July 2020, p. 107228, 2021, doi: 10.1016/j.tws.2020.107228.

[2]   J. Klingelnberg, Manufacturing Process. Elsevier Inc., 2016.

[3]   T. D. Ngo, A. Kashani, G. Imbalzano, K. T. Q. Nguyen, and D. Hui, "Additive manufacturing (3D printing): A review of materials, methods, applications and challenges," Compos. Part B Eng., vol. 143, no. December 2017, pp. 172–196, 2018, doi: 10.1016/j.compositesb.2018.02.012.

[4]   Gartner, "Hype Cycle for 3D Printing.," 2014.

[5]   T. Wohlers, "Wohlers Report 2016: Executive Summary, Wohlers Associates Inc., Fort Collins, 2016.," 2016.

[6]   A. Manyika, J., Chui, M., Bughin, J., Dobbs, R., Bisson, P., & Marrs, "Disruptive technologies: Advances that will transform life, business, and the global economy," McKinsey Glob. Inst., vol. 180, pp. 17–21, 2013.

[7]   J. Xu, X. Gu, D. Ding, Z. Pan, and K. Chen, "A review of slicing methods for directed energy deposition based additive manufacturing," Rapid Prototype. J., vol. 24, no. 6, pp. 1012–1025, 2018, doi: 10.1108/RPJ-10-2017-0196.

[8]   C. W. Hull, "Apparatus for Production of Three-Dimensional Objects by Stereo Thography," Patent, no. 19, p. 16, 1984.

[9]   J. Y. Lee, A. P. Nagalingam, and S. H. Yeo, "A review on the state-of-the-art of surface finishing processes and related ISO/ASTM standards for metal additive manufactured components," Virtual Phys. Prototype, vol. 16, no. 1, pp. 68–96, 2021, doi: 10.1080/17452759.2020.1830346.

[10]   W. Gao et al., "The status, challenges, and future of additive manufacturing in engineering," CAD Computer. Aided Des., vol. 69, pp. 65–89, 2015, doi: 10.1016/j.cad.2015.04.001.

[11]   ASTM International, "ISO/ASTM52900-15 Standard Terminology for Additive Manufacturing—General Principles—Terminology. West Conshohocken, PA:ASTM International" 2015 https://doi.org/10.1520/ISOASTM52900-15. .

[12]   J. Y. Lee, A. P. Nagalingam, and S. H. Yeo, "A review on the state-of-the-art of surface finishing processes and related ISO/ASTM standards for metal additive manufactured

components," Virtual Phys. Prototyp., vol. 16, no. 1, pp. 68–96, 2021, doi: 10.1080/17452759.2020.1830346.

[13]   M. Akmaliyah, "Development and Characterization of Additive Manufacturing of Superalloy Hastelloy X Using a Cost-Effective TIG Technique," J. Chem. Inf. Model., vol. 53, no. 9, pp. 1689–1699, 2013.

[14]   S. H. Huang, P. Liu, A. Mokasdar, and L. Hou, "Additive manufacturing and its societal impact: A literature review," Int. J. Adv. Manuf. Technol., vol. 67, no. 5–8, pp. 1191–1203, 2013, doi: 10.1007/s00170-012-4558-5.

[15]   E. A. Alberti, B. M. P. Bueno, and A. S. C. M. D. Oliveira, "Additive manufacturing using plasma transferred arc," Int J Adv Manuf. Technol., pp. 1861–1871, 2016, doi: 10.1007/s00170-015-7697-7.

[16]   H. Fayazfar et al., "A critical review of powder-based additive manufacturing of ferrous alloys: Process parameters, microstructure and mechanical properties," Mater. Des., vol. 144, pp. 98–128, 2018, doi: 10.1016/j.matdes.2018.02.018.

[17]   D. Herzog, V. Seyda, E. Wycisk, and C. Emmelmann, "Additive manufacturing of metals," Acta Mater., vol. 117, pp. 371–392, 2016, doi: 10.1016/j.actamat.2016.07.019.

[18]   E. Sheydaeian and E. Toyserkani, "A new approach for fabrication of titanium-titanium boride periodic composite via additive manufacturing and pressure-less sintering," Compos. Part B Eng., vol. 138, no. November 2017, pp. 140–148, 2018, doi: 10.1016/j.compositesb.2017.11.035.

[19]   H. Fayazfar et al., "A critical review of powder-based additive manufacturing of ferrous alloys: Process parameters, microstructure and mechanical properties," Mater. Des., vol. 144, pp. 98–128, 2018, doi: 10.1016/j.matdes.2018.02.018.

[20]   A. Zikin, S. Ilo, P. Kulu, I. Hussainova, C. Katsich, and E. Badisch, "Plasma transferred arc (PTA) hardfacing of recycled hardmetal reinforced nickel-matrix surface composites," Medziagotyra, vol. 18, no. 1, pp. 12–17, 2012, doi: 10.5755/j01.ms.18.1.1334.

[21]   ASTM International, "F2792-12a: standard terminology for additive manufacturing technologies," Procedia Eng,63, pp. 4–11, 2012.

[22]   E. Sachs, M. Cima, P. Williams, D. Brancazio, and J. Cornie, "Three dimensional printing: Rapid tooling and prototypes directly from a CAD model," J. Manuf. Sci. Eng. Trans. ASME, vol. 114, no. 4, pp. 481–488, 1992, doi: 10.1115/1.2900701.

[23]   P. K. Gokuldoss, S. Kolla, and J. Eckert, "Additive manufacturing processes: Selective laser melting, electron beam melting and binder jetting-selection guidelines," Materials (Basel)., vol. 10, no. 6, 2017, doi: 10.3390/ma10060672.

[24]   K. V. Wong and A. Hernandez, "A Review of Additive Manufacturing," ISRN Mech. Eng., vol. 2012, pp. 1–10, 2012, doi: 10.5402/2012/208760.

[25]   A. Kumar et al., "Low temperature additive manufacturing of three-dimensional scaffolds for bone-tissue engineering applications: Processing related challenges and property assessment," Mater. Sci. Eng. R Reports, vol. 103, pp. 1–39, 2016, doi: 10.1016/j.mser.2016.01.001.

[26]   A. Kumar et al., "Low temperature additive manufacturing of three-dimensional scaffolds for bone-tissue engineering applications: Processing related challenges and property assessment," Mater. Sci. Eng. R Reports, vol. 103, pp. 1–39, 2016, doi: 10.1016/j.mser.2016.01.001.

[27]   Parupelli, SantoshKumar, and Salil Desai. "A comprehensive review of additive manufacturing (3d printing): processes, applications and future potential." American journal of applied sciences 16, no. 8, 2019.

[28]   D. S. Engstrom, "Binder jetting" Loughbrgh. Univ., 2012. URL: https://www.lboro.ac.uk/research/amrg/about/the7categoriesofadditivemanufacturing/binderjetting/

[29]   F. J. Mercado Rivera and A. J. Rojas Arciniegas, "Additive manufacturing methods: techniques, materials, and closed-loop control applications," Int. J. Adv. Manuf. Technol., vol. 109, no. 1–2, pp. 17–31, 2020, doi: 10.1007/s00170-020-05663-6.

[30]   Terry T Wohlers; Tim Caffrey, "3D printing and additive manufacturing state of the industry annual worldwide progress report," Wohlers Rep., 2014.

[31]   H. Bikas, P. Stavropoulos, and G. Chryssolouris, "Additive manufacturing methods and modeling approaches: A critical review," Int. J. Adv. Manuf. Technol., vol. 83, no. 1–4, pp. 389–405, 2016, doi: 10.1007/s00170-015-7576-2.

[32]   F. Peng, B. D. Vogt, and M. Cakmak, "Complex flow and temperature history during melt extrusion in material extrusion additive manufacturing," Addit. Manuf., vol. 22, no. August 2017, pp. 197–206, 2018, doi: 10.1016/j.addma.2018.05.015.

[33]   Park SI, Rosen DW, "Quantifying effects of material extrusion additive manufacturing process on mechanical properties of lattice structures using as-fabricated voxel modeling". Addit. Manuf., vol.12, pp. 265-73, 2016.

[34]   J. W. Comb, W. R. Priedeman, and P. W. Turley, "FDM Technology Process Improvements," Proc. Solid Free. Fabr. Symp., pp. 42–49, 1994.

[35]   B. Mueller and D. Kochan, "Laminated object manufacturing for rapid tooling and patternmaking in foundry industry," Comput. Ind., vol. 39, no. 1, pp. 47–53, 1999, doi: 10.1016/S0166-3615(98)00127-4.

[36]   D. T. Pham and C. Ji, "Design for stereolithography," Proc. Inst. Mech. Eng. Part C J. Mech. Eng., vol. 214, no. 5, pp. 635–640, 2000, doi: 10.1243/0954406001523650.

[37]   S. Ibrahim, "Plasma Transferred Arc Additive Manufacturing Using 17-4 Precipitation Hardened Stainless Steel," MSc thesis. Department of Chemical and Materials Engineering, University of Alberta, 2020, p. 180

[38]   P. Lott, H. Schleifenbaum, W. Meiners, K. Wissenbach, C. Hinke, and J. Bültmann, "Design of an optical system for the in-situ process monitoring of Selective Laser Melting (SLM)," Phys. Procedia, vol. 12, no. PART 1, pp. 683–690, 2011, doi: 10.1016/j.phpro.2011.03.085.

[39]   Y. Zhang et al., "Additive Manufacturing of Metallic Materials: A Review," J. Mater. Eng. Perform., vol. 27, no. 1, pp. 1–13, 2018, doi: 10.1007/s11665-017-2747-y.

[40]   A. Dass and A. Moridi, "State of the Art in Directed Energy Deposition : From Additive Manufacturing to Materials Design," Coating, pp. 1–26, 2019, doi: 10.3390/coatings9070418.

[41]   Zhang Y, Jarosinski W, Jung YG, Zhang J. "Additive manufacturing processes and equipment. in Additive Manufacturing", 2018, pp. 39-51, Butterworth-Heinemann.

[42]   M. L. Griffith, L. D. Harwell, J. Romero, E. Schlienger, C. L. Atwood, and J. E. Smugeresky, "Multi-material processing by LENS," Solid Free. Fabr. Symp., pp. 387–393, 1997, [Online].   Available: http://sffsymposium.engr.utexas.edu/Manuscripts/1997/1997-45-Griffith.pdf.

[43]   K. Taminger and R. Hafley, "Electron beam freeform fabrication: a rapid metal deposition process," Proc. 3rd Annu. Automot. Compos. Conf., no. January 2003, pp. 9–10, 2003,URL:http://www.ntrs.nasa.gov/archive/nasa/casi.ntrs.nasa.gov/20040042496_2004036110.pdf.

[44]   C. Körner, "Additive manufacturing of metallic components by selective electron beam melting - A review," Int. Mater. Rev., vol. 61, no. 5, pp. 361–377, 2016, doi: 10.1080/09506608.2016.1176289.

[45]   T. A. Rodrigues, V. Duarte, R. M. Miranda, T. G. Santos, and J. P. Oliveira, "Current status and perspectives on wire and arc additive manufacturing (WAAM)," Materials (Basel)., vol. 12, no. 7, 2019, doi: 10.3390/ma12071121.

[46]   Gibson I, Rosen D, Stucker B. "Directed energy deposition processes", In Additive manufacturing technologies, 2015, pp. 245-268, Springer, New York, NY.

[47]   N. Rodriguez, L. Vázquez, I. Huarte, E. Arruti, I. Tabernero, and P. Alvarez, "Wire and arc additive manufacturing: a comparison between CMT and TopTIG processes applied to stainless steel," Weld. World, vol. 62, no. 5, pp. 1083–1096, 2018, doi: 10.1007/s40194-018-0606-6.

[48]   M. Dinovitzer, X. Chen, J. Laliberte, X. Huang, and H. Frei, "Effect of wire and arc additive manufacturing (WAAM) process parameters on bead geometry and microstructure," Addit. Manuf., vol. 26, no. October 2018, pp. 138–146, 2019, doi: 10.1016/j.addma.2018.12.013.

[49]   L. Łatka and P. Biskup, "Development in PTA Surface Modifications – A Review," Adv. Mater. Sci., vol. 20, no. 2, pp. 39–53, 2020, doi: 10.2478/adms-2020-0009.

[50]   V. V. Diaz, J. C. Dutra, and A. S. C. M. D'Oliveira, "Hardfacing by plasma transfer arc process," Weld. Int., vol. 26, no. 2, pp. 87–95, 2012, doi: 10.1080/09507116.2010.527486.

[51]   Tonya Wolfe. "Homogeneity of Metal Matrix Composites Deposited by Plasma Transferred Arc". PhD thesis. Department of Chemical and Materials Engineering, University of Alberta, 2010, p. 364, doi: https://doi.org/10.7939/ R3K64Q.

[52]   E. M. Perez-Soriano, E. Ariza, C. Arevalo, I. Montealegre-Melendez, M. Kitzmantel, and E. Neubauer, "Processing by additive manufacturing based on plasma transferred arc of hastelloy in air and argon atmosphere," Metals (Basel)., vol. 10, no. 2, 2020, doi: 10.3390/met10020200.

[53]   Najmon JC, Raeisi S, Tovar A. "Review of additive manufacturing technologies and applications in the aerospace industry", Additive manufacturing for the aerospace industry, pp 7-31, 2019.

[54]   A. Saboori, A. Aversa, G. Marchese, S. Biamino, M. Lombardi, and P. Fino, "Application of directed energy deposition-based additive manufacturing in repair," Appl. Sci., vol. 9, no. 16, 2019, doi: 10.3390/app9163316.

[55]   T. Peng, K. Kellens, R. Tang, C. Chen, and G. Chen, "Sustainability of additive manufacturing: An overview on its energy demand and environmental impact," Addit. Manuf., vol. 21, no. June 2017, pp. 694–704, 2018, doi: 10.1016/j.addma.2018.04.022.

[56]   N. Guo and M. C. Leu, "Additive manufacturing: Technology, applications and research needs," Front. Mech. Eng., vol. 8, no. 3, pp. 215–243, 2013, doi: 10.1007/s11465-013-0248-8.

[57]   Optomec. URL:http://www.optomec.com/1/6 scale mixing nozzle for gas turbine exhaust for Bell helicopter .

[58]   K. S. Prakash, T. Nancharaih, and V. V. S. Rao, "Additive Manufacturing Techniques in Manufacturing -An Overview," Mater. Today Proc., vol. 5, no. 2, pp. 3873–3882, 2018, doi: 10.1016/j.matpr.2017.11.642.

[59]   Arcam Electron beam. URL:http://www.arcam.com/ technology/products/arcam-q10/.

[60]   Babak Kianian, "3D Printing and Additive Manufacturing State of the Industry, Annual Worldwide Progress Report," 2017. URL: https://wohlersassociates.com/2017report.htm.

[61]   R. Chang, K. Emami, H. Wu, and W. Sun, "Biofabrication of a three-dimensional liver micro-organ as an in vitro drug metabolism model," Biofabrication, vol. 2, no. 4, 2010, doi: 10.1088/1758-5082/2/4/045004.

[62] D. Garcia-Gonzalez, S. Garzon-Hernandez, and A. Arias, "A new constitutive model for polymeric matrices: Application to biomedical materials," Compos. Part B Eng., vol. 139, no. December 2017, pp. 117–129, 2018, doi: 10.1016/j.compositesb.2017.11.045.

[63] B. Vandenbroucke and J. P. Kruth, "Selective laser melting of biocompatible metals for rapid manufacturing of medical parts," 17th Solid Free. Fabr. Symp. SFF 2006, pp. 148–159, 2006.

[64] S. M. Peltola, F. P. W. Melchels, D. W. Grijpma, and M. Kellomäki, "A review of rapid prototyping techniques for tissue engineering purposes," Ann. Med., vol. 40, no. 4, pp. 268–280, 2008, doi: 10.1080/07853890701881788.

[65] O. L. A. Harrysson, O. Cansizoglu, D. J. Marcellin-Little, D. R. Cormier, and H. A. West, "Direct metal fabrication of titanium implants with tailored materials and mechanical properties using electron beam melting technology," Mater. Sci. Eng. C, vol. 28, no. 3, pp. 366–373, 2008, doi: 10.1016/j.msec.2007.04.022.

[66] D. Jafari, T. H. J. Vaneker, and I. Gibson, "Wire and arc additive manufacturing: Opportunities and challenges to control the quality and accuracy of manufactured parts," Mater. Des., vol. 202, p. 109471, 2021, doi: 10.1016/j.matdes.2021.109471.

[67] Pettersson V. "Study of the effect of process parameters in laser blown powder with superalloys: Varying laser power and scanning speed, analyzing material properties", MSc thesis, Department of Mechanical Engineering, Karlstads University, 2018, p. 80. URL:https://www.diva-portal.org/smash/get/diva2:1238212/FULLTEXT01.pdf

2 In-situ image processing for process parameter-build quality dependency in PTA-AM[1]

2.1 Abstract

Plasma transferred arc additive manufacturing (PTA-AM) is a high volume and high speed directed energy deposition (DED) technique that uses metal powder as a feedstock material to build up 3D components, layer by layer. In the PTA-AM process, the quality of the build is a function of several parameters, including but not limited to the powder feed rate, the torch travel speed, stand-off distance (SOD), and plasma arc current. Unlike the laser DED systems, the melt pool and laser visualization are not possible through inline imaging systems. These processes have difficulty sustaining uniform evenly distributed powder flow between the nozzle and the substrate. For the constant operating parameters, the process requires in-depth attention to inspect the quality and geometrical features of bead deposition, which may alter due to continuous mechanical connection with the deposition system. This paper provides a high-speed imaging approach to quantify and systematically analyze the process aspects of the PTA-AM system. The experiments of single-track multi-layer bead deposition of WC-reinforced NiCrBSi composites are carried out and recorded. The proposed image processing techniques are developed to optimize and validate stand-off distance (SOD) to print the stable bead and maintain the higher powder catchment efficiency at the deposition zone. It is also used to assess the impact of powder variation on the bead height. The powder stream distribution, the statistical dispersion of powder particle count, and their effect on the build quality are described based on powder flow images, using an image

---

[1] A version of this chapter has been accepted for Springer publication, International Journal of Advanced Manufacturing Technology as: "Gajbhiye R.; Rojas M.; Waghmare, P; Qureshi, A., (2021), In-situ image processing for process parameter-build quality dependency of plasma transferred arc additive manufacturing"

processing approach. The significance of relationships between bead height variation and powder particle counts are analyzed using statistical methodologies such as Analysis of Variance (ANOVA) and t-test. The effect of PTA-AM process parameters on bead geometry reveals that the plasma arc current and powder particle count significantly affect the bead geometry. This work validates the benefit of using 7 mm SOD for improving part quality. Using image analysis, the uniformity of powder flow is evaluated. In addition, the finding shows that the increment in plasma current by 40% increases the mean bead width by 85% and decreases its height by 24%. By determining the effect of processing parameters on the bead quality and geometry, this PTA-AM process can build near-net-shape parts and increase the reliability and reproducibility of the process. Thus, the proposed *in-situ* image processing methods can be adopted in the PTA-AM process to analyze manufactured parts' quality and characterize the process parameters responsible for the deviation in surface quality and dimensional geometry.

2.2 Introduction

Additive Manufacturing (AM) techniques build 3D components by adding the material in layers guided by a computer-aided design (CAD) model and associated computer-aided manufacturing (CAM) plan [1]. It prints the customized and intricate parts without conventional manufacturing steps such as casting mold, dies, or punching. It also remanufactures and repairs the damaged component by adding a layer to layer deposition of feedstock material [2]. One of the main categories of AM processes is the directed energy deposition (DED) method in which the energy source (i.e., plasma transfer arc (PTA), wire-arc, laser, or an electron beam) melts the feedstock material (i.e., wire, powder or both wire and powder) at their intersection point and forms the molten pool. The DED systems are classified based on energy sources such as laser-based, electron

beam-based, plasma-based, and electric arc-based DED systems. Based on the feedstock material it can be further divided into powder-feed and wire-feed DED systems [3].

DED is employed in AM to produce parts of metal-matrix composites (MMC), functionally graded material, and metal-ceramics, which are used in biomedical, aerospace, and defence industries due to its enhanced material properties (i.e., abrasion, corrosion-resistant, etc.), mechanical properties (i.e., tensile strength, hardness, Fatigue, etc.) and geometrical properties [4]. The variation in these properties is associated with the common defects that arise during the DED process, such as porosity, deformation, geometrical distortion, etc. The defect properties of AM components get influenced by various operating parameters such as energy source, powder/wire feed rate, travel speed of worktable/torch, stand-off distance, etc. [5], [6]. A diverse set of parameters, coupled with the complex thermal and momentum transport phenomena, limit our ability to understand the impact of these individual variables on the DED process [7]. With respect to ongoing advancements in DED systems, many researchers have been working on approaches such as analytical, thermal modelling, numerical simulation, statistical tests, artificial neural network (ANN), etc., to optimize the DED process by ascertaining the effect of operating parameters on deposit qualities.

In the laser-based DED (L-DED) system, the control of clad geometry is essential for commercial applications. To avail of this need, several researchers [8], [9] have constructed the optimization method for standard operating parameters such as powder feed rate, laser power, and scanning velocity. In the outcome measures, clad width and height were studied [8]. Thus far in theoretical studies, only a few mathematical models have been established to analyze clad geometry under the influence of powder feed behaviour with respect to stand-off distance [8] and powder transport

ratio, which validated with powder catching efficiency [9]. Further, the numerical models employed in L-DED were used to simulate the operating parameters, which include analysis of the powder stream shapes with respect to focal point positions, the effect of powder feed rate on laser beam intensity [10], clad geometry formation under the influence of laser power and scanning speed [11]. Moreover, the validation of statistical models has been achieved experimentally in the studies [12] using a high-speed imaging approach. The properties of streams, such as particles trajectory and velocity, powder stream distribution and focal plane position, were optimized in these studies [12]. In the same direction, Analysis of Variance (ANOVA) [13] and ANN using the machine learning approach [14] were also employed to predict clad layer geometry in the L-DED process. Besides, the in-situ monitoring using image signals with the visible and infrared spectrum, X-ray and acoustical signals is developed to enhance the defect detection in clad layers and repeatability of the L-DED process [15].

Like L-DED, the electron-beam DED (EB-DED) is also an AM process that prints a wide range of materials under a vacuum environment, unlike L-DED, which operates under an inert atmosphere [16]. Although a vacuum system is expensive, it offers tremendous advantages over L-DED, such as low residual stress, effective energy transfer to the substrate and high-speed scan rate [17]. In the EB-DED, the material microstructure also plays a crucial role because of the requirement posed by mechanical properties for the finished parts. Several works have been done to assess the impact of different processing parameters such as beam power, beam travel speed, beam focus and wire/powder feed rate on the mechanical properties and bead geometries [18]. The design of experiments approach used by Wallace et al. [19] highlighted that the process variables (beam power, beam travel speed) significantly impact bead width and height variation. In the same

study, it was also examined that the incident beam width changed the molten pool geometry without varying the microstructure of the deposits. In [20], the beam power and travel speed process map were developed using the finite element method to deposition a single-bead Ti6Al4V with the desired microstructure. Further, it also helped in achieving the proportional size scales between melt pool and beta grain widths [20]. In addition, the influence of deposition modes on the microstructure of Inconel 718 studied by [21] determined that the continuously deposited bead had greater yield and ultimate strength while intermittent deposited bead has superior plastic elongation property. Moreover, the high-quality build was achieved using the closed-loop control in the electron beam melting system, which provided deposit information via sensors to make immediate corrections [22].

As the EB-DED and L-DED are confined by higher cost and low efficiency, and thus suited better for manufacturing great-value and low-production parts, the wire and arc additive manufacturing (WAAM) is another DED process that has been used recently in the industry in view of high-efficiency and unique cost [23]. However, a significant problem associated with WAAM is the poor surface quality and low accuracy of the geometry created by extreme input power, high deposition rates, and large temperature gradients that occur during its process [24]. To address this query, recent experiments [25] have determined that bead surface quality and geometry can be improved by heat reduction. The Taguchi and ANOVA method used on experimental results by [24] revealed that increment in travel speed or decrement in current increases the roughness, independent of wire feed rate. As the optimization based on experimental results is time-consuming and expensive, the simulation modelling had been used in WAAM by various authors [26], in which accurate prediction of thermal behaviour on the bead, geometrical distortion,

residual stresses and mechanical properties were achieved in less time and cost. Further, to achieve the near-net deposition in WAAM, a forward and reverse model was developed by [27] that uses ANN to correlate the welding process parameters with single bead geometry. The Single-bead ANN model implemented with adaptive medial axis transformation (MAT) algorithm was able to deposit the accurate and void-free bead via an automatic selection of WAAM process parameters [28].

The plasma transferred arc (PTA) in the AM process has also been acquiring attention in scientific communities and the AM industry. The technology of PTA is counted as one of the fascinating additive techniques to fabricate the 3D parts through layer depositions by powder injection under the plasma arc [29], [30]. The PTA process had been recently employed in 3D plasma metal deposition, which is a category of DED process [31], [32]. As a promising technology, several ongoing studies have also been focusing on the effect of PTA processing parameters on geometrical and mechanical properties of deposits. In PTA-AM, characteristics that include the bead height and width, deposition rates, quality of bead, powder catching efficiency, melt pool dilution, and penetration level into the substrate depend on processing parameters such as arc current, voltage, travel speed, powder feed rate, shield/center gas flow [33], [34]. Mercado Rojas et al.[35] has confirmed that the PTA-AM system is capable of the mass production of WC-reinforced NiCrBSi 3D products for industrial applications. Another study by Mercado Rojas et al. [36], which is based on characterization of bead geometry and microstructural properties, showed that the bead height and width were significantly affected by the powder feed and gas rate, plasma arc current, and table travel speed. The printing of suitable quality components that encounter less deviation using optimized process parameters in PTA-AM is achievable with

minimum efforts required in post-processing. Further improvements in the final 3D metallic parts had been made by Moghazi et al. [37], which addressed the issues of oxidation and pore formations in the bead layer of 17-4PH stainless steel material. The study concluded that using 5% hydrogen in shield, center, and powder gas flow could avoid the oxidation in the layer and increment the heat input by 15 %, thereby eliminating porosity. Other researchers [38]–[41] have developed a micro-PTA-AM system to fabricate meso-sized parts, repair high-value components, and remanufacture defective products. Jhavar et al.[40] determined the correlation of good surface quality for multiple-layer depositions with optimized plasma energy and wire feed rate per unit of transverse length. Nikam et al. [38], [39] proposed a finite simulation model along with a thermal model to predict the single layer bead geometry using optimized parameters, i.e. plasma power, travel speed, wire feed rate, shielding gas flow, and thermal properties of melt pool and substrate. In addition to the effect of the above-mentioned process parameters, the influence of continuous and dwell-time mode multi-layer depositions has a significant impact on the deposit's microstructure, microhardness, and tensile properties [41].

Based on the reviews from the previous research studies done on the various DED systems (i.e., L-DED, EB-DED, WAAM, and PTA-AM), the PTA-AM has superior characteristics such as higher productivity, cost-effective, and low power consumption. Among the overlaying techniques, the PTA-AM proposes a higher deposition rate and efficiency, thicker overlays, and minimum dilution of substrate [42]. Multiple powder hoppers in the PTA-AM system provide the novel means to fabricate the parts of composite materials and functionally graded material [29]. For the above-mentioned advantages, the PTA-AM system has been recognized to manufacture the whole complex parts for industries such as mining and oil and gas industries [37]. However,

due to the complexity of the powder stream's ejection from the multiple nozzles, their interactions with the plasma arc, and in-process monitoring of the powder stream and stand-off distance effects on the quality of build is challenging. In addition, isolating the effect of operating variables on geometrical and microstructural properties has been difficult since build deposition is susceptible to minute changes in the process [43]. It is also stated that the deposited geometry can vary significantly with the same set of operating parameters between processing cycles on account of its high sensitivity towards process parameters [44]. Moreover, the difficulty in accomplishing the adaptive control, complex post-process assessment, expensive and time-consuming trial-and-error experiments, and accumulation of error in the processes makes it challenging to have a widespread implementation of DED to its full potential [7] [45]. As well as most of the experimental work in DED systems, including PTA-AM, focus on process parameters and build quality optimizations, which are described ex-situ, i.e., after the process is finished and fabricated part has cool down [46].

To overcome the aforementioned challenges, in-situ monitoring of AM process is essential for comprehending the physical phenomena that arise during the process and transmute them into process signatures which can signify the bead quality. Moreover, these process signatures can be controlled online using adaptive closed-loop feedback control in DED systems. Despite the various effort in using high-speed imaging and image processing approaches for monitoring and optimizing the different DED processes, minimal attempts have been reported on the image processing approach used in the PTA-AM system for process optimizations. Therefore, the present work attempts in the PTA-AM process to develop in-situ image processing technique for process parameter-build quality dependency.

Figure 2-1 shows the schematic of the PTA-AM process. The plasma arc is used as the energy source to melt the powder particles as a feedstock material on the substrate, and repetition of this deposition process layer by layer produces the complete 3D solid part. In this PTA-AM system, the arc is restricted with a small diameter by using a water-cooled copper nozzle, but the power density is higher as compared to other arc welding methods [14]. The choice of the powder as a feedstock material in the process arises with the flexibility in using the desired composite coatings, overlays with different alloys composition and difficulty in producing the required diameter of a wire, as a form of feedstock material which is especially crucial for the efficient methods [47], [48].
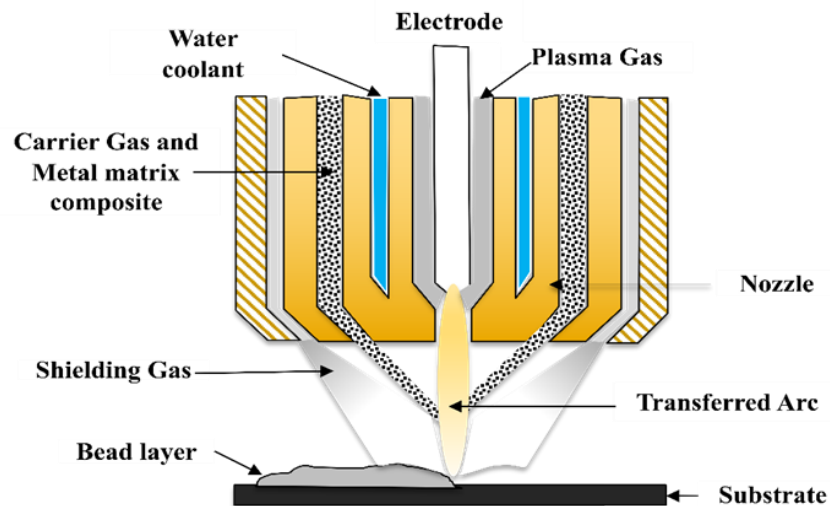
Figure 2-1 Schematic of PTA-AM system

Noteworthy prior works have been done using an in-situ imaging system to develop advanced process monitoring procedures for faster mechanization of DED in the manufacturing industries. The in-situ high-speed X-ray imaging system used in the piezo-driven L-DED system revealed the laser beam-powder flow interaction and their effect on porosity and cavity formation during the

deposition of Ti-6Al-4V material [49]. With the same setup, Webster et al. [50] evaluated the Ti-6Al-4V powder flow-melt pool interactions with the key finding such as laser beam attenuation into the molten pool zone due to increment in powder feed rate, the effect of particle velocity's on melt pool quality, phase transformation of powder as well as various porosity formations. The above literature provides insight into the fundamental physics of powder flow interaction with a laser beam and with a melt pool. However, these DED processes are still far from imitating components from real industrial DED systems; therefore, further research development is required to implement them into the industries [7]. In addition, the use of the charge-coupled device (CCD) or complementary metal-oxide-semiconductor (CMOS) high-speed cameras has been cited in different studies for monitor and controlling the DED systems. Lott et al. [51] have developed the CMOS camera-based optical system for in-situ monitoring of laser beam velocities and implemented the image processing technique to demonstrate molten pool variation. However, in the proposed method, the influence of process parameters for molten pool dynamics is not clearly illustrated. Fathi et al. [52] presented a CCD coupled vision-based proportional–integral–derivative controller system to monitor a clad height under the influence of process conditions. However, only the scanning velocity was used as the input parameter to compensate for the deviation in deposition height. Later, Mozaffari et al. [53] have advanced the previous work by including the Particle Swarm Optimization and Pareto-based evolutionary algorithms for real-time melt pool prediction and optimization of process parameters, respectively. With this system, the authors demonstrated the clad height and dilution under the influence of scanning speed, laser powder and powder flowrate.

As per the author's view, no work reported on the *in-situ* image processing technique used in a plasma-based DED system to investigate the correlation between processing parameters and the bead quality and geometry. Thus, this study uses the *in-situ* image processing methodology in the PTA-AM to systematically compute the image-based powder measurement and detect the bead geometry variation in the deposition zone. In order to understand the impact of PTA-AM process parameters on bead geometry, statistical techniques such as ANOVA and the two-tailed t-test have been used to estimate the significance of the linear relationship between powder particle count and bead geometry. In addition, the effect of plasma arc current on the bead height and width has been determined in this study. The proposed *in-situ* image processing methods can be well-defined measurement guideline to monitor PTA-AM process stability and ensure the optimum level of processing parameters for the stable build deposition. The outcome of this research work will be valuable for the optimization and validation of process parameters and deposition of the stable bead with lesser deviation manufactured by the PTA-AM process. The process and product characteristic optimizations using image analysis will help reduce material waste in a repetition of expensive experiments and increase the stability and reproducibility of the process.

2.3 Experimental and optical setup

The main equipment used in the process is an experimental PTA-AM system developed in-house consisting of a Kennametal StelliteTM STARWELD 400A PTA (Pittsburgh, USA) source, installed with Kennametal Stellite Excalibur II Torch [36]. The torch features a high-efficiency 3.18 mm (1/8 in.) nozzle with two powder ports and a self-centering thoriated tungsten electrode that is honed to an angle of 20°. The Excalibur torch is the transition point where plasma arc is used to melt powder particles carried by argon gas from the hopper to the nozzle exit. The

employed light source for illumination was a 1.2-kW HMI PAR Arrisun 12 plus (New York, USA).
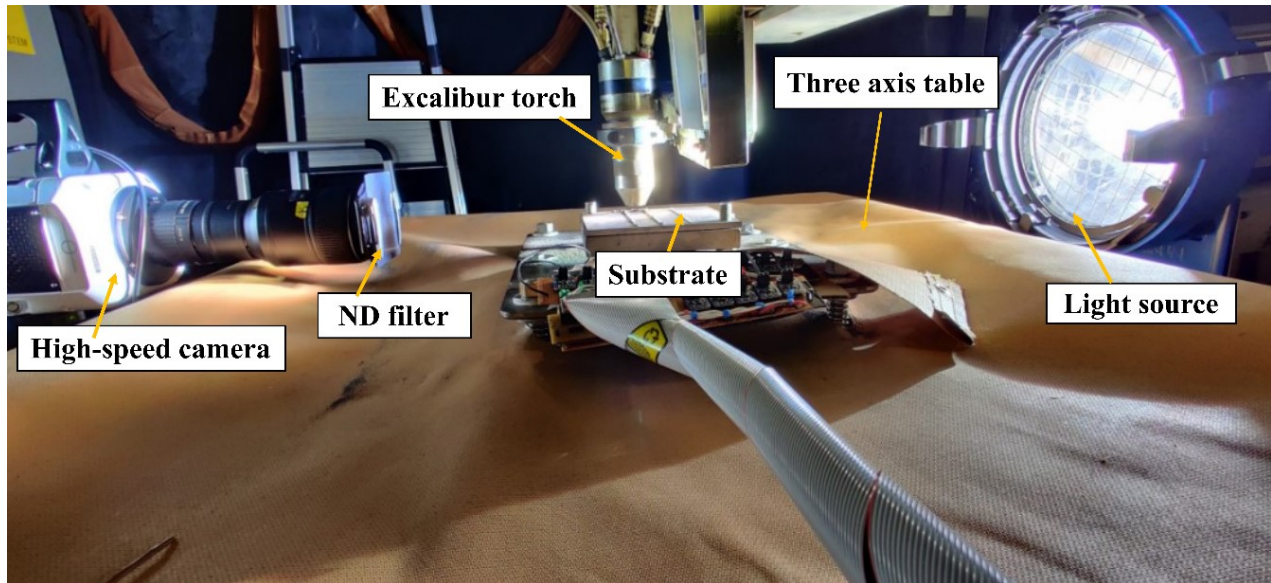
Figure 2-2 Experimental and optical setup of PTA-AM system

The torch is fixed at one position, and the substrate moves in three dimensions guided by a CAD model. The powder streams from both nozzles and deposited layer height on the substrate are recorded with CMOS high-speed camera (Vision Research, Phantom V711) mounted with long-reach macro lens assembly (AF-S Micro NIKKOR 105 mm f/2.8). This high-speed camera could provide up to 68,000 fps. The sensor size is 1280×800 pixels, where pixel size is 20 μm $\times$ 20 μm. A neutral density (ND) filter is used in front of the camera lens to suppress the plasma arc radiation and the weld pool brightness. The frame rate, exposure time, and spatial resolution are carefully chosen in this study to capture the powder flow distribution and complete bead deposition under the plasma arc intensity without losing the relevant information and to capture a high-speed image stream that can be computationally feasible for the image analysis implementation. With this aim,

the sampling frequency of 100 fps and 4 µs exposure time is selected, corresponding to a spatial

resolution of 1024 × 768 pixels.
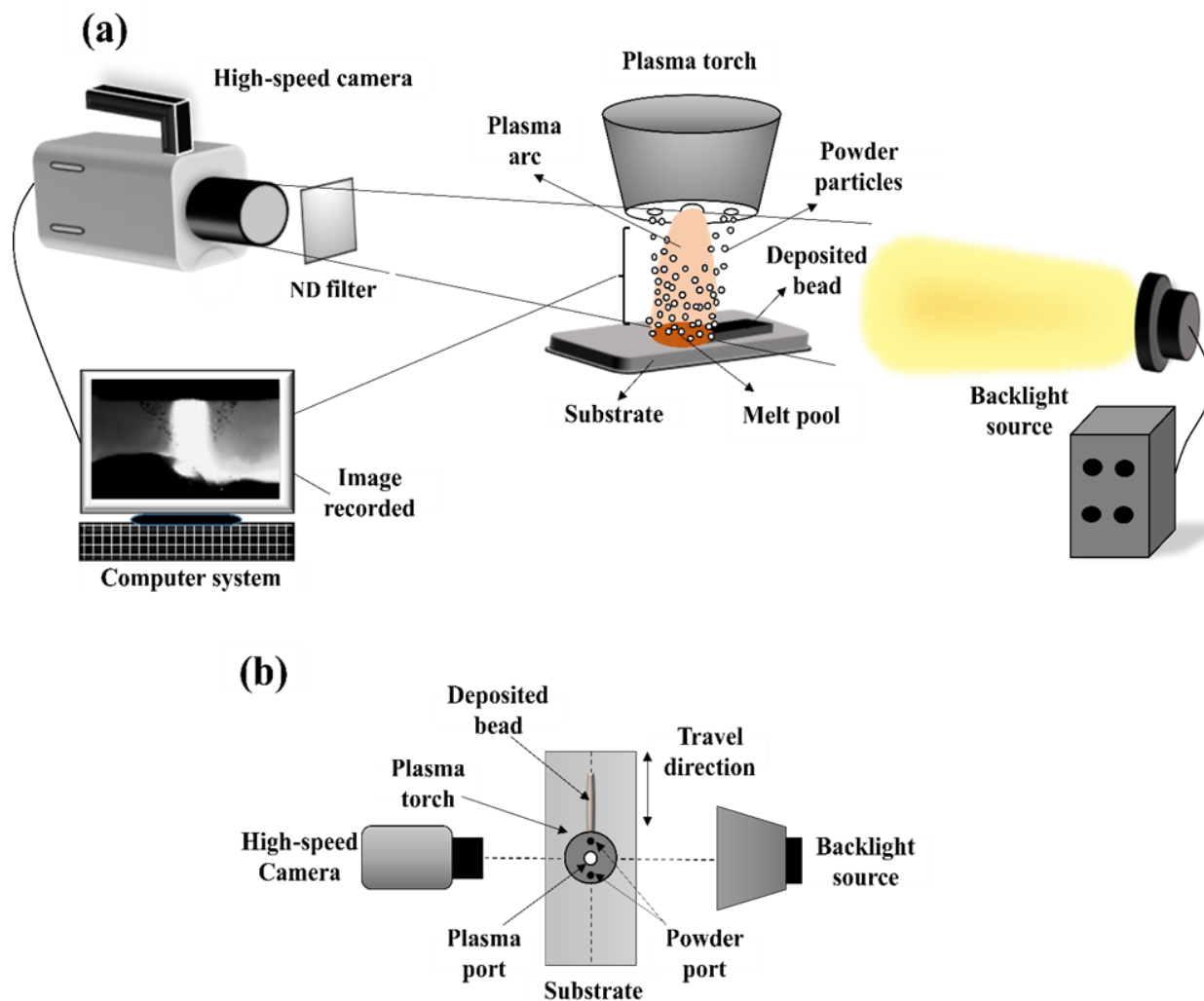
Figure 2-3 (a) Schematic of Optical setup with PTA-AM system (Isometric view) (b) Top view of an optical setup

Figure 2-3 (a) depicts the optical setup used in this study. The high-speed camera is fixed on the

tripod (Manfrotto, Italy) to focus on powder streams injected from both powder ports. The

backlight source is placed to illuminate the powder particles from the backside. The Neutral

Density (ND)-4 filter is inserted in front of the camera lens, which reduces the 1/10000 amount of plasma arc light entering the lens. The field of view of the high-speed camera has been fixed to a certain height of observation by keeping the camera sensor perfectly aligned with the substrate. Figure 2-3 (b) shows that the high-speed camera is aligned with and pointed towards the backlight source. Both are perpendicular to the moving direction of the substrate and powder port plane. The depth of field is correctly adjusted to provide an in-focused image of powder streams in a plane perpendicular to the camera and in-line with the powder deposition ports of the nozzle together with bead deposition.

Table 2-1 Chemical composition ranges for tungsten carbide and MMC [54]

Product	Hard Phase composition (wt. %)			Matrix alloy composition (wt. %)						
	Phase	W	C	Phase	Ni	Cr	B	Si	C	Fe
	%			%						
PlasmaDur 51122	60	93.8	6.0	40	Bal.	9.5	2.0	3.3	0.3	2.0
		94.0	6.2			12.5	2.5	4.3	0.6	3.5

The powder material is the pre-blended mixture of tungsten carbide, and nickel-based metal matrix composites (MMC) sourced from OErlikon Metco [54], and the powder product name is PlasmaDur 51122. The particle size distribution is + 63 to – 180 µm with apparent density ranging from 5500 to 7000 kg/m^3. The tungsten carbide is an angular shape, whereas MMC is in spheroidal shape. Table 2-1 represents the chemical composition of powder material.

2.4 PTA-AM processing parameters

Table 2-2 provides the PTA-AM process parameters with their corresponding values. Experiment 1 is mainly performed to investigate the spatial distribution of powder flow field along the nozzle axis and to optimize the stand-off distance (SOD) for the deposition of the stable bead using the image processing technique.

Table 2-2 Main processing parameters for experiments

Sr. No.	Process Parameters	Experiment 1	Experiment 2 (S1 , S2 , S3)	Experiment 3 (S1 , S2 , S3)
1	Plasma arc current (Amp)	100	100	60
2	Powder flow rate (gram /min)	45	27	27
3	Travel speed (mm/ min)	100	600	600
4	Stand-off distance (SOD) (mm)	12	7	7
5	Powder gas (slpm)	1.5	1.5	1.5
6	Center gas (slpm)	1.5	1.5	1.5
7	Shield gas (slpm)	12	12	12

Experiments 2 and 3 are conducted to determine the influence of powder particle count on the bead height variation. Three samples named S1, S2, and S3 are performed with the same processing parameters under experiments 2 and 3, respectively, to evaluate the variation in the process. The plasma current is decreased by 40%, with other parameters kept constant to investigate the influence of current on the bead geometry.

2.5 Image processing methodology
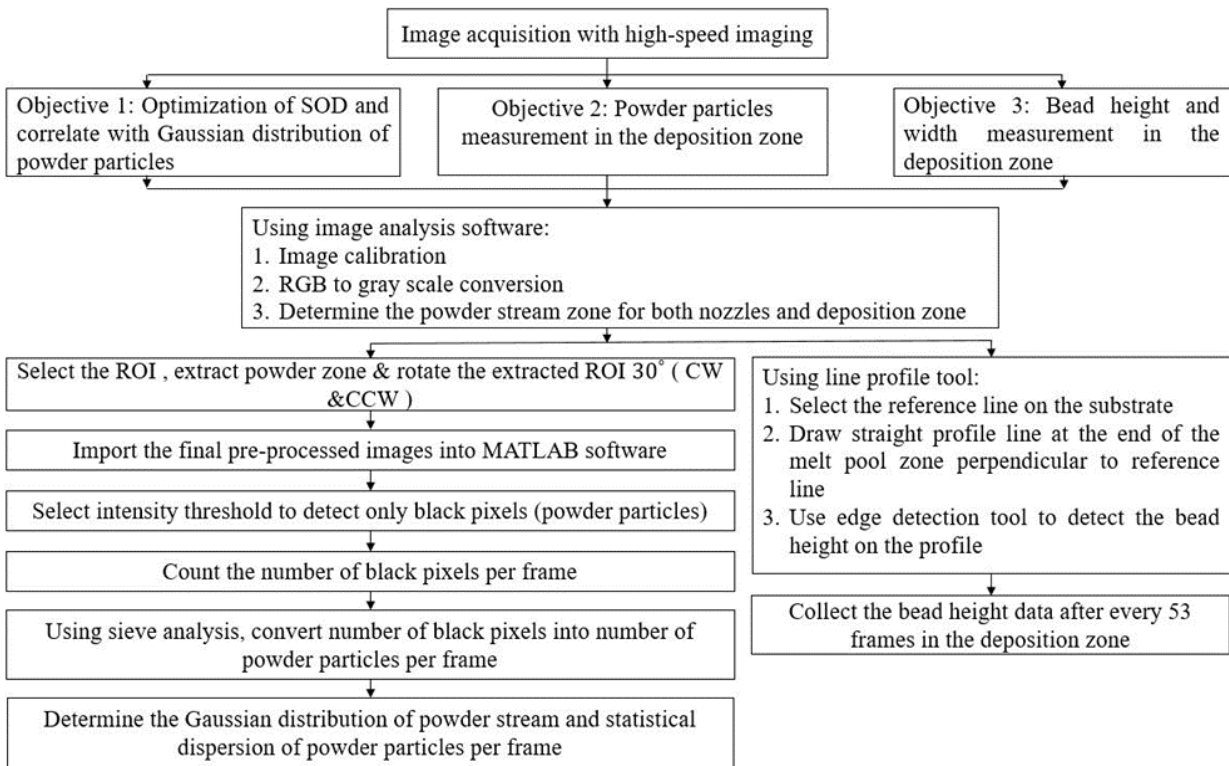
Figure 2-4 Flow diagram of the proposed image-processing method.

Figure 2-4 presents a flow diagram showing the method for estimating the Gaussian distribution of powder particles, optimized stand-off distance (SOD), powder particle measurement per frame, and bead height measurement per frame for every analyzed layer using the proposed image-processing method. Based on objectives in the current study, the flow diagram contains three different series of image processing steps. The proposed methodology begins with acquiring a series of high-speed images and importing them into the image analysis software Image-Pro 10 for pre-processing images. The spatial calibration of the images has been used to convert the dimensions from pixel to millimetre measurements. The corresponding pixel size based on the image resolution is 20 μm × 20 μm, and the magnification factor was determined as 0.0125 mm/pixel. The grayscale images were extracted from the high-speed RGB images to identify the

powder particles and beads (black pixels in the image). The spatial calibration and image aspect ratio enables us to determine the powder stream zone and melt pool zone. A region of interest (ROI) is extracted from the series of images to calculate the Gaussian distribution of powder stream and powder particle count per frame. The pre-processed images are imported into the MATLAB software to detect only black pixels below a threshold.

The sieve analysis of powder size distribution provided by the powder's manufacturer is then used to convert the powder black pixels into the powder particle count in the metric unit. The bead height variation in the melt pool zone is measured per frame using the line profile tool provided in the image analysis software. The line profile provides the edge detection tool, which measures the pixel intensity change (black to white pixel) along the line drawn in the melt pool zone of the images. An overview of the significant image processing steps of the proposed methodology is presented in Sections *2.5.1* and *2.5.2*. In addition, one of the objectives, i.e., optimization of SOD for good quality deposition using image processing methodology, is explained further in Section *6.1.1*.

2.5.1 Powder particle distribution and measurement method

Figure 2-5 depicts a schematic of a number of deposited layers i (i = *1,2,3,4,5*) on the substrate, and n is the number of high-speed images that have captured the whole bead layer i and the number of powder particles deposited to build the corresponding bead layer. The image stream acquired during the deposition of bead layers can be signified as a series of images which are I = $\{I_1, I_2, I_3 ..., I_n\}$, where I_n is the nth image of size 1280 × 800 pixels. 550 consecutive frames capture the single-layer bead deposition, which was processed in the developed algorithm. The

grayscale images are an 8-bit per pixel in which the pixel intensity ranges from 0 to 255, where 0 is black, and 255 is white.
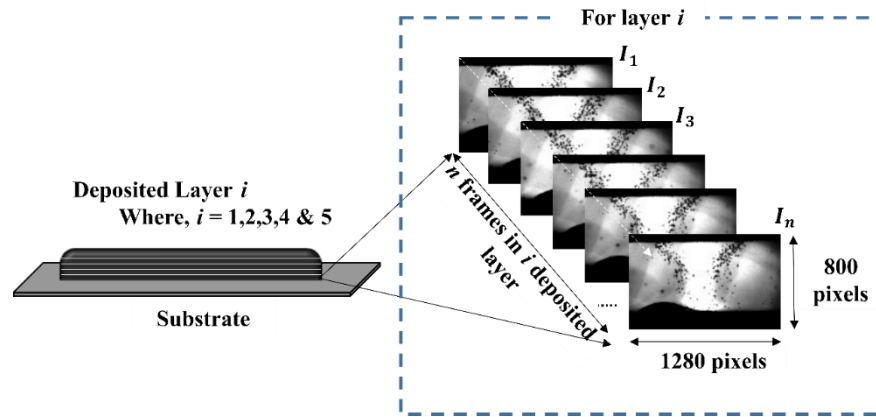
Figure 2-5 Example of an image stream containing n frames of 1280 × 800 pixels in the bead layer *i*

The angle at which images are rotated is decided on the powder injection angle, which is around 60°. The re-orientation has been done for vertical translation of powder streams distribution at the deposition zone. The powder flow distribution along the nozzle axis in the newly oriented images is aligned with the plasma arc axis and center of the melt pool zone. The re-orientation of images made it convenient to correlate the projected powder stream distributions with respect to bead height variation in the deposition zone. As shown in Figure 2-6, the image processing methodology is explained in steps to determine the powder stream distribution and powder particle measurement. The pre-processing of images was done in the image analysis software (Image-Pro 10). The image calibration has been done using the center-to-center distance between the nozzles, which is 8 mm. A suitable size of two red-coloured rectangular windows is the region of interest (ROI) selected to extract only the region of powder flow ejected from both nozzles. The region of interest has been used in image processing to segment powder streams from the raw high-speed images and remove the unwanted portions of the images, as a result, reduction in the processing

time and complexity. The segmented powder stream images were re-oriented using a rotation of image at $30°$ (clockwise for nozzle 1 and anti-clockwise for nozzle 2 with respect to plasma center axis).
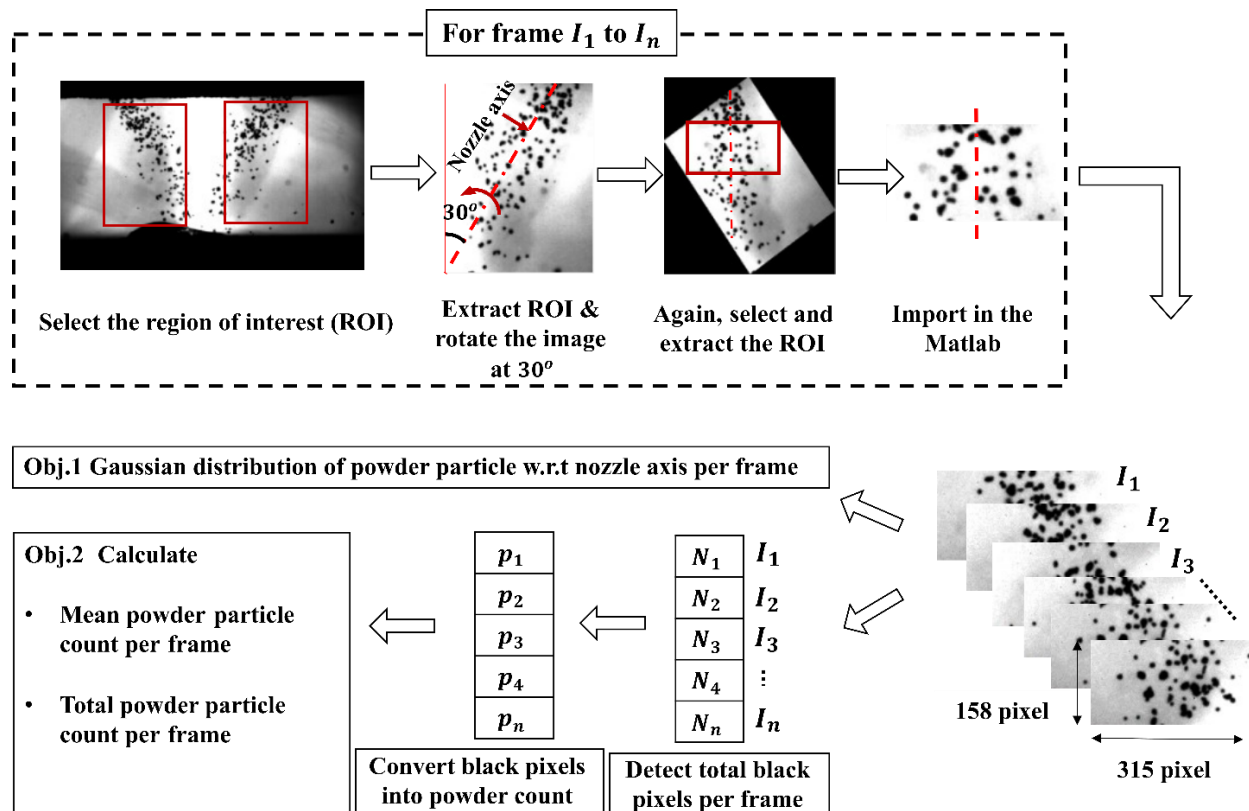
Figure 2-6 Stepwise image processing method for powder particle detection in the image stream and powder particle count per frame

A small ROI of size 315×158 pixels on the series of images has been defined for image processing. The size of the ROI region is decided in such a way as to detect the maximum distribution of particles as well as to crop the unwanted plasma arc region and black background region from the images. The final segmented image stream was imported into the MATLAB toolbox. The threshold value of the grayscale is estimated manually in the image analysis software. In order to binarize an image, the threshold is set at the point where all of the black pixels (powder

particles) have been detected and applied to the stream of images. The particles are detected in the binarized image data by counting the same value unit of attached black pixels. The total black pixels detected per frame are converted into a number of powder particles per frame by dividing the average area of a powder particle diameter of 71 μm. The total powder particle count per deposited layer and mean powder particle count per frame has been determined using the aforementioned image processing technique. In addition, the positions of the black pixels per frame are known, which have been used to calculate the Gaussian distribution of powder particles alongside the central nozzle axis and across the powder stream area.

2.5.2 Bead height measurement in the deposition zone

A typical high-speed image captured the powder stream and bead height with an eight-bit grayscale is presented in Figures 2-7, from which the bead layer height can be clearly seen. The image analysis software Image-Pro 10 has been used to detect the location of both the nozzles, powder injection angles, powder stream central axes (blue hash dot lines), and powder stream spatial distributions (blue lines) with respect to their deposition zone on the substrate. The mentioned software performs the measurement operation in terms of pixel positions in the image, and these pixel-level measurements can be converted into scaling units using spatial calibration.
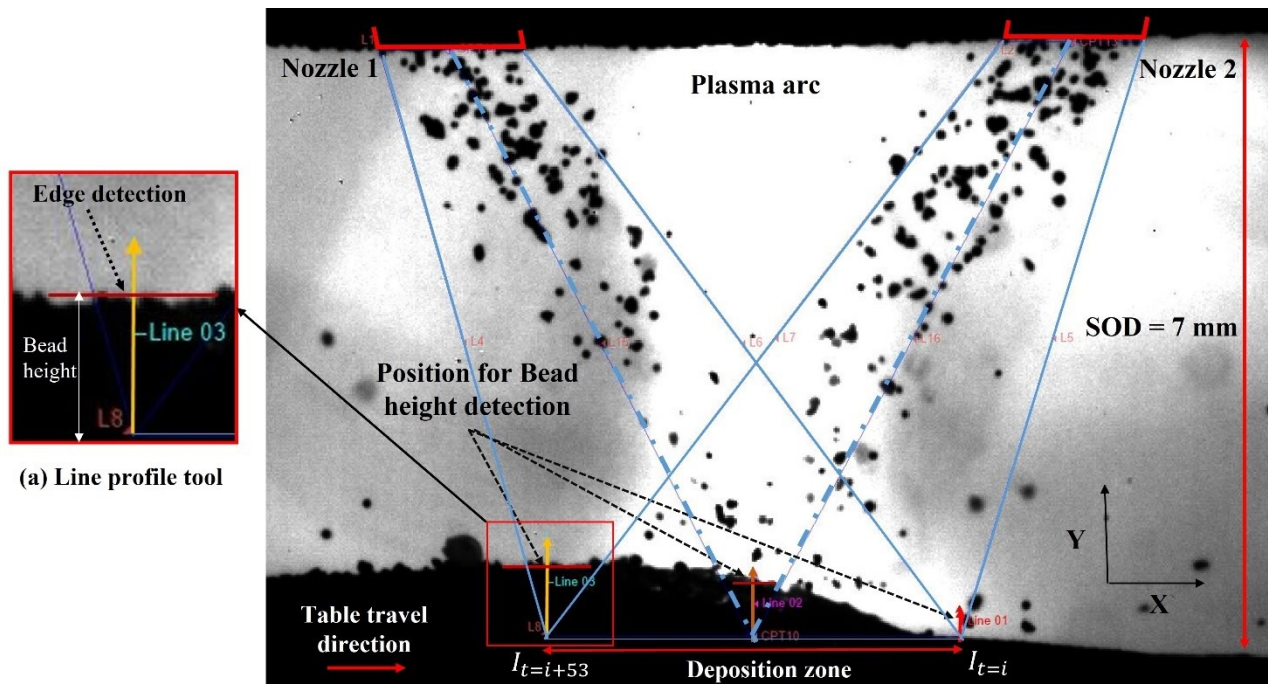
Figure 2-7 Image processing technique for bead height detection after every 53rd frame in the deposition zone to correlate the mean powder particle counted from 53 frames with bead height variation at every 53rd frame

In addition, the height tracking of whole beads was achieved using the processing of high-speed images into the image analysis software. The Line Profile tool provides the edge detection at the intensity change of greyscale pixels along the drawn line in the image. As shown in Figure 2-7, the reference is taken on the substrate plane, and the line tool is drawn perpendicular to the reference at three different points on the substrate, which are positioned at the starting point, the middle point and the endpoint of the deposition zone to detect the layer height. As shown in the detailed image Figure 2-7 (a), the edge of the bead is detected with the red line, and the bead height in between is measured from the substrate plane along the yellow line. As the PTA-AM table moves with a speed of 600 mm/min in the direction of the x-axis, the substrate located at starting point of the deposition zone $[I_{t=i}]$ travels under the powder stream and plasma arc region. The bead layer is formed on the substrate by the impingement of powder particles, which are melted by the energy of the plasma arc. The gradual increment in the bead height is observed from the

point $[I_{t=i}]$ at which bead deposition starts to the point $[I_{t=i+53}]$ where deposition reaches the maximum height as the table moves forward, and beyond this point, the layer height remains constant due to the end of the powder deposition zone and the plasma arc zone. With the available information of table travel speed, image frame rate and deposition zone distance, the time required to reach the deposition zone endpoint $[I_{t=i+53}]$ from the deposition zone start point $[I_{t=i}]$ is calculated. It is computed that a time period of 53 frames (0.53 sec as per 100 fps) has been taken to cover the distance of the deposition zone, as shown in Figure 2-7. Therefore, at the deposition zone, the variation in bead height is detected after every 53rd frame to evaluate the variation in the amount of powder deposition and their effect on the bead layer variation. The detection of bead height at point $[I_{t=i+53}]$ per frame and total powder particle count per frame can be estimated using the image processing technique. This study determined the correlation between the bead height variation at every 53rd frame and the accumulation of total powder particles detected in those corresponding 53 frames.

2.6 Results and Discussion

2.6.1 Powder flow structure and deposition zone

Figure 2-8 depicts an average grayscale image of five hundred high-speed images with a time interval of Δt between two consecutive images, which is an average time for the powder particles to travel from nozzle exits to the substrate. For finding the spatial distribution of powder streams, an average image of 550 of the sample images is considered, with a certain angle of divergence from the exit of the nozzle to the deposition zone on the substrate.
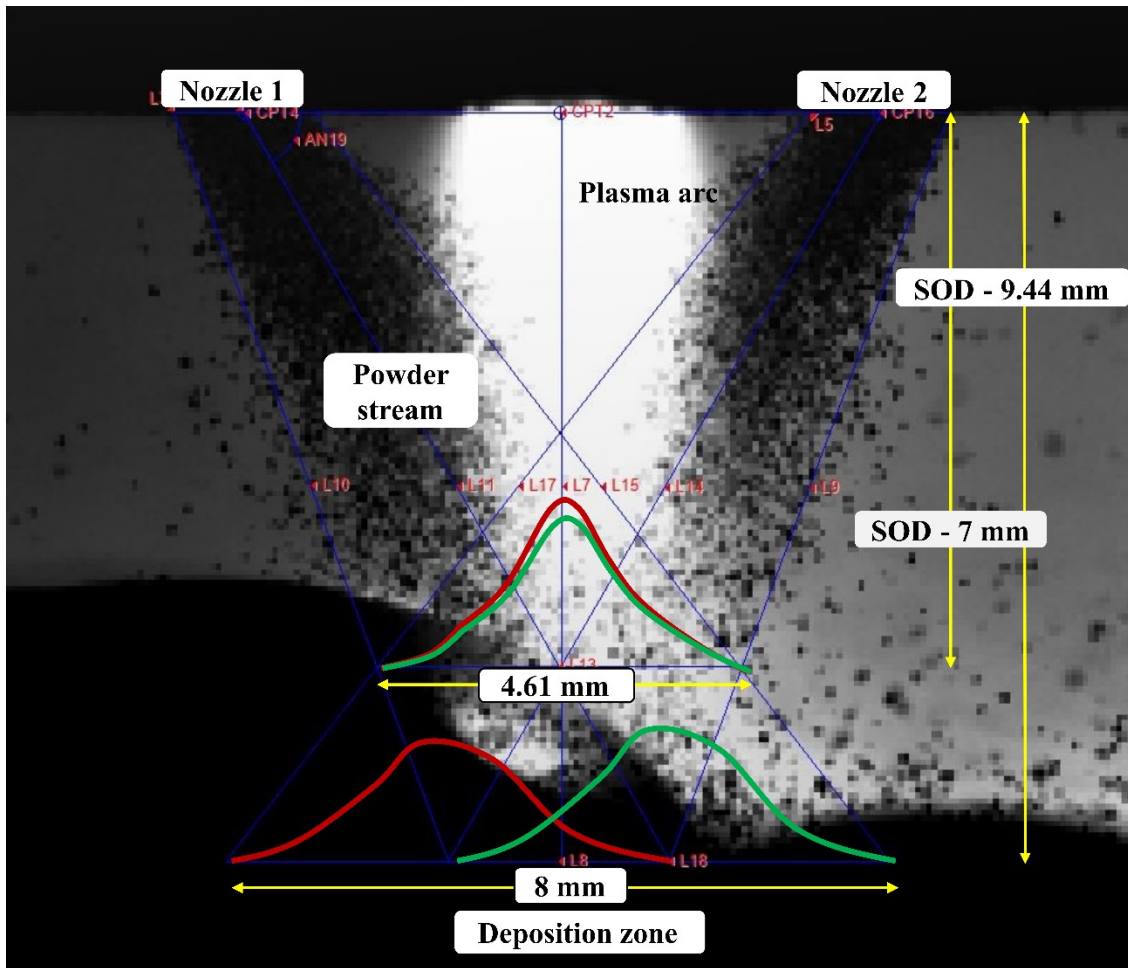
Figure 2-8 Schematic diagram represents the Gaussian distribution of powder flow streams and their concentration distribution at different SODs along the plasma arc axis

The powder particles follow a parabolic trajectory motion under the gravity effect, with a particular initial velocity. The divergent powder stream generally complies with the Gaussian distribution [55]. The image analysis method is used to investigate the powder flow distribution within the cross-section of the powder stream, which is perpendicular to the nozzle axis. In addition, the powder flow coordinates, melt pool zone and SOD are determined using arithmetic operation in the image analysis.

The powder stream distribution has been determined based on the following assumptions:

1. The Gaussian distribution of powder flow is symmetrical along the nozzle axis, and at every cross-sectional plane of powder flow, it follows the same Gaussian trend.

2. The divergent powder stream cone is similar for both nozzles, and it is symmetrical along the nozzle axis.

3. The effect of gravity and drag force on the powder particles is considered.

4. Powder particle size distribution is uniform, and particles have spherical morphology.

5. After powder injection, particle-particle interaction is neglected.
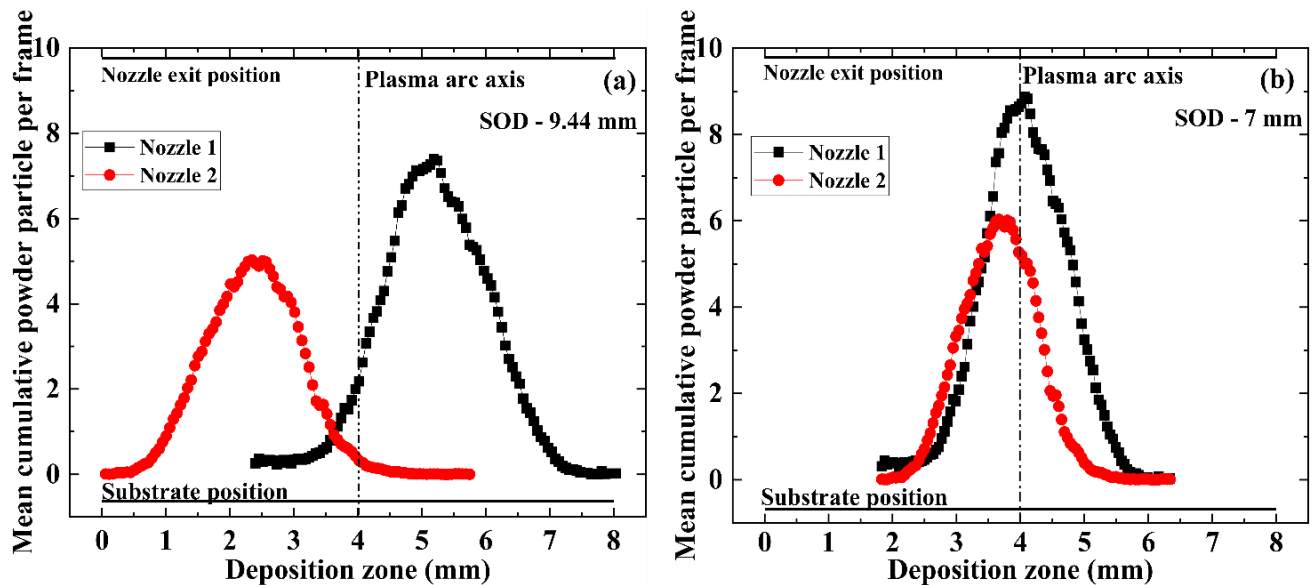
Figure 2-9 Gaussian distribution of powder streams incoming from nozzle 1 and 2 and variation in powder concentration distribution at the SOD of (a) 9.44 mm and (b) 7 mm along the plasma arc axis

The schematic diagram (Figure 2-8) shows the distinctive pattern of Gaussian distribution of two powder streams and variation in deposition zone at different SOD planes. It is projected that the powder stream distributions follow a 'saddle' pattern, overlapping with each other as SOD decreases.

The Gaussian distribution pattern of powder streams is shown in Figure 2-9 (a - b). By the law of mass conservation, it is expected that the total area under the Gauss curve of mean powder particle count at SOD of 9.44 mm is equal to the total area under the curve at SOD of 7 mm. Fig 2-9 (a) depicts that the peak of the powder stream distributions has deviated approximately 1.5 mm from the center of the deposition zone, which is 8 mm long, and the Gaussian distribution of two powder streams follow a saddle-shaped profile which can be the reason for the deposition of two low-quality beads rather than one uniform stable bead. As the SOD decreased to 7 mm, as shown in Figure 2-9 (b), the Gaussian peaks are almost aligned with the center of the deposition zone, which is 4.61 mm long and overlapping of powder streams distribution can conclude the merging of two powder streams into one which is an essential factor for the deposition of the single stable bead. It is also determined that as the SOD decreases, as shown in Figure 2-9 (a - b), the deposition zone decreases from 8 mm to 4.61 mm, which is almost covered by the plasma arc region (Approx. 4 mm wide). Statistically, it can be predicted that around 96% of the deposition zone falls under the plasma arc region at SOD of 7 mm. In contrast, only 50% of the deposition zone is covered by the plasma arc region at the SOD of 9.44 mm. It provides the clear insight that as the SOD decreases, the chance of powder catchment in the deposition zone under the plasma arc region increases.
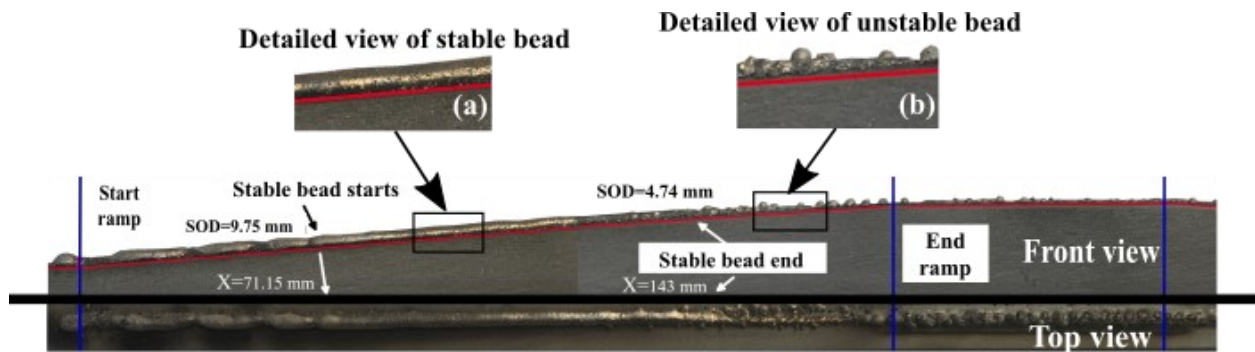
Figure 2-10 Deposition of bead layer over ramp geometric benchmark test artifacts (GBTA), at specific SOD, the deposition bead gets uniform surface [56]

It is known that SOD plays a vital role in bead quality. The effect of SOD on the bead height variation is experimentally evaluated by Mercado et al. [56] using the Geometric Benchmark Test Artifacts (GBTAs). The GBDA is specifically designed in the study to assess the uncertainties and build the bead deposits with different characteristics in the AM process. Using the processing parameters such as powder feed rate of 40 gram/min, plasma current of 50 Amp and table speed of 500 mm/min, the single-track single layer bead is deposited over the GBTA to measure the bead height and degree of deviation in the layer height with respect to SOD variation. The SOD between nozzle exits and GBDA starts from a maximum value of 13.15 mm to a minimum value of 2.54 mm. The nozzle position is fixed while the GBDA travels in the x-direction under the plasma arc and powder streams, and this arrangement gives a variety of SOD ranges for the bead deposition. In Figure 2-10, it can be noted that as the ramp GBDA starts at the maximum SOD value of 13.15 mm, the unstable bead deposition is observed till the SOD value of 9.75 mm. The beads stabilize at the SOD of 9.75 mm, where the two beads from individual powder nozzles merge into one stable bead with fewer deviations [Figure 2-10 (a)]. The stable bead again starts to split into two low-quality beads with some deviations at the SOD of 4.74 mm [Figure 2-10 (b)]. The uniform bead with less variance is achieved between the SOD ranges of 9.75 mm to 4.74 mm. In addition, the

Mercado et al. [56] has confirmed experimentally that the good quality bead deposited at the SOD of 7 mm with lesser deviation, which is relatively similar to the SOD, was estimated in the current study using an image processing method at which Gaussian distribution of the dispersed powder is overlapped which can be responsible for the deposition of uniform bead [Figure 2-9 (b)].

2.6.2 Statistical dispersion of powder particle count

Figure 2-11 shows the statistical distribution of the mean powder particle count per frame for the number of deposited layers. The x and y axes signify the number of deposited layers and the mean powder particle count per frame. Three different samples [S1, S2, and S3] are analyzed at a 100 amp and 60 amp plasma current for Expt. 2 and Expt. 3 respectively while other processing parameters were kept constant. The dispersion of mean powder particle counts per frame was summarized for five consecutive deposited layers in each sample experiment. Figures 2-11 (a), (c), and (e) show distribution of data for three samples (Expt.2) reveal that the interquartile spacing, median value and max-min range of mean powder particle count per frame with respect to deposited layers are nearly similar for all three samples. The mean powder particle count per frame for the samples S1, S2, and S3 from Expt. 2 is 66 ± 3, 65 ± 1, and 62 ± 4, respectively. Also, the maximum value of mean powder particle count is 95 ± 3, 99 ± 1, and 94 ± 4, and the minimum value is 33 ± 3, 32 ± 1, and 30 ± 2. From the comparison, it can be determined that the powder stream is almost constant with less variation for all three different samples. Similarly, Figures 2-11 (b), (d), and (f) represents the statistical distribution of data for three more samples (Expt. 3). The mean powder particle count per frame for S1, S2, and S3 from Expt. 3 is 76 ± 2, 70 ± 1, and 69 ± 2, respectively. Likewise, the maximum value of mean powder particle count is 105 ± 4, 100 ± 3, and 103 ± 3, and the minimum value is 37 ± 2, 37 ± 3, and 36 ± 2. It is also observed that the

interquartile space, median value, and max-min range of the data set against the deposited layers are closely identical, which shows consistency in the powder flow.

Expt.2 and Expt.3 are operated at the constant powder feed rate of 27 grams/min. The statistical distribution for the same experiments investigates that the interquartile spacing and max-min range of powder particles are almost equal. However, the overall mean and median shift can be observed in the Expt. 3 samples in comparison with Expt. 2 samples. This uncontrollable variation of mean and median values might be due to the process being more susceptible to disruptions and can be affected due to the influence of other governing parameters, including but not limited to the carrier gas flow rate, shielding gas flow rate.
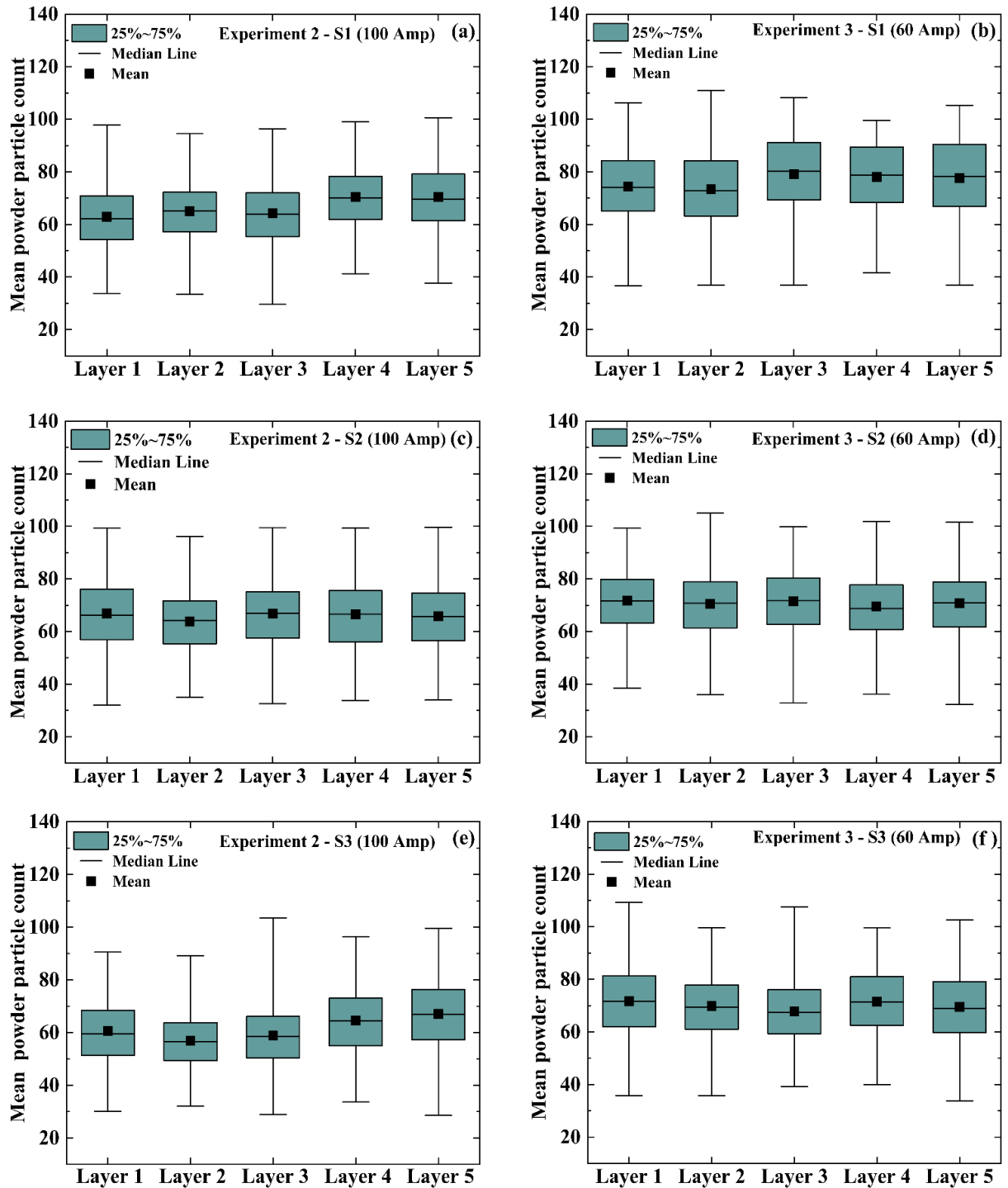
Figure 2-11 Box-and-Whisker plot represents the mean powder particle count per frame for three different samples (S1, S2, S3) in Experiment 2 (100 Amp) and Experiment 3 (60 Amp), respectively.

2.6.3 ANOVA of experimental samples

The variation in bead height with respect to total powder particle count for three different samples performed at a plasma current of 100 amp is shown in Figure 2-12. The linear regression is applied between the independent (*x*-axis) and dependent variable (*y*-axis), representing the total powder particle counted for 53 frames and bead height variation at every 53rd frame, respectively. In the regression equation ($y = a + b*x$), y is the measured bead height in mm, x is the powder particle count, a is the *y*-intercept, and b is the slope of a regression line. The Analysis of Variance (ANOVA) evaluates the significance of linear regression with a 95% level of confidence (the test level is p-value < 0.05). For all three samples, the range of bead height variation is between 0.6 – 0.9 mm against the total powder particle count range of 2700 – 3700.

Figures 2-12 (a), (c), and (e) show the separate linear fit applied for individual layers. It is concluded from the ANOVA test that four out of five layers for sample S1 have a p-value < 0.05, which explains that 95% variability of bead height data can be presented with the linear fit model. Moreover, three out of five layers have a p-value less than 0.05, which signifies the linear relationship for samples S2 and S3. Figures 2-12 (b), (d), and (f) indicate the concatenated linear fit applied for all layers' data set together and the ANOVA test is performed to evaluate the overall significance of the model. It has been investigated that all three samples have a p-value less than 0.05, which explains that bead height variation data can be predicted from the linear regression model.

The variation in bead height with respect to total powder particle count for three different samples performed at a plasma current of 60 amp is shown in Figure 2-13. The linear regression is applied

between the x and y axes, representing the total powder particle count for 53 frames and bead height variation at every 53rd frame, respectively. The ANOVA is performed to determine the significance of the linear relationship between independent and dependent variables. For all three samples, the range of bead height variation is between $0.8 - 1.1$ mm against the total powder particle count range of $2700 - 3800$.

Figures 2-13 (a), (c), and (e) show the separate linear fit applied for individual layer data sets. The ANOVA analysis examined that four out of five layers for all three samples have a p-value less than 0.05, and it explains that the 95% bead height variation in the data can be predicted from the regression model. Moreover, Figures 2-13 (b), (d), and (f) indicate the single linear regression model based on all layers' data sets together. It is observed based on ANOVA analysis, the p-value is less than 0.05 for all three samples, and it concludes that the linear relationship between bead height variation and total powder particle count is statistically significant.

Additionally, for the constant powder feed rate, Figures 2-12 and 2-13 observed the height variation between five individual bead layers. It could be due to the thermal histories of the interlayers that bead heights fluctuate. As thermal dissipation varies along the bead height and dwell time between two successive deposit layers, the bead geometry of the first few layers changes, thus resulting in arc constriction and SOD changing as well. Due to the sensitive nature of bead deposition, the slight change in arc shape and SOD significantly affect the bed geometry of each layer.
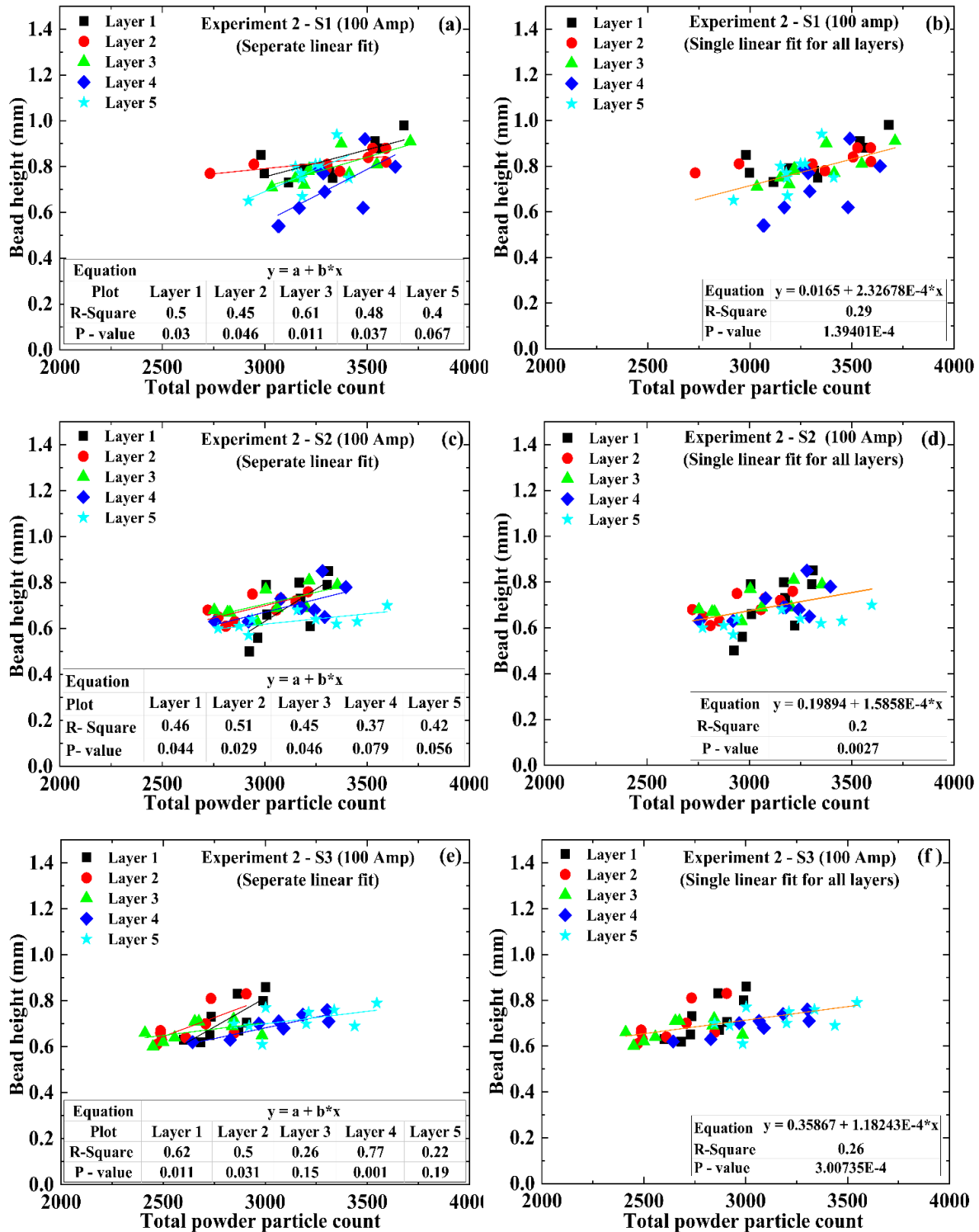
Figure 2-12 Bead height detection at every 53rd frame with respect to total powder particle count for respective 53 frames. Figures 2-12 (a), (c), and (e) show the separate linear fit between bead height and total powder particle count for the individual layers in three samples and Figures 2-12 (b), (d), and (f) show the concatenate linear fit between bead height and total powder particle count for all the layers together for same samples performed in experiment 2 (plasma current is 100 amp).
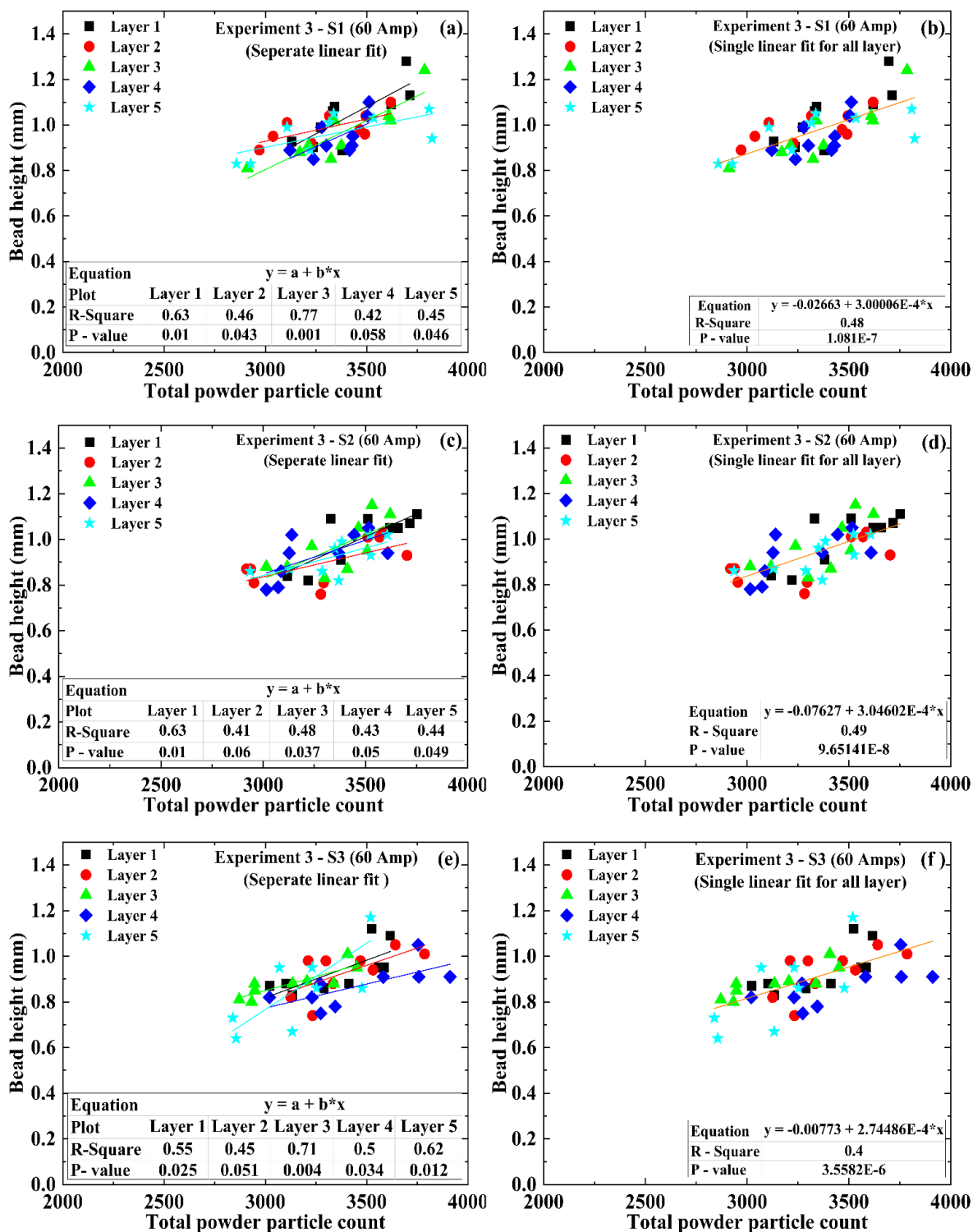
Figure 2-13 Bead height detection at every 53rd frame with respect to total powder particle count for respective 53 frames. Figure 2-13 (a), (c), and (e) shows the separate linear fit between bead height and total powder particle count for the individual layers in three samples and Figure 2-13 (b), (d), and (f) shows the concatenated linear fit between bead height and total powder particle count for all the layers together for same samples performed in experiment 3 (plasma current is 60 amp).

2.6.4 Comparison of regression of different samples using t-test

The linear regression model (straight line -1st order polynomial degree) explains a linear relationship where a dependent variable (y), i.e., bead height, is dependent on y-intercept (a) and of total powder particle count (independent variable x) that causes such a bead height variation throughout a coefficient factor, the slope (b), i.e., $y = b*x + a$, as shown in Table 2-3. The data from the 6 different samples were also analyzed to determine the regression line for individual samples (45 data points) performed at the plasma current of 100 amp and 60 amp. The concatenated linear fit was estimated across all the samples (135 data points); this result is categorized as the full sample.

The regression model for the three samples together is $y = 0.2*x + 190.5$ and $y = 0.3*x - 59.8$, respectively, for plasma currents of 100 amps and 60 amps, as shown in the last row of Table 2-3. The degree of variability of the PTA-AM process can be investigated by comparing the coincidence and parallelism of two regression lines of samples operated at the constant processing parameters. The slopes and y-intercept of two regression lines have been compared within samples operated at plasma current of 100 amp and 60 amp, respectively, as shown in Table 2-4. In addition, the regression model of samples operated between plasma current of 100 amp and 60 amp has been compared to investigate the effect of plasma current on the regression model, as shown in Table 2-5. Within this study, the two-tailed t-test is a statistical hypothesis test that has been used to test the significance of the difference in the slopes and y-intercepts of two regression lines. The null hypothesis of the t-test is that the slopes and the y-intercepts for two different samples are identical. With the confidence interval of 95%, the significance level (alpha) is 0.05, which compares with a p-value. If the p-value is greater than 0.05 of significance level, the null

hypothesis of the t-test has failed to reject, which estimates that the two slopes or intercepts are significantly identical.

Table 2-3 Fitted regressions for the samples (in µm) from Experiment 2 and 3

Plasma current	100 amp	60 amp	n
Sample 1 (S1)	$y = 0.23267x + 16.50$	$y = 0.30000x - 26.63$	45
Sample 2 (S2)	$y = 0.15858x + 198.94$	$y = 0.30460x - 76.27$	45
Sample 3 (S3)	$y = 0.11814x + 358.67$	$y = 0.27448x - 7.73$	45
Full Sample	$y = 0.2x + 190.5$	$y = 0.3x - 59.8$	135

As shown in Table 2-4, for all the possible samples' comparisons, the p-value is greater than 0.05, which depicts that the slopes are significantly equal. Similarly, the y-intercept of regression lines for two different samples is significantly identical except for the unusual observation in sample comparison of S3 and S1, which operates at the plasma current of 100 amp (p-value is $0.009 < 0.05$). As shown in Table 2-4, the analysis indicates that the linear relationship between the dependent variable (y), i.e., bead height and independent variable (x), i.e., total powder particle count is significantly similar for all three different samples operated at constant processing parameters. In other words, it can be concluded that the stable bead deposited in the PTA-AM process for constant operating parameters and the deposition process is less susceptible to external disturbances.

Table 2-4 Comparison of the linear regression slopes and y-intercepts using two-tailed t-test for different samples (S1, S2, S3) from Expt.2 and Expt. 3

	Experiment 2 (100 amp)			Experiment 3 (60 amp)		
Sample comparison	S1 & S2	S2 & S3	S3 & S1	S1 & S2	S2 & S3	S3 & S1
Comparison of slopes (p-value)	0.31	0.48	0.070	0.88	0.44	0.32
Comparison of y-intercepts (p-value)	0.137	0.181	0.009	0.960	0.945	0.984

Table 2-5 compares the regression statistics of every sample from experiment 2 with the samples from experiment 3. A total of 10 combinations of sample comparisons have been inspected to compare the variation in the slopes and intercepts. We have used 45 data points to analyze statistics from 1 to 9 while in order to compare slopes and intercepts across all the three samples, 135 data points were examined as shown in the last row of Table 2-5 and is referred to as "full sample." Inspection of Table 2-5 reveals that for the sample comparison, which is denoted as 4,5,7,8 and 9 in the table, the p-value for the comparison of slopes is less than the significance level (i.e., p-value < 0.05), which rejects the null hypothesis of two slopes being equal. The slopes are significantly different. Likewise, for the sample comparison, denoted as 5, 7, 8 and 9, the p-values are less than 0.05 level of significance. It shows that the y-intercepts are significantly different from each other by rejecting the null hypothesis of two intercepts being identical. The unusual data points have been recorded in sample S1 of experiment 2, which has regression statistics that are significantly equal to those of all samples from experiment 3. As we observed in the sample

comparisons named 1, 2, and 3 having p-value greater than 0.05 fails to reject the null hypothesis

of two slopes or intercepts being equal.

Table 2-5 Comparison of the linear regression slopes and y-intercepts using two-tailed t-test between the different samples (S1, S2, S3) from Expt. 2 and Expt. 3

Sr. No.	Samples comparison		Comparison of Slopes (p-value)	Comparison of y-intercepts (p-value)
	Experiment 2 (100 amp)	Experiment 3 (60 amp)		
1	S1	S1	0.355	0.93722
2	S1	S2	0.325	0.64332
3	S1	S3	0.580	0.85189
4	S2	S1	0.041	0.06044
5	S2	S2	0.035	0.02471
6	S2	S3	0.107	0.09662
7	S3	S1	0.001	0.00066
8	S3	S2	0.001	0.00019
9	S3	S3	0.010	0.00225
10	Full Sample	Full Sample	0.049	0.00458

On the contrary, the mean regression fits of full samples have been considered to compare the mean slopes and mean intercepts of all the data points together. Two-tailed t-tests revealed that the p-value was lower than the significance level, which is 0.05, a p-value of 0.049 and 0.00458 < 0.05. The mentioned results have shown that the slopes and intercepts of the full sample are significantly different from each other. In the PTA-AM process, the processing parameters are kept constant except the plasma current, which has been operated at 100 amp and 60 amp to investigate its effect on the bead deposition geometry. From Table 2-5, it can be concluded that the linear regression statistics (i.e., slopes and intercepts) between the bead height and total powder particle count is the function of plasma current. The bead deposition geometry is changed significantly with the effect of plasma current.

The effect of plasma current on the bead height and width is determined in the current study. The high-speed camera is oriented to capture only the bead height variation. The bead width dimension has been measured using a Vernier caliper. The five width measurements at a different position are taken to determine the mean bead width and its standard deviation. As shown in Figure 2-14, the x-axis defines the number of samples operated at 60 Amp and 100 Amp of plasma current. The y-axis represents the variation in mean bead height and width. From Figures 2-14 (a) and (b), it is investigated that the mean bead height decreased by 24 %, and the mean bead width increased by 84% as the plasma current increased by 40%. Furthermore, the mean deviation of the bead width has decreased by 71%, as the plasma current has reduced by 40%. It can be concluded that the width of the deposited layer stabilizes with fewer deviations as the plasma current reduces to a certain amount. However, the mean deviation in height is nearly constant, which provides a clear indication that there is a negligible effect of plasma current on bead height stabilization.
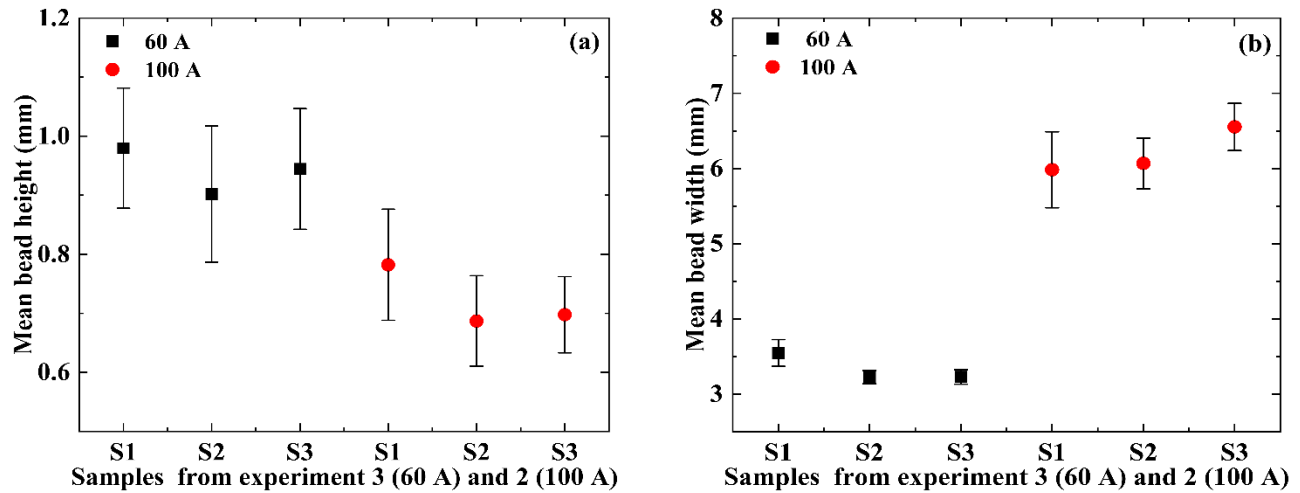
Figure 2-14 Effect of plasma arc current on the (a) Mean bead height and (b) Mean bead width for three different samples (S1, S2, and S3)

This is due to the increase in the arc current, that the amount of transfer of heat energy increases, leading to the complete fusion of powder material into the molten pool and substrate surface zone. It also impacts the fluid properties of the deposited bead at the melt pool zone, which gives rise in temperature of the melt pool and reduction in viscosity of the molten deposition material. As the viscosity of material decreases, the percent dilution of deposition increases, which can be the possible reason for the lateral spreading of the bead deposition over the substrate surface. In addition, the complete melting of the powder material as the arc current increases advances the broadness of width of bead deposition. However, it is observed that bead height is less as compared to the width of the bead [33].

2.7 Conclusion

This study provides the methodology through the image processing techniques to optimize the process parameters, to determine statistical powder distribution and to compute the bead geometry of multi-layer single-pass deposition of WC-reinforced NiCrBSi composites by using the PTA-

AM process considering plasma current, table travel speed, powder feed rate and SOD as processing parameters. It comprises the image processing approach to correlate optimized SOD with Gaussian powder distribution. The proposed technique is also applied to the image stream captured using high speed imaging for the bead height detection. The linear regression model is developed to determine the relationship between bead height and measured powder particles. The significance of the relationship is determined using the ANOVA test and two-tailed t-test. The influence of plasma current on bead geometry is also investigated.

The following are the main conclusions that can be drawn from the research work:

- The results for experiment 1 have shown that the Gaussian distribution of two powder streams merges into one at the SOD plane of 7 mm, leading to depositing the stable bead. At the SOD plane of 9.44 mm, the Gaussian distribution of powder streams presents a "saddle shape," which can be the reason for an unstable bead. The predicted SOD from image processing is in good agreement with experimentally calculated SOD from the work of Rojas. et.al.[56]. At the optimized SOD of 7 mm, the projected deposition zone is almost equal to the plasma arc region, which implies that the plasma arc totally melts the powder stream fed into the deposition zone. As a result, higher powder utilization efficiency and bead geometrical accuracy can be attained with in-focused powder flow.

- Image analysis proves that the powder stream distribution is uniform for the samples performed at a constant powder feed rate. It signifies that the PTA-AM system is less susceptible to disturbances.

- The influence of powder particle measurement on the bead height variation was determined using a linear regression model. The ANOVA result concludes that the linear relationship between the variation in the deposited bead height and the powder particle count is significant. The two-tailed t-test has deduced that the linear relationship is approximately constant for all the 3 different samples performed in Expt.2 and Expt.3, respectively. It implies that the deposition process is consistent with less degree of variation for constant processing parameters used in different samples. In addition, the same statistical technique has concluded that the linear relationship between bead height and total powder particle count is significantly changed under the effect of plasma arc current.

- The influence of plasma arc current on the bead geometry is proven to be very significant during the deposition process. As the plasma current is increased by 40%, the mean bead width increases by 85%. Although, the mean bead height decreases by 24%. It is also observed that bead width is stable with lesser deviation as plasma current is decreased to 60 Amp from 100 Amp.

References

[1]   Mazumder, J. (2015). Design for metallic additive manufacturing machine with capability for "certify as you build." Procedia CIRP, 36(Dmd), 187–192, https://doi.org/10.1016/j.procir.2015.01.009.

[2]   Thompson, S. M., Bian, L., Shamsaei, N., & Yadollahi, A. (2015). An overview of Direct Laser Deposition for additive manufacturing; Part I: Transport phenomena, modelling and diagnostics. Additive Manufacturing, 8, 36–62. https://doi.org/10.1016/j.addma.2015.07.002.

[3]   Ding, D., Pan, Z., Cuiuri, D., & Li, H. (2015). Wire-feed additive manufacturing of metal components: technologies, developments and future interests. International Journal of Advanced Manufacturing Technology, 81(1–4), 465–481. https://doi.org/10.1007/s00170-015-7077-3.

[4]   Andersson, J. (2020). Welding metallurgy and weldability of superalloys. Metals, 10(1)., https://doi.org/10.3390/met10010143.

[5]   Cunningham, R., Nicolas, A., Madsen, J., Fodran, E., Anagnostou, E., Sangid, M. D., & Rollett, A. D. (2017). Analyzing the effects of powder and post-processing on porosity and properties of electron beam melted Ti-6Al-4V. Materials Research Letters, 5(7), 516–525. https://doi.org/10.1080/21663831.2017.1340911.

[6]   Wu, B., Pan, Z., Ding, D., Cuiuri, D., Li, H., Xu, J., & Norrish, J. (2018). A review of the wire arc additive manufacturing of metals : properties, defects and quality improvement. Journal of Manufacturing Processes, 35(August), 127–139.https://doi.org/10.1016/j.jmapro.2018.08.001.

[7]   Dass, A., & Moridi, A. (2019). State of the Art in Directed Energy Deposition : From Additive Manufacturing to Materials Design, Coatings, 9(July), p.418. 1–26. https://doi.org/10.3390/coatings9070418

[8]   Tan, H., Zhang, F., Fu, X., Meng, J., Hu, G., Fan, W., & Huang, W. (2016). Development of powder flow model of laser solid forming by analysis method. International Journal of Advanced Manufacturing Technology, 82(5–8), 1421–1431. https://doi.org/10.1007/s00170-015-7481-8

[9]   Gong, X., Wang, J., & Feng, H. (2019). Lateral powder transport model with Gaussian distribution in laser cladding. International Journal of Advanced Manufacturing Technology, 102(9–12), 3747–3756.https://doi.org/10.1007/s00170-019-03499-3.

[10]   Mahmood, M. A., Popescu, A. C., Oane, M., Ristoscu, C., Chioibasu, D., Mihai, S., & Mihailescu, I. N. (2020). Three-jet powder flow and laser–powder interaction in laser melting deposition: Modelling versus experimental correlations. Metals, 10(9), 1–17. 2020, https://doi.org/10.3390/met10091113.

[11]   Parekh, R., Buddu, R. K., & Patel, R. I. (2016). Multiphysics Simulation of Laser Cladding Process to Study the Effect of Process Parameters on Clad Geometry. Procedia Technology, 23, 529–536. https://doi.org/10.1016/j.protcy.2016.03.059.

[12]   Ferreira, E., Dal, M., Colin, C., Marion, G., Gorny, C., Courapied, D., & Peyre, P. (2020). Experimental and numerical analysis of gas/powder flow for different LMD nozzles. *Metals*, *10*(5), 667.. https://doi.org/10.3390/met10050667.

[13]   Saqib, S., Urbanic, R. J., & Aggarwal, K. (2014). Analysis of laser cladding bead morphology for developing additive manufacturing travel paths Design of Experiments. Procedia CIRP, 17, 824–829. https://doi.org/10.1016/j.procir.2014.01.098.

[14]   Caiazzo, F., & Caggiano, A. (2018). Laser direct metal deposition of 2024 al alloy: Trace geometry prediction via machine learning. Materials, 11(3). https://doi.org/10.3390/ma11030444.

[15]   Tang, Z. jue, Liu, W. wei, Wang, Y. wen, Saleheen, K. M., Liu, Z. chao, Peng, S. tong, Zhang, H. chao. (2020). A review on in situ monitoring technology for directed energy deposition of metals. International Journal of Advanced Manufacturing Technology, 108(11–12), 3437–3463. https://doi.org/10.1007/s00170-020-05569-3.

[16]   Galati, M., & Iuliano, L. (2018). A literature review of powder-based electron beam melting focusing on numerical simulations. Additive Manufacturing, 19, 1–20.https://doi.org/10.1016/j.addma.2017.11.001.

[17]   Soylemez, E., Beuth, J. L., & Taminger, K. (2010). Controlling melt pool dimensions over a wide range of material deposition rates in electron beam additive manufacturing. 21st Annual International Solid Freeform Fabrication Symposium - An Additive Manufacturing Conference, SFF 2010, (January 2010), 571–582.

[18]   Kuchi, S. C. (2009). Effect of finite geometry on solidification microstructure in the beam-based fabrication of thin-wall structures (Doctoral dissertation, Wright State University).

[19]   Wallace, T. A., Bey, K. S., Taminger, K. M., & Hafley, R. A. (2004). A design of experiments approach defining the relationships between processing and microstructure for Ti-6Al-4V. In 2004 International Solid Freeform Fabrication Symposium.

[20]   Gockel, J., Beuth, J., & Taminger, K. (2014). Integrated control of solidification microstructure and melt pool dimensions in electron beam wire-feed additive manufacturing of Ti-6Al-4V Additive Manufacturing, 1–4, 119–126. https://doi.org/10.1016/j.addma.2014.09.004.

[21]   Yao, M., Yao, Z., Tao, X., & Moliar, O. (2020). Effect of deposition modes on electron beam directed energy deposited inconel 718. Materials Science and Technology, 36(14), 1556-1565.

[22]   Seufzer, W. J., & Taminger, K. M. (2007). Control methods for the electron beam free form fabrication process. In 2007 International Solid Freeform Fabrication Symposium.

[23]   Li, F., Chen, S., Shi, J., Zhao, Y., & Tian, H. (2018). Thermoelectric cooling-aided bead geometry regulation in wire and arc-based additive manufacturing of thin-walled structures. Applied Sciences, 8(2), 207. https://doi.org/10.3390/app8020207.

[24]   Dinovitzer, M., Chen, X., Laliberte, J., Huang, X., & Frei, H. (2019). Effect of wire and arc additive manufacturing (WAAM) process parameters on bead geometry and microstructure.

Additive Manufacturing, 26(October 2018), 138–146. https://doi.org/ 10.1016/j.addma.2018.12.013

[25]   Wang, H., Jiang, W., Ouyang, J., & Kovacevic, R. (2004). Rapid prototyping of 4043 Al-alloy parts by VP-GTAW. Journal of Materials Processing Technology, 148(1), 93–102. https://doi.org/ 10.1016/j.jmatprotec.2004.01.058.

[26]   Rodrigues, T. A., Duarte, V., Miranda, R. M., Santos, T. G., & Oliveira, J. P. (2019). Current status and perspectives on wire and arc additive manufacturing (WAAM). Materials, 12(7). https://doi.org/10.3390/ma12071121.

[27]   Karmuhilan, M., & Kumar, A. (2018). ScienceDirect Intelligent process model for bead geometry prediction in WAAM. Materials Today: Proceedings, 5(11), 24005–24013. https://doi.org/10.1016/j.matpr.2018.10.193.

[28]   Ding, D., Pan, Z., Cuiuri, D., Li, H., Duin, S. Van, & Larkin, N. (2016). Robotics and Computer-Integrated Manufacturing Bead modelling and implementation of adaptive MAT path in wire and arc additive manufacturing. Robotics and Computer Integrated Manufacturing, 39, 32–42. https://doi.org/ 10.1016/j.rcim.2015.12.004.

[29]   Alberti, E. A., Bueno, B. M. P., & D'Oliveira, A. S. C. M. (2016). Additive manufacturing using plasma transferred arc. The International Journal of Advanced Manufacturing Technology, 83(9-12), 1861-1871.

[30]   Vály, L., Grech, D., Neubauer, E., Kitzmantel, M., Bača, Ľ., & Stelzer, N. (2017). Preparation of Titanium Metal Matrix Composites Using Additive Manufacturing. 742, 129–136.https://doi.org/10.4028/www.scientific.net/KEM.742.129.

[31]   Perez-Soriano, E. M., Ariza, E., Arevalo, C., Montealegre-Melendez, I., Kitzmantel, M., & Neubauer, E. (2020). Processing by additive manufacturing based on plasma transferred arc of Hastelloy in air and argon atmosphere. Metals, 10(2). https://doi.org/ 10.3390/met10020200.

[32] Rodriguez, J., Hoefer, K., Haelsig, A., & Mayr, P. (2019). Functionally graded SS 316L to Ni-based structures produced by 3D plasma metal deposition. Metals, 9(6), 620. https://doi.org/10.3390/met9060620

[33]   Lakshminarayanan, A. K., Balasubramanian, V., Varahamoorthy, R., & Babu, S. (2008). Predicting the dilution of plasma transferred arc hardfacing of stellite on carbon steel using response surface methodology. Metals and Materials International, 14(6), 779–789.https://doi.org/ 10.3365/met.mat.2008.12.779.

[34]   Wang, C., Suder, W., Ding, J., & Williams, S. (2021). The e ff ect of wire size on high deposition rate wire and plasma arc additive manufacture of Ti-6Al-4V. Journal of Materials Processing Tech., 288(April 2020), 116842. https://doi.org/ 10.1016/j.jmatprotec.2020.116842.

[35]   Mercado Rojas, J. G., Wolfe, T., Fleck, B. A., & Qureshi, A. J. (2018). Plasma transferred arc additive manufacturing of Nickel-metal matrix composites. Manufacturing Letters, 18, 31–34.https://doi.org/ 10.1016/j.mfglet.2018.10.001.

[36]   Rojas, J. G. M., Ghasri-Khouzani, M., Wolfe, T., Fleck, B., Henein, H., & Qureshi, A. J. (2021). Preliminary geometrical and microstructural characterization of WC-reinforced NiCrBSi matrix composites fabricated by plasma transferred arc additive manufacturing through Taguchi-based experimentation. The International Journal of Advanced Manufacturing Technology, 113(5), 1451-1468. https://doi.org/ 10.1007/s00170-020-06388-2.

[37]   El Moghazi, S. N., Wolfe, T., Ivey, D. G., & Henein, H. (2020). Plasma transfer arc additive manufacturing of 17-4 PH: assessment of defects. The international journal of advanced manufacturing technology, 108, 2301-2313. https://doi.org/10.1007/s00170-020-05540-2

[38]   Nikam, S. H., & Jain, N. K. (2018). 3D-finite element simulation and image processing based prediction of width and height of single-layer deposition by micro-plasma-transferred arc process. The International Journal of Advanced Manufacturing Technology, 95(9), 3679-3691. https://doi.org/ 10.1007/s00170-017-1472-x.

[39]   Nikam, S. H., Jain, N. K., & Jhavar, S. (2016). Thermal modelling of the geometry of single-track deposition in micro-plasma transferred arc deposition process. Journal of Materials Processing Technology, 230, 121-130.https://doi.org/10.1016/j.jmatprotec.2015.11.022.

[40]   Jhavar, S., Jain, N. K., & Paul, C. P. (2014). Development of micro-plasma transferred arc (μ-PTA) wire deposition process for additive layer manufacturing applications. Journal of Materials Processing Technology, 214(5), 1102-1110.https://doi.org/10.1016/j.jmatprotec.2013.12.016.

[41]   Sawant, M. S., & Jain, N. K. (2018). Investigations on additive manufacturing of Ti–6Al–4V by microplasma transferred arc powder deposition process. Journal of Manufacturing Science and Engineering, 140(8), 081014. https://doi.org/10.1115/1.4040324.

[42]   Liyanage, T., Fisher, G., & Gerlich, A. P. (2012). Microstructures and abrasive wear performance of PTAW deposited Ni–WC overlays using different Ni-alloy chemistries. Wear, 274, 345-354.https://doi.org/10.1016/j.wear.2011.10.001.

[43]   Vetter, P. A., Engel, T., & Fontaine, J. (1994, September). Laser cladding: the relevant parameters for process control. In Laser Materials Processing: Industrial and Microelectronics Applications (Vol. 2207, pp. 452-462). International Society for Optics and Photonics.https://doi.org/10.1117/12.184751.

[44]   Toyserkani, E., Khajepour, A., & Corbin, S.F. (2004). Laser Cladding (1st ed.). CRC Press. https://doi.org/10.1201/9781420039177

[45]   Liu, W. W., Tang, Z. J., Liu, X. Y., Wang, H. J., & Zhang, H. C. (2017). A review on in-situ monitoring and adaptive control technology for laser cladding remanufacturing. Procedia Cirp, 61, 235-240. https://doi.org/10.1016/j.procir.2016.11.217.

[46]   Liu, W. W., Tang, Z. J., Liu, X. Y., Wang, H. J., & Zhang, H. C. (2017). A review on in-situ monitoring and adaptive control technology for laser cladding remanufacturing. Procedia Corp, 61, 235-240. https://doi.org/10.1146/annurev-matsci-070115-032024.

[47]   Łatka, L., & Biskup, P. (2020). Development in PTA surface modifications–a review. Advances in Materials Science, 20(2), 39-53. https://doi.org/10.2478/adms-2020-0009.

[48]   Mendez, P. F., Barnes, N., Bell, K., Borle, S. D., Gajapathi, S. S., Guest, S. D., ... & Wood, G. (2014). Welding processes for wear-resistant overlays. Journal of Manufacturing Processes, 16(1), 4-25. https://doi.org/10.1016/j.jmapro.2013.06.011.

[49]   Wolff, S. J., Wu, H., Parab, N., Zhao, C., Ehmann, K. F., Sun, T., & Cao, J. (2019). In-situ high-speed X-ray imaging of piezo-driven directed energy deposition additive manufacturing. Scientific reports, 9(1), 1-14.https://doi.org/10.1038/s41598-018-36678-5.

[50]   Wolff, S. J., Webster, S., Parab, N. D., Aronson, B., Gould, B., Greco, A., & Sun, T. (2021). In-situ observations of directed energy deposition additive manufacturing using high-speed x-ray imaging. JOM, 73(1), 189-200. https://doi.org/ 10.1007/s11837-020-04469-x.

[51]   Lott, P., Schleifenbaum, H., Meiners, W., Wissenbach, K., Hinke, C., & Bültmann, J. (2011). Design of an optical system for the in situ process monitoring of selective laser melting (SLM). Physics Procedia, 12, 683-690.https://doi.org/10.1016/j.phpro.2011.03.085.

[52]   Fathi, A., Khajepour, A., Toyserkani, E., & Durali, M. (2007). Clad height control in laser solid freeform fabrication using a feedforward PID controller. The International Journal of Advanced Manufacturing Technology, 35(3-4), 280-292. https://doi.org/10.1007/s00170-006-0721-1.

[53]   Mozaffari, A., Fathi, A., Khajepour, A., & Toyserkani, E. (2013). Optimal design of laser solid freeform fabrication system and real-time prediction of melt pool geometry using intelligent evolutionary algorithms. Applied Soft Computing, 13(3), 1505-1519. https://doi.org/ 10.1016/j.asoc.2012.05.031.

[54]   Metco O (2019) Material product data sheet monocrystalline tungsten carbide/nickel chromium boron silicon powder for plasma transferred arc (PTA). Oerlikon Metco.

[55]   Frenk, A., Vandyoussefi, M., Wagniere, J. D., Kurz, W., & Zryd, A. (1997). Analysis of the laser-cladding process for stellite on steel. Metallurgical and Materials transactions B, 28(3), 501-508. https://doi.org/10.1007/s11663-997-0117-0.

[56]   Jose Guadalupe Mercado Rojas (2021), Design and system identification for a plasma transferred arc additive manufacturing technology, University of Alberta. Unpublished research

3 Maximum spreading of molten powder particles in PTA-AM process[2]

3.1 Abstract

In plasma transferred arc additive manufacturing (PTA-AM), the powder flow behaviour (the particle trajectories and their velocities) under the plasma arc is a complex but essential physical phenomenon, which affects not only the geometrical dimensions but also the characteristics of the bead deposition. Understanding the Tungsten Carbide reinforced NiCrBSi powder particle transportation during the interaction with plasma arc is limited and requires in-depth investigation. This study employs high-speed imaging in the PTA-AM process to capture the 2D powder flow images and import them into the image analysis software to assess variation in powder particle trajectories and velocities under the influence of plasma arc currents. The results showed a substantial shift in powder particle deposition zones on the substrate plane and traced the fluctuation in particle velocity with increasing plasma current by 40%. It has also been observed that the particle initial space condition at the nozzle outlet with respect to the plasma arc region decides the particle path and particle speed before impact on the substrate. The theoretical trajectory model validates the midstream particle flow characteristics derived from image analysis. Based on these results, the parametric study is further conducted to predict the spreading and solidification dynamics of the individual molten powder particles during their impingement on the

---

deposition plane. It was found that the particle's impact velocity plays a vital role in the particle's impact dynamics.

Nomenclature

A_p	particle area	V_i	impact velocity
C_d	coefficient of drag	V_p	particle volume
C_p	specific heat	V_{radial}	radial velocity
D_p	particle diameter	$V_\infty(r)$	plasma arc velocity
D'	cylindrical disk diameter of spread particle	w	z-component of velocity
D_{max}	maximum spread diameter	W_{1-2}	energy loss due to viscous dissipation
D_t	base diameter of a truncated particle		
F	forces acting on a particle	*Greek symbols*	
$\vec{g}$	acceleration due to gravity		
h	solid layer thickness	α	solidification term $We\sqrt{\dfrac{3\,Ste}{4\,Pe}}$
h^*	dimensionless solid layer thickness	σ_{LV}	surface tension
h_f	latent heat of fusion	ρ	density
I	plasma arc current	ξ_{max}	maximum spreading factor
KE_1	kinetic energy before impact	μ	viscosity
KE_2	kinetic energy after impact	θ_e	equilibrium contact angle
ΔKE	kinetic energy loss due to solidification	φ	viscous dissipation
r	distance between arc axis and calculated point	ω	argon plasma's magnetic permeability
r_*	radius of plasma arc column		
SE_1	surface energy before impact	*Dimensionless number*	
SE_2	surface energy after impact		
t	time	Pe	Peclet number
t^*	dimensionless time	Re	Reynolds number
t_c	characteristic time for dissipation	Ste	Stefan number
T_p	particle temperature	We	Weber number
T_s	substrate temperature		
u	x-component of velocity	*Subscripts*	
U_c	characteristic velocity		
$\vec{U}_r$	resultant velocity	p	particle
		s	substrate
		∞	plasma

3.2 Introduction

An additive manufacturing (AM) is a rapidly growing field, where a process of layer-by-layer deposition attends the production of complex 3D shapes guided by a CAD model [1]. AM is highly valued in numerous industries due to its versatility, design flexibility, and ability to produce metallic products with various materials that can withstand harsh conditions such as abrasion and erosion [2]–[4]. Additionally, AM can lead to novel products that could not be fabricated by conventional subtractive processes and allow for a longer lifecycle for existing products through innovative repair methods [4]. Directed energy deposition (DED) is a category of an AM process predominantly used for deposition of high-performance material, such as nickel-based, titanium-based alloys, composites and functionally graded materials, etc.[5]. DED uses a concentrated energy source (laser, electron beam, or plasma/electric arc) that is focused on the substrate, forming a small molten pool and simultaneously melting the feedstock material (either powder or wire) and depositing into the molten pool to build the product [5].

DED-AM is a non-equilibrium process with rapid cooling rates. This process involves a variety of process parameters (such as heat source, powder feed rate, carrier and shielding gas flow, stan-off distance, and table travel speed), which are combined with multiple physical processes that determine deposition rate and quality, powder utilization, and bead geometry characteristics [6], [7]. These processing variables need to be optimized, and complex physical phenomena such as the interaction between heat source, powder flow, and melt pool need to be understood to manufacture the part free from defects [8]. The powder flow behaviour in the DED process is a crucial factor. It introduces complexity in the process and controls the deposition quality. Different interaction positions of the powder stream with molten pool [9], including powder flow

convergence effects on heat sources (such as lasers) [10] and powder distribution effects on the molten pool [11], significantly affect liquid pool morphology and, later in the solidification behaviour of the deposited material [12]. The powder flow behaviour, which includes particle velocity and trajectory, and powder stream distribution, has an important influence on the interaction of concentrated energy source, powder stream, and molten pool, which determines the particles catching ability in the melt pool (powder catching efficiency) and results in the geometric dimensions of the deposition system [13].

The increment in the velocity of the particles can decrease the powder catching efficiency, which results in the poor surface finish of the deposited layer. Also, too low particle velocity affects catching efficiency and surface quality since impinging particles must possess some momentum to break the surface tension of the molten pool [14]. The other factor determining the powder catching efficiency in the melt pool region is the flow information of individual particles' trajectories. Analyzing trajectory information on powder particles makes it possible to calculate the number of powder particles that will bounce off the previously deposited layer/substrate and fall into the melt pool under the heat source region. Furthermore, the variation in particle velocity within the heat source often affects the resident time (time for the particles to travel from nozzle exits to the molten pool) of powder particles. The resident time governs the powder's thermal states, such as the degree of heating and melting of powder particles when they reach the substrate [15]. As a result, the different thermal phenomena (fully melted, partially melted or entirely solid) of the powder particles can significantly affect the deposition quality and microstructural and mechanical properties [16], [17] of the resulting material. The flow information of the particles (velocity and trajectory) is also essential to ensure the sufficient bonding of the deposits over the

substrate. The melt pool's dilution rate and the melt pool's fusion state at the centre and edges are based on the powder stream's flow information [18]. Thus, optimum particle velocity becomes a matter of great importance for given processing parameters and requires immediate attention. As a result, researchers have dedicated their attention to the flow behaviour of powder particles, such as particle trajectories and velocities and their variation under the heat source. In the following paragraph, a review of past work in this direction is presented.

Researchers Schopphoven et al. [19] have experimentally characterized the powder-gas jet of Laser-DED and validated it with the numerical model. In their study, the quantification and position of the powder particles at different SOD were analyzed. Using the high-speed images of powder streams, they have confirmed the rectilinear motion and constant velocity of powder trajectories until they reach the substrate. In the same study, the laser beam-powder jet interaction and particle-substrate heat transfer phenomena were also investigated. Based on the simulated model, Liu et al.[20] investigated powder flow under the influence of nozzle exit geometry, powder morphology (particle size, shape, and density), and powder flow parameters (feed rate and carrier-gas flow rate). In order to capture the particle velocity and particle distribution characteristics of the powder flow, a high-speed CCD camera was used. It was found that the surface quality of the clad can be improved through the adjustment of carrier gas flow rate, which will ensure homogeneous powder distribution. Also, a decrease in particle velocity is observed with the increase in density, and the speed of non-spherical particles is high. The particle velocity was also increased with the carrier gas flow rate but not with the powder feed rate. The influence of particle diameter and restitution coefficient on the dynamics of powder streams has also been studied by Hao et al.[21]. In addition to the dynamics behaviour, the thermal behaviour of the powder stream

is also modelled numerically in [22]. The deposition zone is predicted for a combination of laser and powder parameters. In addition, a study by Silva et al.[23] demonstrated with HSI that, as powder particles heated up in the laser beam, they reached their vaporization temperature and the associated recoil pressure altered their trajectory path. Likewise, the [24], [25] study has demonstrated that in the laser radiation field, powder particles experience intense acceleration due to laser evaporation and the force generated by recoil pressure generated by the vaporization of the particles. In the Laser-based DED system, the TiC powder flow-laser radiation interaction is studied by Gulyaev et al. [26] using the optical diagnostic system. A study has revealed that powder particles accelerate under the laser beam and that their trajectory is also substantially altered by laser radiation. The study [27]–[29] employed an *in-situ* high-speed X-ray imaging system to observe the interactions between powder flows and the laser and how the laser energy is absorbed into the substrate and molten pool, which ultimately influences the parameters of the clad layer. The microstructure properties of the molten pool geometry depend on the powder flow characteristics. It has been shown in the experimental and modelling study of Anandkumar et al. [17] that the particle injection velocity is the key factor for the variation in the microstructure of Al–12Si/SiC coatings prepared by the L-DED process. The particle injection velocity determines the interaction time between the laser beam and powder stream. As a result, the time it takes for particles to melt is different based on particle injection velocity. According to the same study, particle temperature increases with increments in trajectory and beam intensity. The L-DED process is based on the principle that a laser beam is incident on a substrate surface and forms a melt pool as a result. The powder is fed through a powder feeder and nozzle onto the melting pool as an additive material.

Unlike the L-DED process, the plasma arc-based DED process works by injecting powder into the plasma arc region, where it melts. As the molten powder particles impinge on the substrate, the individual particles spread, agglomerate with each other, and form a molten pool. As a result, a layer-by-layer 3D object is constructed. The final part's quality depends on various parameters such as powder material properties, impact conditions (particle trajectory and velocity) and substrate conditions (substrate material, temperature and thermal contact resistance between particles and substrate). A particle's impact dynamics are determined by the rate at which it melts under the plasma arc and spreads on the substrate, where it solidifies. When powder particles travel along their trajectory and velocity, it determines the time in which particles remain underneath the plasma arc zone, which results in the state of the particle impacting the substrate, which may be semi-melted or completely melted. The state of the particles at the point of impact is a deciding factor for the printed component's geometrical, microstructural, and mechanical properties. In addition to these properties, the bonding strength of the molten particles with the substrate or previously deposited layer is highly dependent on the particle's spreading and solidification dynamics during its impingement. It is essential to control the molten particle's cooling rate during solidification since it determines the final microstructure and material properties. Furthermore, achieving good flow characteristics of deposited molten particles will minimize the presence of voids, enabling dense and homogeneous artifacts. It is, therefore, crucial to control the solidification of the particles. It depends on the particles' residence time in the plasma arc region, which is the particle's trajectory and velocity function. Therefore, a deep understanding of powder flow behaviour under the plasma arc region is essential. Several research studies [30]–[32] in thermal spraying have been assessed to calculate the particles' velocities and their effect on the impact dynamics of the molten particles during impingement on the surface. The same modelling

methodology can be applied to plasma arc-based DED to estimate the variation in velocities and trajectories of particles and their spreading phenomena upon impact on the substrate under the effect of the plasma arc. The difference in the physics between thermal spraying and the plasma arc-based DED system is the particles' travelling distance and their delivery position into plasma, and the temperature and velocity of the centre gas flow with the plasma. The studies [30]–[32] in plasma spraying have mainly investigated the powder flow behaviour, such as impact velocity and trajectories that govern the dynamics of the individual melted particles and the solidification behaviour after they impinge on the substrate. The impact dynamics include the spreading, splashing, and rebounding of the melted powder particles responsible for the uniform and quality deposition. The surface roughness, geometry deviation, microstructure properties are also the function of impact dynamics of the powder particles. In addition, Xibao et al. [33] in the PTA surfacing have investigated plasma fluid velocity as the function of plasma arc current. It is determined in the study that as the powder stream enters the plasma region, the powder particles accelerate, which might change the particle's thermal behaviour in the plasma arc region.

Based on the literature review, it can be concluded that the powder flow behaviour with laser-based DED systems and pertinent particles' impact dynamics is studied in greater detail. To our knowledge, no peer-reviewed studies have been conducted to analyze powder particles trajectories and velocities during their transportation from the nozzle exit to the substrate and their effect (particles impact velocity) on the spreading phenomena in a plasma arc-based DED process. Hence, the present work is dedicated to plasma arc-based DED processes known as the plasma transferred arc additive manufacturing process (PTA-AM), which is aimed to (i) investigate the interaction of the plasma arc current with powder flow by studying the variation in key flow

behaviours of the powder particles such as particles trajectories and velocities under the influence of plasma arc current, and (ii) to study the parametric effect of impact velocities of the powder particles on its spreading and solidification during their impingement on the substrate.

In this study, the single-particle theoretical trajectory model is also developed to validate the experimental results. The model developed by Pasandideh-Fard [30] has been implemented with necessary modifications for the parametric study of the spreading and solidification of molten particles. A high-speed imaging method is proposed to capture the dynamics of powder stream transporting from nozzle exit to the substrate under plasma arc current. The image processing approach is used to track the particles' trajectories and calculate their velocities. PTA is among the existing DED-AM techniques used for depositing high wear-resistant [34] and corrosion-resistant coatings [35] at faster deposition speeds [36]. The PTA is also employed for hardfacing applications in the industries such as marine, oil drilling, steel manufacturing, etc. [37]. In the recent work of Mercado Rojas et al. [38], it has been proved that the PTA-AM system can build Tungsten Carbide-based Metal Matrix Composites (MMC) parts appropriate for the mining, oil, and gas sectors.

3.3 Experimental and optical setup

Figure 3-1 depicts the schematic as well as the process principle of the PTA-AM system. As it could be observed, the feedstock material (metal powder) is carried into the concentrated plasma arc through a carrier gas, and the plasma arc provides the necessary energy to melt it. The shielding gas prevents the melting powder particles and the molten pool from oxidation, resulting in metallurgically pure deposits and high-quality products [39].
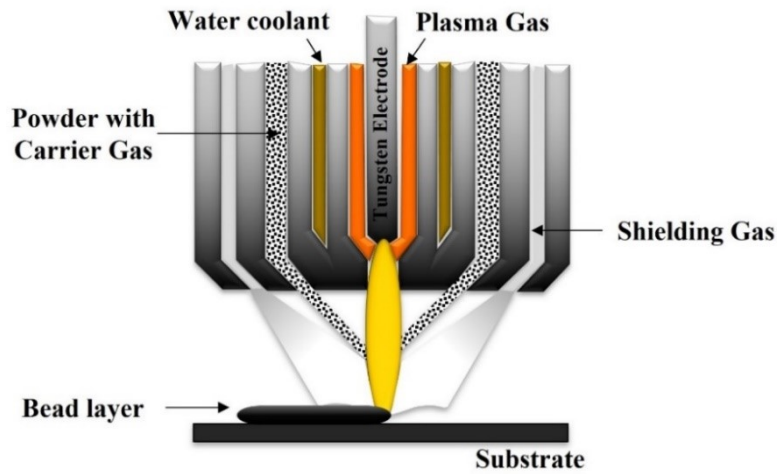
Figure 3-1 Plasma transferred arc deposition system
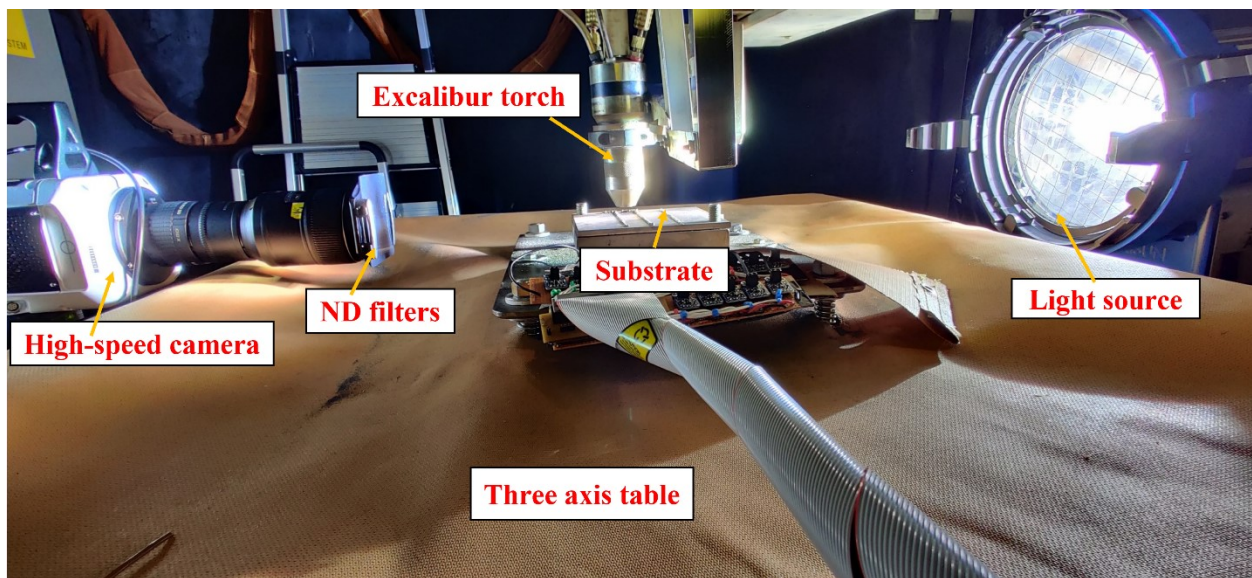
Figure 3-2 Experimental setup of PTA-AM system

The primary equipment used in the DED process is an in-house PTA-AM system containing a Kennametal Starweld 400A PTA (Pittsburgh, USA) source, mounted with Kennametal Stellite Excalibur Torch [2]. The torch includes a high-performance nozzle (3.18 mm diameter) with two powder ports and a thoriated tungsten electrode that is sharpened to an angle of 20°. At the Excalibur torch, an arc of plasma melts the powder particles transported from the hopper to the

nozzle inlets by argon gas. In this process, the backlight illumination was provided by a 1.2-kW HMI PAR Arrisun 12 plus (New York, USA).

The torch is preset at one position, and the worktable moves in 3D, directed by a CAD model. In the PTA-AM system, the powder streams injected from nozzle exits are recorded with a high-speed camera (Phantom v711, Vision Research) equipped with an extended macro lens (AF-S Micro NIKKOR 105 mm f/2.8). This CMOS high-speed camera can record up to 68,000 frames per second. A sensor size of 1280 × 800 pixels is used, in which each pixel measures 20 µm × 20 µm. The camera lens is fitted with a neutral density (ND) filter to suppress the plasma arc intensity and the melt pool brightness. A carefully chosen spatial resolution, exposure time and frame rate were used in this study in order to record the powder flow streams under the plasma arc without losing the relevant information and to capture image streams that are computationally practicable for implementing the image analysis algorithm. In this regard, the sampling frequency of 7500 frames per second, with a 4µs exposure time, is decided, corresponding to an image resolution of 1024 × 767 pixels.

Figure 3-3 (a) shows the optical setup used in the experimental PTA-AM system. High-speed images were taken with a camera mounted on a tripod (Manfrotto, Italy) to examine powder streams. A backlight source is used to irradiate the powder particles. An ND-4 filter is placed in front of the macro lens to reduce the amount of plasma arc light entering it by 1/10,000. The camera's field of view has been positioned to a precise observation height by aligning the camera sensor perfectly with the substrate. Figure 3-3 (b) depicts that the camera is pointed at and aligns with the backlight illumination source. These are perpendicular to the powder port plane and the

travelling direction of the worktable. The depth of field is correctly adjusted to provide an in-focused image of powder streams in a plane perpendicular to the camera position.

(a)

(b)
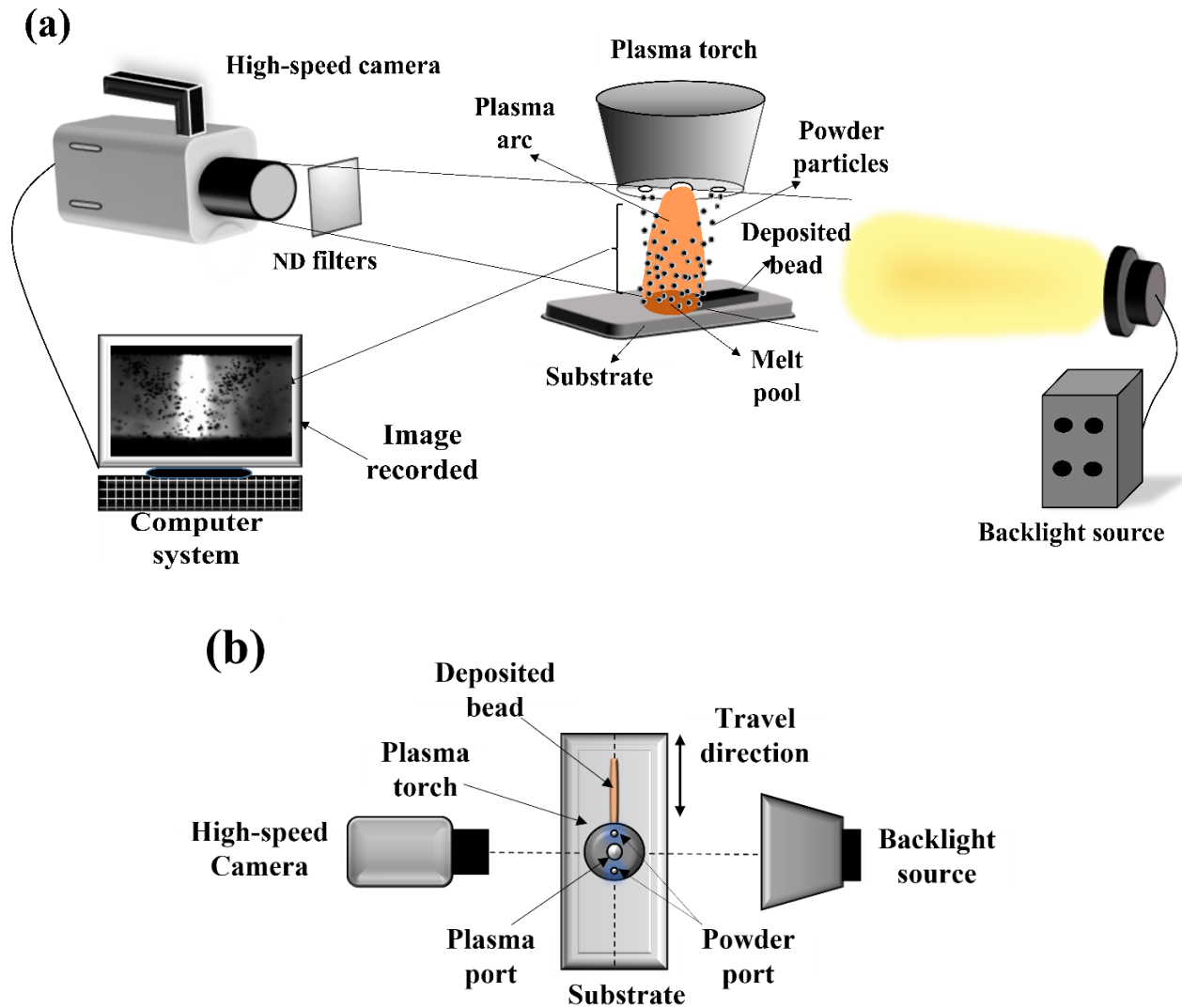
Figure 3-3 Schematic of optical setup in PTA-AM system (a) Isometric view (b) Top view

Table 3-1 Chemical composition ranges for tungsten carbide and MMC [40]

Product	Hard Phase composition (wt. %)			Matrix alloy composition (wt. %)						
	Phase %	W	C	Phase %	Ni	Cr	B	Si	C	Fe
PlasmaDur 51122	60	93.8	6.0	40	Bal.	9.5	2.0	3.3	0.3	2.0
		94.0	6.2			12.5	2.5	4.3	0.6	3.5

The feedstock material used in the study is the pre-blended mixture of tungsten carbide (WC) and nickel-based alloys (MMC) obtained from OErlikon Metco [40], and the powder trade name is PlasmaDur 51122. This powder density ranges from 5.5 to 7.0 g/cm^3 and has a +63 to –180 microns particle size distribution. A tungsten carbide possesses an angular shape, whereas an MMC has a spheroidal form. The chemical composition of the powder is represented in Table 3-1. The processing parameters used in the PTA-AM experiments are shown in Table 3-2. The experiments were performed with constant values except for the plasma arc current.

Table 3-2 Processing parameter for experiments

Processing Parameter	Value
Plasma arc current	60 & 100 Amp
Powder flow rate	27 gram /min
Travel speed	600 mm / min
Stand-off distance (SOD)	7 mm
Powder gas	1.5 slpm
Center gas	1.5 slpm
Shield gas	12 slpm

3.4 Image processing methodology

This section describes the 2D image processing program to detect the individual powder particles from the powder streams and determine their trajectories and velocities. The image processing has been done using image analysis software named Image Pro 10 (Media Cybernetics). The image processing technique involves importing high-speed images and calibrating them spatially, followed by three primary steps, as shown in Figure 3-4. The pre-processing step aims to augment the quality of the raw images obtained from the high-speed camera to improve the image analysis accuracy. The motion tracking steps focus on threshold selection for particles detection, particles segmentation for clusters particles and tracking of segmented particles.
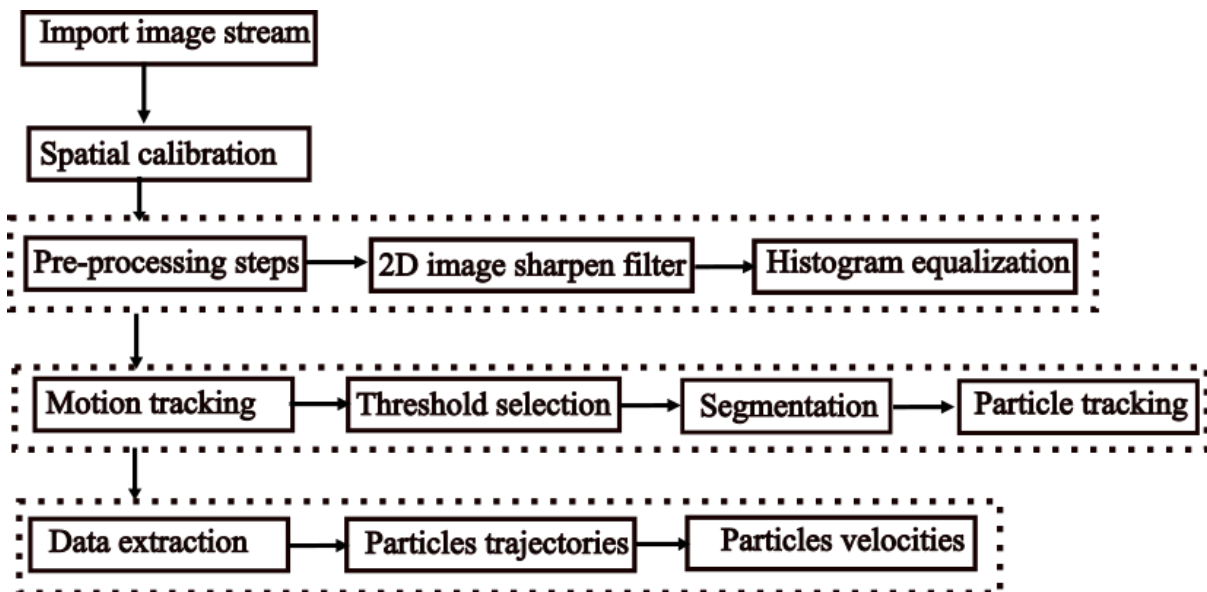
Figure 3-4 Flowchart of the proposed image processing technique

The final step involves the data extraction from the image analysis software. The detailed procedures of the image processing technique are shown in Figure 3-5. The proposed method begins with recording a stream of high-speed images and importing them into the Image-Pro 10

software. The images obtained during the injection of powder particles from both the nozzles can be indicated as a stream of images denotes as $I = \{I_1, I_2, I_3 \ldots, I_n\}$, where I_n is the nth image of 1023×767 pixels resolution as shown in Figure 3-5 (a). 100 consecutive recorded images were used for the image analysis in this methodology. Δt is the time interval between two successive high-speed images, which is the function of frame rate (fps) of the high-speed imaging (7500 fps). Calibration of the images has been performed using the center-to-center distance of 8 millimetres between the nozzles (Figure 3-5 (b)). The pixel dimensions were converted to millimetre measurements using the spatial calibration of the images. Based on the image resolution of 1023×767 pixels, the pixel size was determined to be 20 μm × 20 μm, and the scaling factor was 0.01 mm/pixel.
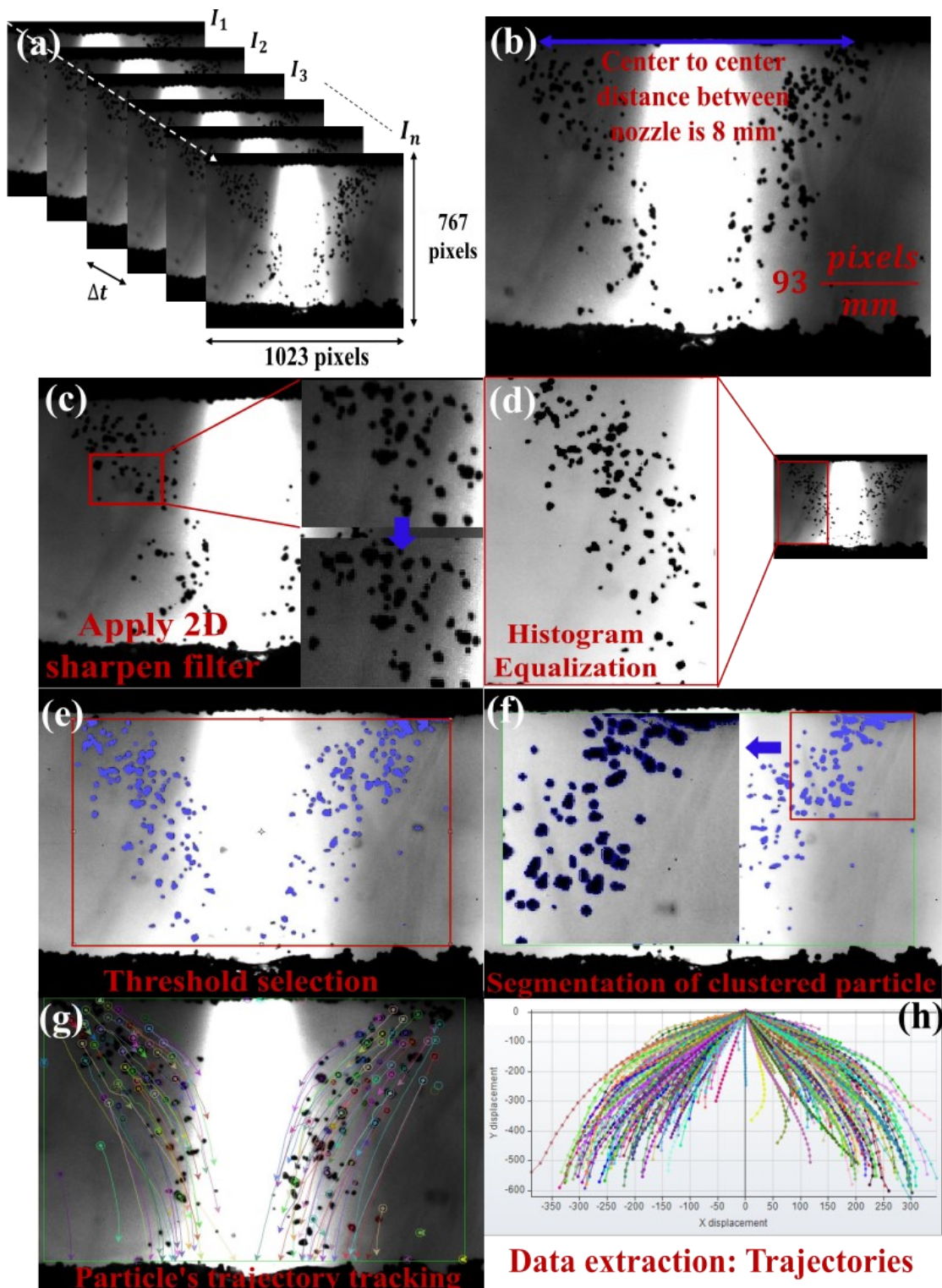
Figure 3-5 Image processing steps: (a) Import image streams (b) Spatial calibration; Pre-processing steps : (c) 2D filter for image sharpening (d) Histogram equalization; Motion tracking: (e) Threshold selection for particle detection (f) Segmentation for clustered particle separation (g) Tracking of particles trajectory (h) Extracted particle trajectories

Images recorded with high speed in the experiment undergo noise introduced by various factors, such as background noise and non-uniform brightness values, which reduces the image's quality. Even with ND filters and backlight sources, the intensity of the plasma arc from the images can not be effectively suppressed. To detect the particles in the high intense plasma arc, less exposure is used to detect particles with sphere edges in the image. The minimum exposure values while high-speed imaging causes the optical vignetting effect (brightness falls off the images' corners) [41]. In addition, non-uniformity in the brightness of the images cause due to the Gaussian distribution of plasma arc.

Three-dimensional flow through the nozzles cannot be ignored. The depth of field with a single camera can only detect particles within 500 μm whereas the nozzle can sprinkle particles up 3 mm along the periphery of the nozzle exit. This results in blurry powder particles which are outside the focal plane. Therefore, as shown in Figure 3-5 (c) and (d), the pre-processing is designed to bring out the images' details, eliminate noise from the images, and improve their features for further processing using a 2D filter for sharpening and histogram equalization. From Figure 3-5 (c) and (d) insets, we can see images after the 2D sharpen filter has been applied, and after the histogram equalization filters, we have uniform brightness and noiseless background. The image's contrast has been improved using histogram equalization to eliminate skewness caused by dark or light patches. It helps expand the histogram of the image into broader distribution.

With the pre-processed images, the subsequent step in image processing is 2D motion tracking, which tracks the movement of objects that are detected in an image sequence as they change over time and space. The first step in motion tracking is to separate all the possible powder particles from the image (background). An image is segmented based on common attributes using the

threshold technique. It is used to identify the black powder particles from high-speed images. A threshold is applied to images with an assessment of the values obtained from the bimodal distribution (one prominent peak for the black particles and plateau for the background) of an automatic histogram to detect black particles. As shown in Figure 3-5 (e), the region of interest (ROI) (dotted line box) was segmented from the raw high-speed images, and unwanted portions were removed to reduce the processing time and complexity. In ROI, the detection of the black particles can be observed after selecting optimum threshold values based on the intensity concentration of the image histogram. The second step in motion tracking is the segmentation of the clustered particles. Figure 3-5 (f) shows the clustered powder particles at the entrance of the nozzle exit. The clustered particles are separated on the base of the watershed algorithm inbuild in image analysis software. The watershed option splits the objects using the watershed algorithm, which erodes the objects until they vanish and amplify them again, so they do not touch each other [42]. The detailed view in Figure 3-5 (f) shows the individual particles, especially at the position where the particles clustered at higher concentrations. Tracking the individual particles is the third step in motion tracking and identifying dynamic changes in translatory motion. This dynamic change is quantified through a temporary displacement of the particles from frame to frame. As shown in Figure 3-5 (g), the translational motion of detected particles is tracked through frames to compare their positions between consecutive pairs of frames. The trajectory of the particles is completed once they impact the substrate. To achieve the entire trajectories of the particles (from nozzle exit to substrate), the tracking of the particles continued for 100 consecutive frames. In the 2D motion tracking of individual particles, it is assumed that particle trajectories were not interconnected, and no particles were mistracked with other particles. Once all the possible detected particle trajectories are tracked, data extraction is the final step in an image processing

methodology. Figure 3-5 (h) shows the variation in x and y coordinates (in pixels) of the particles with respect to space and time (Δt). Further, this information was used to calculate the resultant velocities of the detected particles.

3.5 Theoretical model

3.5.1 Single powder particle trajectory model

A powder particle is obliquely injected into the plasma arc while entering from the nozzle exit, as shown in Figure 3-6. As a result, the particle is subjected to the forces affecting its projectile motion in the plasma gas flow field. A single particle's conservation of momentum equations is obtained by equating the particle motion with drag and body forces. The velocity and trajectory of Nickel powder particles with respect to time can be calculated using the particle momentum equation [43][44].

The proposed analytical trajectory model is based on the following assumptions:

1. The plasma arc flow is a steady-state and fully developed regime for velocity distribution along with the arc radial distance. Particle initial velocity is constant, and it is normal to the nozzle exit plane.

2. The Nickel powder particles are spherical, and the inter-particle collisions are ignored.

3. The drag, gravitational and inertial force is considered to be significant contributors.

The equation of particle motion is reduced to include the effect of only drag force and body force with consideration of the given set of assumptions. The momentum equation for a single particle injected along the central nozzle axis and flowing into plasma arc, as shown in Figure 3-6 (b), can be expressed as

$$\vec{F}_{momentum} = \vec{F}_{drag} + \vec{F}_{body} \qquad (1)$$
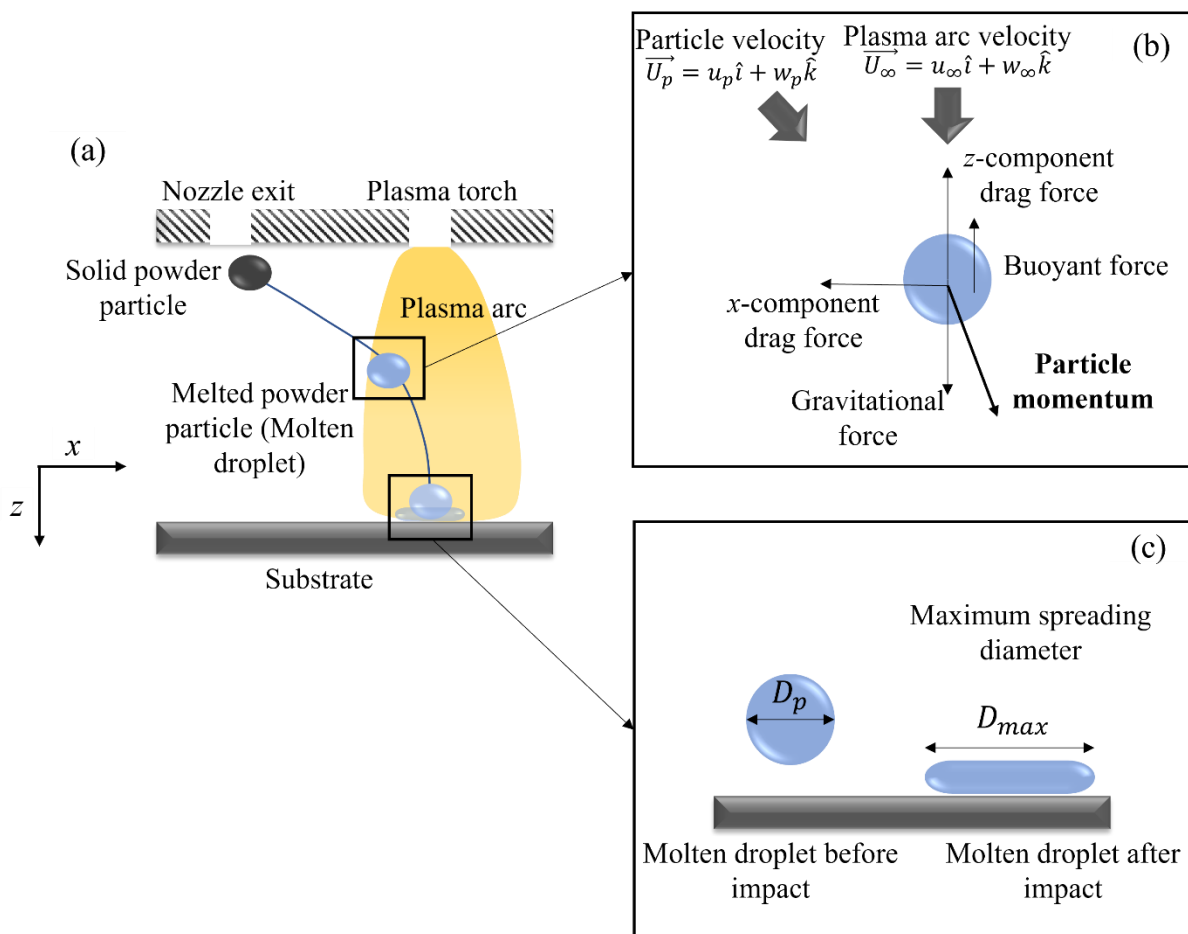
Figure 3-6 (a) Schematic of single-particle trajectory in the plasma arc region, (b) Force balance on the molten droplet, (c) Molten droplet spreading upon impingement on a substrate.

The drag force on the particle in the plasma fluid can be expressed as the integral of plasma fluid forces acting on the powder particle.

$$\vec{F}_{drag} = -\frac{1}{2}\rho_\infty A_p C_d \vec{U}_r |\vec{U}_r| \quad (2)$$

The drag coefficient (C_d) in Eq. 2 is the function of particle Reynolds number (Re_p). For a Stokes flow $(Re_p \ll 1)$, as the frictional forces dominated on the particles in a viscous fluid, which implies that the stokes' drag force $(3\pi \mu D_p \vec{U}_r)$ can be considered in momentum balance equation for a particle, and the drag coefficient is defined,

$$C_d = \frac{24}{Re_p} \quad (3)$$

The drag force coefficient for the particles of Reynold number is greater than 1, i.e., non-Stokes flow; the drag coefficient can be calculated as:

$$C_d = \frac{24}{Re_p}(1 + a(Re_p)) \quad (4)$$

where a is the function of particle Reynolds number as determined in Proulx et al.[45]:

$$a\left(Re_p\right) = 1 \qquad\qquad\qquad Re_p < 0.2$$

$$a\left(Re_p\right) = 1 + \frac{3}{16} Re_p \qquad\qquad\qquad 0.2 < Re_p < 2$$

$$a\left(Re_p\right) = 1 + 0.116\, Re_p{}^{0.81} \qquad\qquad\qquad 2 < Re_p < 20$$

$$a\left(Re_p\right) = 1 + 0.189\, Re_p{}^{0.632} \qquad\qquad Re_p > 20$$

Where, Re_p is the particle Reynolds number and is defined as follows

$$Re_p = \frac{\rho_\infty |\vec{U}_r| D_p}{\mu_\infty} \qquad (5)$$

The particle Reynolds number is estimated using particle diameter and the relative velocity (U_r) between the particle and plasma arc, is given by

$$|U_r| = \sqrt{\left(u_p - u_\infty\right)^2 + \left(w_p - w_\infty\right)^2} \qquad (6)$$

The particle velocity components in axial and radial directions were considered for relative velocity due to the dominant effect of gravity and drag on a single particle in that direction. The plasma arc velocity has two components. The velocity in the z-direction dominates the x-direction, which is set to zero in this calculation. Additionally, the third component of particle velocity (in the y-direction) is not considered since there is no force applied in that direction. The falling of powder particles under the plasma arc region is due to the gravitational acceleration and density difference between the particle and surrounding plasma fluid. In the momentum balance of particles, the body force, which includes the gravitational effect and the buoyant force due to the density difference, is defined as follows:

$$\vec{F}_{body} = \left(\rho_p - \rho_\infty\right)V_p \vec{g} \qquad (7)$$

Using Eqs. 2 and 7 in Eq. 1 yield to the following axial momentum and radial momentum equations

of particle motion[46]:

$$\frac{du_p}{dt} = \frac{\frac{-1}{2}\rho_\infty(u_p - u_\infty)|U_r|A_p C_d}{\rho_p V_p} \qquad (8)$$

$$\frac{dw_p}{dt} = \frac{\frac{-1}{2}\rho_\infty(w_p - w_\infty)|U_r|A_p C_d + (\rho_p - \rho_\infty)V_p g}{\rho_p V_p} \qquad (9)$$

$$\frac{dx}{dt} = u_p \qquad (10)$$

$$\frac{dz}{dt} = w_p \qquad (11)$$

The Eqs. 10 and 11 have been substituted in the momentum equation of particles to predict a

particle's analytical trajectory coordinates with respect to time. The MATLAB software used a 4th

order Runge-Kutta numerical method to solve the ordinary differential Eqs. 8 to 11. This approach

describes the particle trajectory until it arrives inside the plasma arc; the moment particle penetrates

the high-temperature plasma arc, we assume it instantly changes to the liquid phase due to thermal

transfer to and from particles occurring through radiation, convection, and mass transfer [47]. We

implement the molten droplet (melted powder particle) model as described in the next section.

3.5.2 Spreading factor of a molten droplet

When a molten droplet impinges on the substrate with sufficient impact velocity, it spreads at its

maximum extent and simultaneously, it solidifies due to the heat exchange between the substrate

and molten droplet. The molten droplet's spreading and solidification phenomena are influenced by its material properties, impact velocity, droplet volume, and wettability properties. In the PTA-AM process, the impingement of streams of molten droplets on the substrate forms the material layer and repetition of this process layer by layer forms a 3D part. It can be seen that the impact behaviour of the molten droplets (spreading and solidification) onto the substrate characterizes the quality and geometrical properties of the final fabricated part. Therefore, examining the maximum spreading of a molten droplet on the substrate is crucial in the process. Energy consumption is applied to travelling drops before and after the impact [48], as shown in Figure 3-6 (c).

The energy stored in the molten powder particle before impact = Kinetic energy (KE_1) + Surface energy (SE$_1$).

$$KE_1 = \frac{\pi}{12} \rho_p V_i{}^2 D_p{}^3 \qquad (12)$$

$$SE_1 = \pi D_p{}^2 \sigma_{LV} \qquad (13)$$

The energy stored in the molten powder particles after impact when the particle diameter is at maximum extension = Kinetic energy (KE_2) + Surface energy (SE$_2$) + W_{1-2} .

During the impingement of molten droplets on the substrate, the kinetic energy stored in it is transformed into the surface energy by increasing the surface area of the droplet at maximum spreading extension and loss of energy due to viscous dissipation of the molten droplet. Therefore, at this phase, the kinetic energy (KE_2) of the droplet at the maximum spreading condition is considered as zero, and surface energy is determined by three interfacial forces, namely, solid-

liquid interfacial energy (σ_{SL}), liquid-vapor surface energy (σ_{LV}), and solid-vapor surface energy (σ_{SV}). The relationship between interfacial energies and contact angles can be determined by using Young's equation, since liquid and solid vapors are not readily available. The total surface energy (SE_2) can be approximately considered as:

$$SE_2 = \frac{\pi}{4} D_{max}{}^2 (\sigma_{SL} - \sigma_{SV})$$

$$\sigma_{LV} \cos \theta_e = \sigma_{SL} - \sigma_{SV}$$

$$SE_2 = \frac{\pi}{4} D_{max}{}^2 \sigma_{LV} (1 - \cos \theta_e) \tag{14}$$

The energy loss during the deformation of molten particles against the viscosity from phase 1 to 2 is given by:

$$W_{1-2} = \int_0^{t_c} \int_{V_p} \varphi \, dV \, dt \approx \varphi \, V_p t_c \tag{15}$$

For the viscous dissipation, $\varphi = \mu_p \left(\frac{\partial u_i}{\partial x_j} + \frac{\partial u_j}{\partial u x_i} \right) \frac{\partial u_i}{\partial x_j} \approx \mu_p \frac{U_c{}^2}{t_c{}^2}$ (16)

The model also estimated the time required for the molten droplet to spread on the substrate at the maximum extension diameter by considering the cylindrical disk shape formation from the truncated droplet, as shown in Figure 3-7. The thickness of the droplet after the impingement, when the droplet is at maximum spreading diameter i.e., $D' = D_{max}$, can be determined using the conservation of molten droplet volume before and after the impact on the substrate.

$$h = \frac{2 D_p{}^3}{3 D_{max}{}^2} \qquad (17)$$

The conservation of momentum has been applied between the bottom of the truncated sphere shape particle and the spread particle. The truncated shape molten particle of diameter D_p and impact velocity V_i formed the cylindrical disk shape of diameter D' and radial velocity V_{radial} as the molten liquid flows through the area of diameter D_t. This equated the given equation as follows:

$$\frac{V_{radial}}{V_i} = \frac{3 D_{max}{}^2}{32 D_p D'} \qquad (18)$$
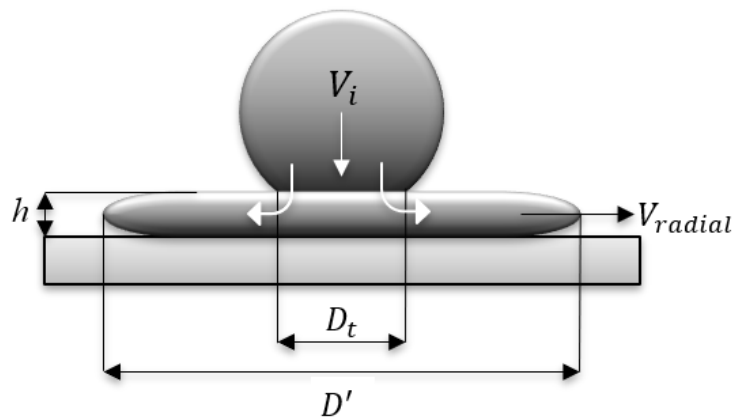
Figure 3-7 Schematic of the formation of cylindrical disk shape of the molten droplet from a truncated sphere shape

From the literature [50], it can be considered that the diameter $D_t \approx \frac{D'}{2}$ as D_t varies from 0 to D'. The radial velocity (V_{radial}) can be calculated by integrating the rate of change of spreading diameter (D') with respect to the time taken for the molten droplet to spread on the substrate. This can be written in the form of a given equation as follows:

$$\frac{dD'}{dt} = 2V_{radial} = \frac{3\,D_{max}{}^2}{16\,D_pD'}V_i \qquad (19)$$

As Eq. 19 integrated for a limit of diameter between 0 to D' and time varies from 0 to t. The resulted equation can be written as follows [159]:

$$\frac{D_{max}}{D'} = \sqrt{\frac{8}{3}t^*} \qquad (20)$$

The total time required for the particle to spread at maximum diameter can be calculated using Eq. 20, where dimensionless time $(t^*) = \frac{8}{3}$ at $D_{max} = D'$. It can be obtained as

$$t_c = \frac{8\,D_p}{3\,V_i} \qquad (21)$$

Eq. 16 - 21 can be used in Eq. 15 to determine the loss of energy due to the viscous dissipation of molten particles during impact. This can be expressed in the form of the following equation.

$$W_{1-2} = \frac{\pi}{3}\rho_p V_i{}^2 D_p D_{max}{}^2 \frac{1}{\sqrt{Re}} \qquad (22)$$

In order to apply the law of conservation of energy before and after particle impact, the equation becomes as follows:

$$KE_1 + SE_1 = KE_2 + SE_2 + W_{1-2} \qquad (23)$$

The maximum spreading of powder particles has been formulated using Eq. 12 to 22 in Eq. 23. The resulted equation for the maximum spreading can be written as

$$\xi_{max} = \sqrt{\frac{We+12}{3(1-\cos\theta_e)+4\frac{We}{\sqrt{Re}}}} \qquad (24)$$

The effect of inertial, viscous and surface tension forces on the maximum spreading factor (using dimensionless number $Re = \frac{\rho_p D_p V_i}{\mu_p}$, $We = \frac{\rho_p D_p V_i^2}{\sigma_{LV}}$) can be determined using Eq. 24. Moreover, the effect of solidification on the restriction of molten droplet spreading is also investigated by assuming that all kinetic energy stored in the solidified droplets has been lost after the droplet spreads. If the cylindrical disk shape solid layer of mean thickness h and diameter D' at the maximum spreading condition, then the loss of kinetic energy can be written as given below:

$$\Delta KE = \frac{\pi}{8}D'^2 h\rho_p V_i^2 \qquad (25)$$

In the Eq. 25, the D' varies from 0 to D_{max} during the droplet spreading, the average value is taken as $D' \approx \frac{D_{max}}{2}$. The energy balance equation by including the term of loss of kinetic energy during solidification can be written as:

$$KE_1 + SE_1 = \Delta KE + SE_2 + W_{1-2} \qquad (26)$$

By substituting Eq. 12 to 25 in Eq. 26, the maximum spreading factor expression formulated as follows:

$$\xi_{max} = \sqrt{\frac{We+12}{\frac{3}{8}We\,h^* + 3(1-\cos\theta_e)+4\frac{We}{\sqrt{Re}}}} \qquad (27)$$

The h^* in Eq. 27 is the dimensionless solid layer thickness ($h^* = \frac{h}{D_p}$). It is the function of Stefan

number ($Ste = \frac{C_p(T_p-T_s)}{h_f}$), Peclet number ($Pe = \frac{C_p\,V_i\,D_p\,\rho_p}{k_p}$) and dimensionless time ($t^* = \frac{tV_i}{D_p}$). The

equation for h^* can be written using the following simplified assumptions such as [52]: heat

transfer is by 1D heat conduction; the substrate temperature is constant; thermal contact resistance

at the molten droplet-substrate interface is negligible; Stefan number is small; and h^* increases

with the dimensionless time (t^*). The equation for the dimensionless solid layer thickness is:

$$h^* = \sqrt{2t^*\frac{Ste}{Pe}} \qquad (28)$$

The substitution of Eq. 28 and $t^* = \frac{8}{3}$ from Eq. 20 into the Eq. 27 gives the expression for maximum

spreading factor of the solidifying molten droplet during impingement on the substrate is [48]:

$$\xi_{max} = \frac{D_{max}}{D_p} = \sqrt{\frac{We+12}{We\sqrt{\frac{3\,Ste}{4\,Pe}} + 3(1-\cos\theta_e)+4\frac{We}{\sqrt{Re}}}} \qquad (29)$$

In Eq. 29, the three terms in the denominator signify the effect of droplet solidification, surface

tension, and viscous dissipation on the maximum spreading diameter of the molten droplet.

We have presented the particle trajectory in two phases: the solid and liquid phases. In the result

and discussion section, we first investigate the solid phase by analyzing the range of particle

trajectories and velocities under plasma arc current. Once we quantify the particle entrance velocities inside the plasma, we further analyze powder particle trajectory and velocity variations under 60 A and 100 A plasma arc currents; the image stream of the powder flow was processed in software to produce high-speed images. These results were later validated with theoretically determined ranges. A parametric study is also conducted using this flow behaviour of powder particles to determine the effect of impact velocities on the spreading and solidification of the molten droplet.

3.6 Result and Discussion

3.6.1 Theoretical investigation of particles trajectory and impact velocity

Figure 3-8 shows the solution for Eq. 8 to 11, resulting in the variation of particle trajectories and molten particles' impact velocities under the influence of plasma arc velocity. The particle trajectory and impact velocity are represented as two *y*-axes based on the *x*-axis, which represents the *x*-coordinates of the particle trajectory. The inset of Figure 3-8 demonstrates that the plasma arc velocity is the function of plasma arc current and radial distance of plasma arc, which we determined using the following semi-empirical equation [33].

$$V_\infty(r) = \frac{\sqrt{30\,\omega}I}{6\pi r_*\sqrt{\rho_\infty}}\sqrt{\left(1 - \frac{12r^2}{5r_*{}^2} + \frac{9r^4}{5r_*{}^4} - \frac{2r^6}{5r_*{}^6}\right)} \qquad (30)$$

Input parameters for I, r_*, ω and r, can be used to determine the plasma's maximum axial velocity on the plasma arc axis and the velocity distribution along with the arc column radial distance. Figure 3-8 inset shows that plasma arc velocity at the center of the plasma arc reaches almost 100 m/s and 61 m/s when the plasma arc current is 100 A and 60 A, respectively. Plasma fluid

accelerates the particles once they are introduced into the arc space by the carrier gas. Plasma currents of 60 and 100 A were used in the experiment to determine the effect of plasma arc velocity on the powder particle trajectory. Therefore, the plasma arc velocity range from 0 to 100 m/s has been selected to analyze the particle trajectory shift and impact velocity. The impact velocity is defined as the velocity at which the molten droplets is impacting the bed or solid substrate for solidification.
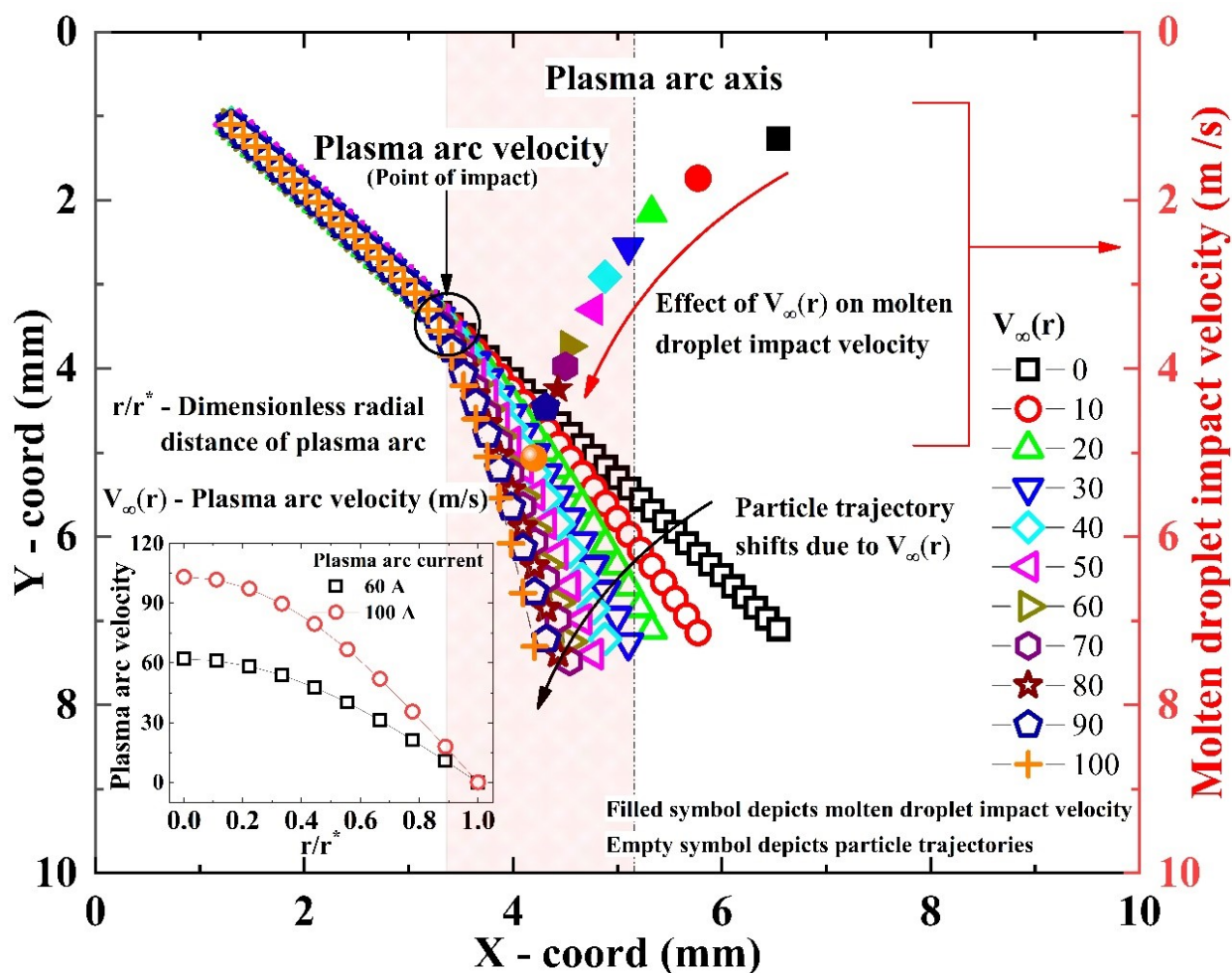
Figure 3-8 Theoretical powder particle trajectories and impact velocities of molten droplets under the effect of plasma arc velocity. The inset figure shows the plasma arc velocity as the function of plasma arc current and dimensionless radial distance of plasma arc

In order to validate the theoretical analysis with experimental observations, the experimentally investigated particles' initial coordinates and velocities from image analysis have been used in Eqs. 8 - 11 to determine the powder particles' theoretical trajectories and impact velocities of molten droplets.

The highlighted region in Figure 3-8 denotes the plasma arc zone; the instant particle enters this zone; it not only gains momentum due to plasma arc velocity but also changes its phase from solid to liquid. The point of impact, where the plasma arc velocity is applied on the incoming powder particles, is 2 mm from the plasma arc axis. With the introduction of plasma arc velocity in the theoretical model, we have determined the particle velocities and trajectories, assuming that as the particle enters the plasma arc, it will travel under constant plasma arc velocity.

It is evident from Figure 3-8 that, as the plasma arc velocity increases, the particle trajectory changes. i.e., the trajectory moves away from the plasma arc axis. Specifically, when plasma arc speeds reach 60 m/s and 100 m/s, there is a trajectory shift of 0.8 and 1 mm from the plasma arc axis position. The molten droplet's impacting location on the substrate for plasma arc speeds of 30 to 100 m/s is observed within the plasma arc region. In contrast, the molten droplets are overshooting the plasma arc region for plasma arc speeds between 0 and 20 m/s. The RHS y-axis in Figure 3-8 denotes the molten droplet impact velocity, which varies with respect to the plasma arc velocity. The molten droplets have an impact velocity of 1.2 to 5 m/s while approaching the substrate, which varies based on plasma arc velocity.

3.6.2 Particles trajectory and velocity variation for plasma current of 60 and 100 A

In Figure 3-9, based on image processing, the trajectories and velocity of powder particles with respect to space and time have been determined. It is compared to the theoretical model presented in Section *3.6.1* and the results demonstrated in Figure 3-8. As shown in Figure 3-9, six particles have been selected from the center of the nozzle exit. Using a mean value of these particles coordinates in the theoretical model, the theoretical trajectories and velocities have been validated with the experimentally determined particles trajectories and velocities.

Plasma currents of 60 and 100 A were used to determine the effect of plasma arc velocity on particle motion dynamics. The semi-analytical equation with an empirical constant for plasma arc velocity as a function of current is presented in Eq. 30. For 60 and 100 A, the trajectories of the exited particles from the nozzle and the impact velocities of six different particles. The shaded region labelled 'theoretical region for trajectories' and ' theoretical region for velocities' are theoretical prediction ranges for varied plasma arc velocities with 60 and 100 A. It is worth mentioning that the plasma arc velocity has gaussian distribution; hence, a minimum to a maximum range of plasm arc velocity, for a given applied current, is considered to predict a theoretical range of trajectories and impact velocities. The bounding region for the theoretical prediction between these two velocities is shaded (empty symbols for minimum and maximum velocities) and labelled as 'theoretical region.' The experimental results obtained after the image analysis are within this theoretical domain, demonstrating good confidence in the proposed theoretical model. After comparing the 60 A and 100 A results, we can say that the trajectories overlap for higher current and lower currents particles are diverging more.
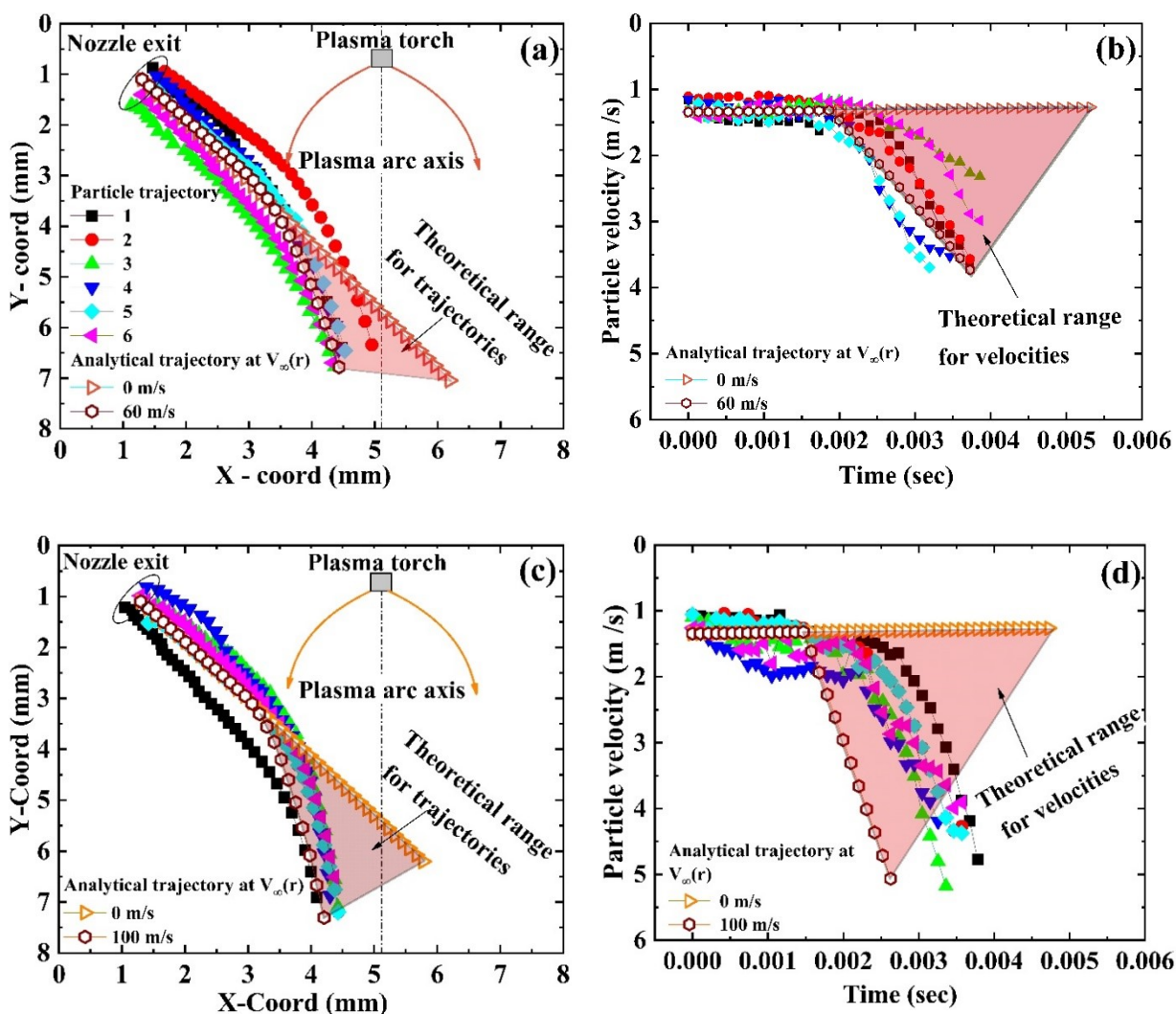
Figure 3-9 Tracking of six powder particle trajectories from the center of the nozzle under the plasma arc current of (a) 60 A (c) 100 A, and the respective six particle velocities under the plasma arc current of (b) 60 A (d) 100 A. The highlighted region represents the theoretical range for particles trajectories and velocities. The filled symbol denotes experimentally calculated trajectories and velocities. The empty symbol signifies theoretically determined particle trajectories and velocities.

Moreover, with the increase in current by 40%, the impact velocities have increased from 2.4 – 3.6 m/s to 4.5 – 5.2 m/s. These powder particle impact positions and impact velocities significantly affect the final geometry of the melt pool zone [53], [54], and it is evident from this analysis that

based on the systems requirement, by tuning the current one can assure the diverging angle and the impact velocities of the particles from the centre of the nozzle.

In Figure 3-9, we made an idealistic assumption of particle exit location, which was along the centre of the nozzle, but one can argue on the different exit positions; therefore, in Figure 3-10, we studied for three different nozzle exits, I – corner of the nozzle farthest from plasma arc, II – the centre of the nozzle (similar to Figure 3-9 analysis) and III – closest nozzle corner to the plasma arc. Since we are studying the entire nozzle section, we tagged eight more particles to the analysis performed for the only central region, i.e., Figure 3-9, analysis.

As mentioned earlier, in Figure 3-10, the 14 powder particles were tracked using the image analysis method at three different exit positions of the nozzle. A maximum number of particles that can eject from the nozzle for 27 gm/min can be up to, but we are considering representative particles that are in focus for our analysis. This exercise evaluates the effect of plasma arc current on the powder particles with different initial locations from the plasma arc.

Zone I is the farthest from the arc envelope; hence the effect of the arc and pertinent operating current is minimal on the particle trajectories (Figure 3-10 (a) and (c)) in turn, the velocities (Figure 3-10 (b) and (d)) as depicted in all four figures. An increase in the current from 60 to 100 A has certainly reached the arc up to the particles which are ejecting from the farthest most edge of the nozzle, but the effect of this arc is marginal; one can make this comment by observing the Zone I trajectories with 100 A (Figure 3-10 (c)) where particles are travelling in the marginally non-linear path - as compared to the 60A (Figure 3-10 (a)) case – in particular very close to the bed where the arc influences the particles' trajectories.
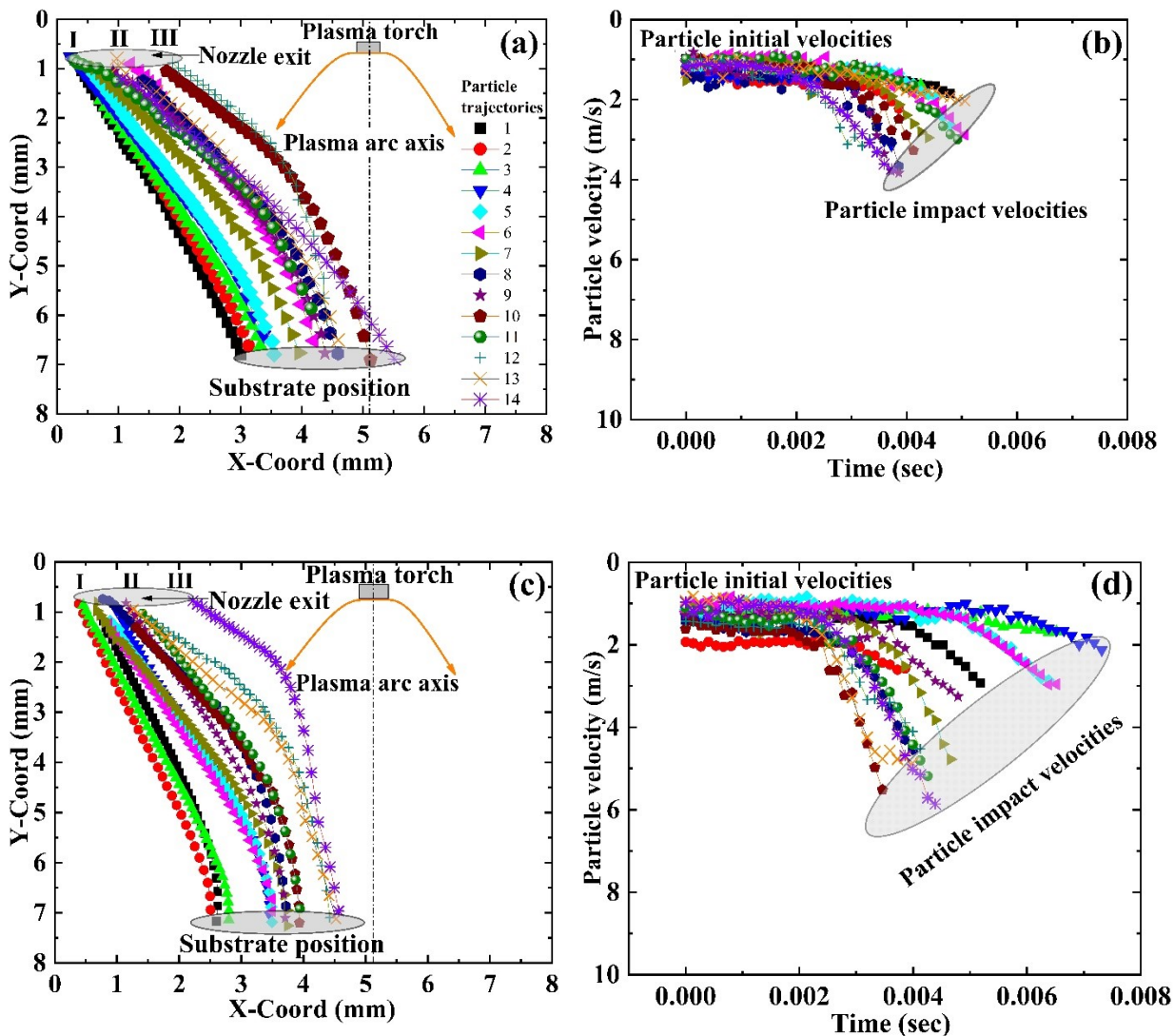
Figure 3-10 (a) Represents trajectories of Fourteen particles from the nozzle exit to substrate position under the plasma arc current of 60 A, (b) Velocities of 14 particles tracked from nozzle exit to substrate under 60 A, (c) Represents trajectories of Fourteen particles from the nozzle exit to substrate position under the plasma arc current of 100 A, (b) Velocities of 14 particles tracked from nozzle exit to substrate under 100 A

The Zone II scenario is the same as Figure 3-9, where the particles leave from the centre of the nozzle and more than half of the trajectory length of particles under the arc envelope. This ultimately affects the particle trajectories and velocity. As explained earlier, with an increase in the current, the particle ejecting zone was narrowed down. In Zone III, as anticipated, we noticed

the maximum influence of arc on the particle trajectories and resultant velocities since the particles are travelling directing through the arc and staying for the most prolonged period within the arc zone. This makes sure that the particles have increased their kinetic energy and have the necessary time to go through the phase transformation. It is worth mentioning that we are focusing only on one nozzle; based on our analysis, it is safe to assume that other nozzle particles will also behave similarly within the remaining half of the plasma arc.

In quantified terms, the impact velocity was increased due to increment in the current from the range of 1.8 - 2.6 m/s to 1.9 - 3 m/s, 3 - 3.6 m/s to 3- 5.5 m/s, 3.2 - 3.8 m/s to 6 m/s in Zone I, Zone II and Zone III, respectively. It can be concluded that as the plasma current increased by 40 %, the range of the impact velocity increased by around 53%. Overall, it can be seen that individual particles' impact velocity gradually increases as the initial coordinate position relative to the plasma torch position decreases. In addition, it can also be determined from Figure 3-10 is that for the plasma current of 60 and 100 A, with all the operating parameters kept constant, the particle's impacting position shifts away from the plasma arc axis as the plasma current increases. As shown in Figure 3-9 and Figure 3-10, the results showed the differences in the particle's motion path and the impact velocity of the molten droplet due to the plasma effect on powder particles. The position of powder particles trajectories and their resident time inside the high-temperature plasma arc determines particles' phase state before impact: fully or partially melted particles (molten droplet) [54], [55]. In addition, the impingement of the molten droplet on the substrate with particular impacting velocity determines their spreading and the solidification phenomena. These phenomena of molten droplets decide the microstructural properties and surface quality of the 3D parts [54]. The findings of particles trajectory and impact velocity from Figure 3-9 and Figure 3-

10 can be used in the PTA-AM process to predict individual molten droplet spreading solidification behaviour which can be helpful to produce the part with high quality and with good microstructural properties.

In previous sections, we attempted to analyze the experimental observation for particle trajectories starting from the nozzle to the bed while changing its phase. We also compared the simplified theoretical trajectories with the observed experimental results. However, the molten droplet impact and solidification of the molten pool are the critical phenomena that dictate the PTA-based AM process. Therefore, in the next section, we are elaborating briefly on the impact of the molten droplet and the solidification of the individual droplet.

3.6.3 Parametric study: Effect of impact velocities on spreading and solidification of molten droplet

Various research studies have been performed to investigate the metal droplet spreading phenomena, particularly for thermal spraying applications [56]–[58]. The metal droplet's spreading upon impact is governed by Reynolds (*Re*), Weber (*We*) number, and the bed's wettability or the surface on which the molten droplets are being impacted. It is to be noted that *Re* and *We* represent the thermophysical properties (density, viscosity, surface tension) and other process parameters (characteristic length and velocity) that affect the impact dynamics. For the simplification of spreading and solidification model, only the impact dynamics of Nickel molten droplet has been studied. The Nickel's physical and thermophysical properties at its melting point is considered and the impact of WC particles on the spreading and solidification of Nickel molten droplet is not considered in this model.
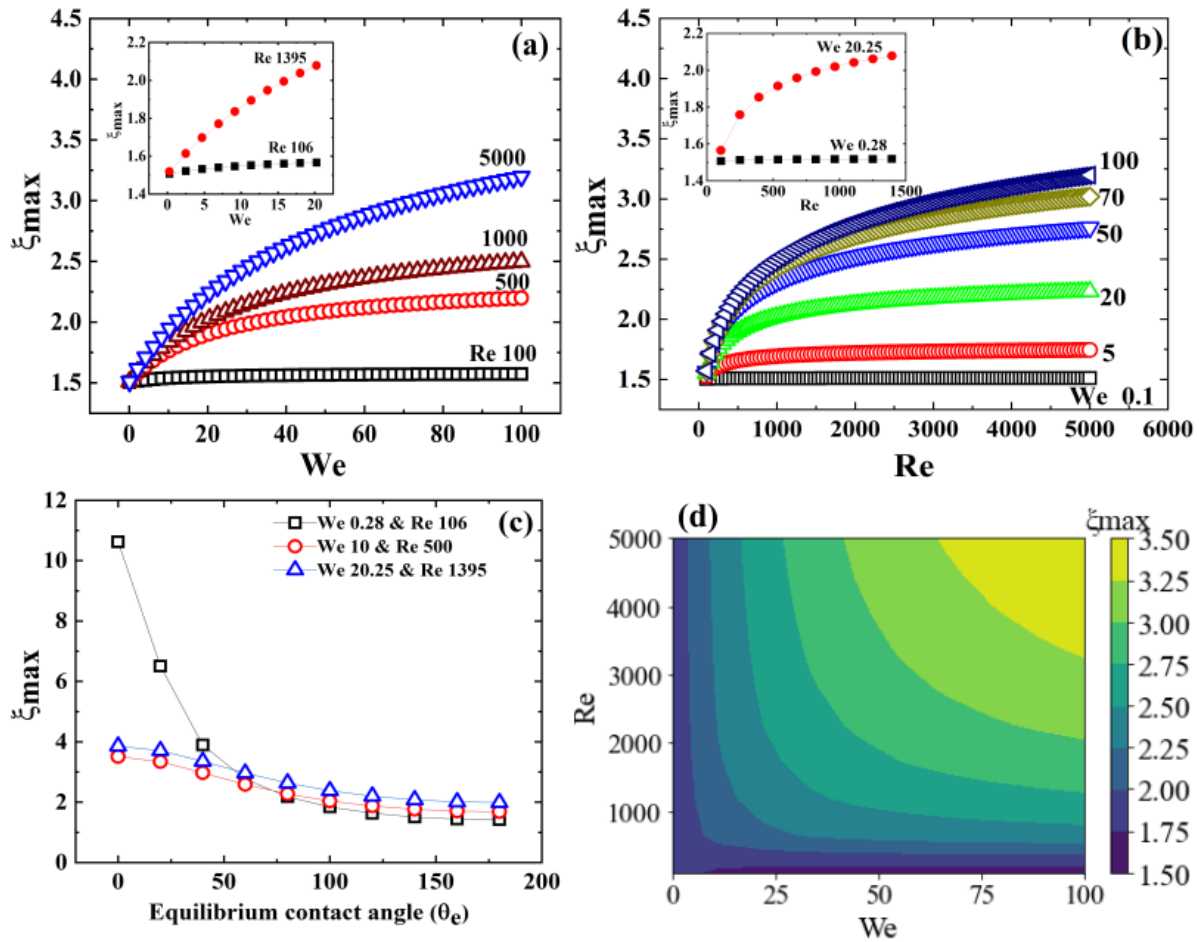
Figure 3-11 (a) Variation in ξ_{max} with respect to We for different Re number, (b) Variation in ξ_{max} with respect to Re for different We number, (c) Variation in ξ_{max} with respect to contact angle for different We and Re number, (d) Contour plot showing the relation between We, Re, and ξ_{max}

Figure 3-11 (a) shows the effect of surface tension and inertia in the molten droplet, i.e., *We* on a maximum spreading factor (ξ_{max}) of molten droplet for a different *Re*. Here, ξ_{max} is maximum deformation in the droplet after impacting while it is transforming the inherent surface and kinetic energy to the spreading process. For a small *We*, the surface tension of a molten particle is strong enough over the impact forces to restrict the spreading. As the impact velocity or the *We* increases, the inertial forces of the droplets dominate the surface tension forces, which leads to a greater

maximum spreading. The proposed model does not account for the breakup of the droplet and the rebound criteria; hence both the cases cannot be witnessed predicted in this case.

Figure 3-11 (a) inset shows the maximum spreading variation for a specific range of *We* with two *Re*; this case resembles the experimentally operating parameters. It is evident that as we increase the *We*, the droplets spreading is increasing monotonically. These results indicate that increasing the current increases the *Re* significantly, but the change in the maximum spreading is also significantly enhanced. Thus, we established the relationship between the operating current and the molten pool thickness since the higher the operating current higher the spreading and the smaller the splat thickness.

A similar argument can be made in relationship with *We*, as demonstrated in Figure 3-11 (b). It shows the effect of *Re* on the maximum spreading ratio for a different *We*. It signifies the ratio of inertial and viscous forces, and it defines how fast the viscous forces can dissipate the inertia of the molten droplet. As the molten droplet impinges on the substrate, the axial momentum is transmuted into radial momentum; however, the viscous effect restricts the droplet's total momentum, which causes the decrement in the radial velocities and lateral spreading. After careful observation of the inset of Figure 3-11 (b), the role of *We* diminishes (ξ_{max} attains the plateau) for very low Re. For example, with *We* = 20.25 around *Re* = 1500, the effect of *We* is negligible. However, the *Re* for 100 A is 1395; hence one can argue that for higher current, the inertia and surface tension forces are negligible due to higher order of kinetic energy with the impacting droplet. As mentioned earlier, the proposed model fails to comment on the breakup and rebound of the droplet; hence at a certain operating current, the drop might either rebound or break up, which requires further investigation. The *Re* and *We* range of 106 – 1395 and 0.28 – 20.25,

respectively, as shown in the inset of Figure 3-11 (a) and (b), were determined using the experimentally analyzed impact velocity range of 2 - 6 m/s and particles diameter range of 63 – 150 microns available from powder manufacturers. The ξ_{max} variation for the above-mentioned range of Re and We number has shown that the molten droplet could spread from 1.5 to 2.1 times their initial diameter after impacting the substrate or previously deposited layer.

The surface energy of the bed or molten pool is an important parameter that defines the maximum spreading. Figure 3-11 (c) depicts the effect of equilibrium contact angle (θ_e– which is the representation of the surface energy of a given surface) on the maximum spreading of a molten droplet over the substrate. For a smaller contact angle ($\theta_e < 90°$), the capillary force accelerates the spreading speed of the droplet-substrate contact line, resulting in maximum spreading of the impinged molten droplets. As the contact angle increases ($\theta_e > 90°$), the same capillary force tends to decelerate the spreading speed of the contact line [59]. In addition, the θ_e is closely correlated with the molten droplet's surface tension and changed along with the molten droplet-substrate interface. With the increment in θ_e, the peripheral interfacial forces squeeze the molten particle upward, as a result of the area of molten droplet-substrate decreases slowly. Figure 3-11 (c) confirms that as the θ_e increases, the ξ_{max} gradually decreases [60]. However, for values of $\theta_e >$ 120°, the dependency of ξ_{max} on θ_e is negligible. These findings indicate that for the $\theta_e < 120°$ substrate wettability properties (θ_e) play a considerable role in changing the molten droplet's spreading diameter. On the other hand, as the $\theta_e > 120°$, substrate wettability plays a very minor role in spreading droplet variation irrespective of increment in plasma current from 60 to 100 A (in the form of We and Re).

Figure 3-11 (d) summarizes all three figures – Figure 3-11 (a)-(c) by presenting the proportional relationship between Re, We, and ξ_{max} with phase plot for given surface energy or contact angle [61]. This sensitivity analysis represents the variation in ξ_{max} with respect to We and Re. The contour plot shows the two regimes, which explains the dominating region of either We or Re for the maximum spreading factor. It can be delineated that as We and Re increase, the ξ_{max} increases. This phase plot can be utilized as a guideline for the PTA-AM process by transforming the axes from Re to the operating plasma current or any other parameter that can relate to the inertia and viscous forces within the droplet.

In addition to the thermophysical parameters, the parametric study also briefly studied the solidification of the molten droplets. The magnitude of term $\alpha = We\sqrt{\frac{3\,Ste}{4\,Pe}}$ in Eq. 29 predicts the effect of solidification on the droplet spread. As the α is the function of Stefan (Ste) and Peclet (Pe) number, the individual impact of Ste and Pe on droplet spreading during the impingement is illustrated in Figure 3-12 (a) and (b), respectively. The solidification effect can be observed in the variation of Ste. The Ste signifies the importance of sensible heat to latent heat. A greater value of heat capacity or higher temperature gradient between molten droplet and substrate or a lower value of heat of fusion of droplet material accelerates the solidification process. With the Ste increment, the time required to solidify the molten droplet spread decreases. In this situation, the solidification process is so rapid that molten droplets have no time to spread to the maximum extent, which restricts them from spreading. This Ste influence can be observed from the results in Figure 3-12 (a), where the ξ_{max} decreases as the Ste increases from 0 to 100.
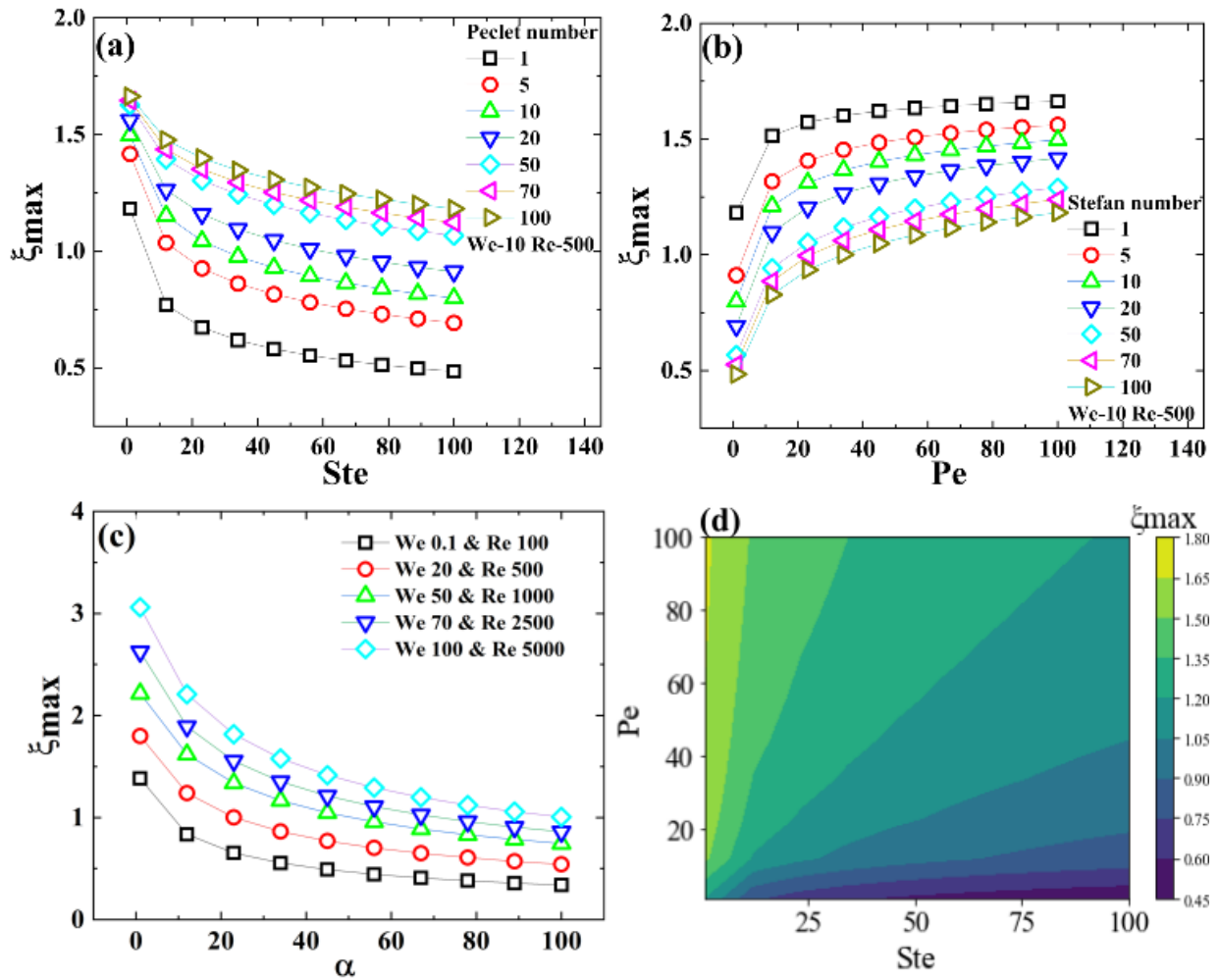
Figure 3-12 (a) Variation of ξ_{max} with respect to Ste for different Pe, (b) Variation of ξ_{max} with respect to Pe for different Ste, (c) Variation of ξ_{max} with respect to α for different We and Re, (d) Contour plot showing the interrelation among the Pe, Ste and ξ_{max}.

The *Pe* is a dimensionless number describing the ratio of heat transferred by motion of fluid to heat transferred by conduction. The *Pe* interrelates the spreading dynamics and solidification. As the *Pe* increases, the molten droplets spreading rate dominates the heat conduction and solidification, resulting in a negligible impact of the solidification on the final spreading shape [62]. With the increment in the impact velocity, which is the governing factor in the *Pe*, the spreading dynamics are controlled by the droplets' radial momentum and less impacted by the

solidification. As depicted in Figure 3-12 (b), the maximum spreading increases with *Pe*'s increment for a given *Ste*, *We* and *Re*. It is determined that as the *Pe* increases from 0 to 100, the ξ_{max} varies from the minimum range of 0.5 – 1.2 to the maximum range of 1.2 - 1.7. It can be clearly stated that the kinetic energy loss due to the solidification of the molten droplet during impingement is minimum to restrict the spreading. In Eq.29, the α term compared to the other two terms in the denominator determines whether solidification affects the spreading of the molten droplet. Figure 3-12 (c) depicts the parametric effect of the solidification term α on the ξ_{max} for a different *We* and *Re*. For $\alpha < 30$, a significant decrement in the spreading factor due to the solidification is observed. As the values of α increased above 30, the droplet spreading factor is almost constant irrespective of increment in *Ste* or decrement in *Pe* (in the form of α). With this inference, it can be depicted that the temperature gradient between droplet and substrate or heat transferred by fluid motion has an insignificant effect on the spreading of the droplet as the solidification term α increased above the 30 for a given operating parameter in the PTA-AM process. Moreover, Figure 3-12 (d) displays the proportional relationship between *Ste*, *Pe* and ξ_{max} , revealing the region for molten droplets spreading with solidification effect dominated by either *Ste* or *Pe*. This phase plot can be employed as a guideline for the PTA-AM process by transforming the axes from *Ste* and *Pe* to the operating parameters that relate the temperature gradient between molten droplet and substrate and the inertial forces acting on the droplet.

As we compare the results for maximum spreading factor from Figure 3-11 and Figure 3-12, it is shown that using Eq. 24, the ξ_{max} is in the range of 1.5 to 3.2 without considering the effect of solidification. On the contrary, using Eq. 29 by considering the impact of solidification, the ξ_{max}

is in the range of 0.2 to 2.2. It can be clearly stated that the solidification of molten droplets during impingement restricts the spreading of particles on the substrate.

3.7 Conclusion

Using high-speed imaging in the PTA-AM process and image processing technique to reveal the substantial influence of plasma arc current on the powder flow behaviour, including the following key finding:

1. The theoretical trajectory model discussed in this paper estimates the variation in particle trajectories and their impact velocities under the influence of plasma arc current, the function of plasma arc velocity. It is revealed that theoretically, as the plasma arc velocity increases, particularly from 60 to 100 m/s, the trajectories shift from 0.8 mm to 1 mm from the arc axis, respectively. The corresponding impact velocities are 3.25 to 5 m/s. Under the plasma current in the PTA-AM system, experimental results fall within the theoretically determined range of the trajectories and impact velocities. We measured the trajectory and velocity of midstream particles selected at the nozzle exit. As the plasma current increases by 40 percent (60 to 100 A), the particle's impacting position shifts from 4.5 to 5 mm to 4 to 4.5 mm with respect to the arc axis. The impact velocity range of particles also changes from 2.4 -3.6 m/s to 4.5 - 5.2 m/s.

2. This study also investigates the effect of plasma arcs on the powder stream ejecting from the nozzle. The powder stream away from the arc region conforms to a linear trajectory and minimal impact velocity. On the other hand, the part of the powder stream, which travels directly under the arc region, shows a significant deviation from the particle's

trajectories and higher impact velocities. A 40 % increase in plasma current shifted the particle impact location on the substrate from 3 to 5.5 mm to 2.5 to 4.5 mm. There was also a significant variation in impact velocity range from 1.7 - 3.9 m/s to 2.1 - 6 m/s.

3. The impact behaviour of the molten powder particles is studied under the parametric effect based on Pasandideh-Fard et al.[48] analytical model. This study demonstrated the impact of 6 main governing parameters such as *We, Re, θ_e, Ste, Pe* and α on the maximum spreading of molten particles. The molten droplet's impact velocity (*We* or *Re*) strongly affects the droplets' spreading dynamics and solidification behaviour. The molten droplets could spread from 1.5 to 2.1 times their initial diameter after impacting the substrate for the experimentally determined range of impact velocities.

4. For contact angle $(\theta_e) > 120^\circ$, the degree of dependency of maximum spreading on θ_e becomes negligible, which shows the less wettability effect on the droplet spreading phenomena. The effect of solidification on particle spreading was found to be insignificant for $\alpha > 30$. For a $\alpha < 30$, there is strong confinement in the particles spreading due to the solidification effect.

In the PTA-AM process, the results indicate that the plasma current regulates the flow characteristics of powders, which is responsible for spreading and solidifying individual powder particles. This study can predict the spreading of the individual particles upon impacting the substrate, which can be further extended to predict the possible geometry dimensions of the molten pool zone and the bead geometry for a given processing parameter.

References

[1]   T. DebRoy et al., "Additive manufacturing of metallic components – Process, structure and properties," Prog. Mater. Sci., vol. 92, pp. 112–224, 2018

[2]   J. G. M. Rojas, M. Ghasri-Khouzani, T. Wolfe, B. Fleck, H. Henein, and A. J. Qureshi, "Preliminary geometrical and microstructural characterization of WC-reinforced NiCrBSi matrix composites fabricated by plasma transferred arc additive manufacturing through Taguchi-based experimentation," Int. J. Adv. Manuf. Technol., 2021

[3]   El Moghazi, S. N., Wolfe, T., Ivey, D. G., & Henein, H. (2020). Plasma transfer arc additive manufacturing of 17-4 PH: assessment of defects. The international journal of advanced manufacturing technology, 108, 2301-2313

[4]   E. Herderick, "Additive manufacturing of metals: A review," Mater. Sci. Technol. Conf. Exhib. 2011, MS T'11, vol. 2, no. 176252, pp. 1413–1425, 2011

[5]   W. E. Frazier, "Metal additive manufacturing: A review," J. Mater. Eng. Perform., vol. 23, no. 6, pp. 1917–1928, 2014

[6]   H. Wang, W. Jiang, M. Valant, and R. Kovacevic, "Microplasma powder deposition as a new solid freeform fabrication process," Proc. Inst. Mech. Eng. Part B J. Eng. Manuf., vol. 217, no. 12, pp. 1641–1650, 2003

[7]   A. Dass and A. Moridi, "State of the Art in Directed Energy Deposition : From Additive Manufacturing to Materials Design," pp. 1–26, 2019

[8]   A. Aggarwal et al., "Role of impinging powder particles on melt pool hydrodynamics, thermal behaviour and microstructure in laser-assisted DED process: A particle-scale DEM – CFD – CA approach," Int. J. Heat Mass Transf., vol. 158, p. 119989, 2020

[9]   S. Zekovic, R. Dwivedi, and R. Kovacevic, "Numerical simulation and experimental investigation of gas-powder flow from radially symmetrical nozzles in laser-based direct metal deposition," Int. J. Mach. Tools Manuf., vol. 47, no. 1, pp. 112–123, 2007

[10]   I. Tabernero, A. Lamikiz, S. Martínez, E. Ukar, and L. N. López De Lacalle, "Modelling of energy attenuation due to powder flow-laser beam interaction during laser cladding process," J. Mater. Process. Technol., vol. 212, no. 2, pp. 516–522, 2012

[11]   E. Toyserkani, A. Khajepour, and S. Corbin, "3-D finite element modelling of laser cladding by powder injection: Effects of laser pulse shaping on the process," Opt. Lasers Eng., vol. 41, no. 6, pp. 849–867, 2004

[12]   S. J. Wolff et al., "In-situ Observations of Directed Energy Deposition Additive Manufacturing Using High-Speed X-ray Imaging," Jom, vol. 73, no. 1, pp. 189–200, 2021

[13]   H. Tan, F. Zhang, R. Wen, J. Chen, and W. Huang, "Experiment study of powder flow feed behavior of laser solid forming," Opt. Lasers Eng., vol. 50, no. 3, pp. 391–398, 2012

[14]   E. Govekar, A. Jeromen, A. Kuznetsov, M. Kotar, and M. Kondo, "Annular laser beam based direct metal deposition," Procedia CIRP, vol. 74, pp. 222–227, 2018

[15]   A. Singh, S. Kapil, and M. Das, "A comprehensive review of the methods and mechanisms for powder feedstock handling in directed energy deposition," Addit. Manuf., vol. 35, no. May, p. 101388, 2020

[16]   A. Tchikango Siagam, G. Brenner, P. Giese, and V. Wesling, "Numerical and experimental study of particle motion in plasma arc welding," Fluid Dyn. Mater. Process., vol. 4, no. 2, pp. 77–83, 2008

[17]   R. Anandkumar, A. Almeida, R. Vilar, V. Ocelík, and J. T. M. De Hosson, "Influence of powder particle injection velocity on the microstructure of Al-12Si/SiCp coatings produced by laser cladding," Surf. Coatings Technol., vol. 204, no. 3, pp. 285–290, 2009

[18]   U. de Oliveira, V. Ocelík, and J. T. M. De Hosson, "Analysis of coaxial laser cladding processing conditions," Surf. Coatings Technol., vol. 197, no. 2–3, pp. 127–136, 2005

[19]   T. Schopphoven, N. Pirch, S. Mann, R. Poprawe, C. L. Häfner, and J. H. Schleifenbaum, "Statistical/numerical model of the powder-gas jet for extreme high-speed laser material deposition," Coatings, vol. 10, no. 4, 2020

[20]   Liu, S., Zhang, Y., & Kovacevic, R. "Numerical simulation and experimental study of powder flow distribution in high power direct diode laser cladding process," Lasers in Manufacturing and Materials Processing, 2(4), 199-218, 2015.

[21]   H. Liu et al., "Numerical simulation of powder transport behavior in laser cladding with coaxial powder feeding," Sci. China Physics, Mech. Astron., vol. 58, no. 10, 2015

[22]   S. Y. Wen, Y. C. Shin, J. Y. Murthy, and P. E. Sojka, "Modeling of coaxial powder flow for the laser direct deposition process," Int. J. Heat Mass Transf., vol. 52, no. 25–26, pp. 5867–5877, 2009

[23]   A. Da Silva, J. Volpp, J. Frostevarg, and A. F. H. Kaplan, "Acceleration of metal drops in a laser beam," Appl. Phys. A Mater. Sci. Process., vol. 127, no. 1, pp. 1–13, 2021

[24]   D. V. Sergachev, O. B. Kovalev, G. N. Grachev, A. L. Smirnov, and P. A. Pinaev, "Diagnostics of powder particle parameters under laser radiation in direct material deposition," Opt. Laser Technol., vol. 121, no. August 2019, p. 105842, 2020

[25]   D. V. Sergachev, A. A. Mikhal'chenko, O. B. Kovalev, V. I. Kuz'min, G. N. Grachev, and P. A. Pinaev, "Laser-optic measurements of velocity of particles in the powder stream at coaxial laser cladding," Phys. Procedia, vol. 56, no. C, pp. 193–203, 2014

[26]   I. P. Gulyaev, O. B. Kovalev, P. A. Pinaev, and G. N. Grachev, "Optical diagnostics of radiation interaction with the powder stream laterally transported during laser cladding," Opt. Lasers Eng., vol. 126, no. June 2019, p. 105877, 2020

[27]   S. J. Wolff, H. Wu, N. Parab, C. Zhao, K. F. Ehmann, and T. Sun, "In - situ high-speed X-ray imaging of piezo-driven directed energy deposition additive manufacturing," Sci. Rep., no. June 2018, pp. 1–14, 2019

[28]   Webster, S., Wolff, S., Bennett, J., Sun, T., Cao, J., & Ehmann, K. "Porosity formation and meltpool geometry analysis using high-speed, in situ imaging of directed energy deposition," Microscopy and Microanalysis, 25(S2), 2556-2557, 2019

[29]   C. Kenel et al., "In situ investigation of phase transformations in Ti-6Al-4V under additive manufacturing conditions combining laser melting and high-speed micro-X-ray diffraction," Sci. Rep., vol. 7, no. 1, pp. 1–10, 2017

[30]   M. Pasandideh-Fard and J. Mostaghimi, "On the spreading and solidification of molten particles in a plasma spray process effect of thermal contact resistance," Plasma Chem. Plasma Process., vol. 16, no. 1, pp. S83–S98, 1995

[31]   K. Shinoda, T. Koseki, and T. Yoshida, "Influence of impact parameters of zirconia droplets on splat formation and morphology in plasma spraying," J. Appl. Phys., vol. 100, no. 7, 2006

[32]   M. Vardelle, A. Vardelle, A. C. Leger, P. Fauchais, and D. Gobin, "Influence of particle parameters at the impact on splat formation and solidification in plasma spraying processes," J. Therm. Spray Technol., vol. 4, no. 1, pp. 50–58, 1995

[33]   W. Xibao and L. Hua, "Metal powder thermal behaviour during the plasma transferred-arc surfacing process," Surf. Coatings Technol., vol. 106, no. 2–3, pp. 156–161, 1998

[34]   D. J. Branagan, M. C. Marshall, and B. E. Meacham, "High toughness high hardness iron-based PTAW weld materials," Mater. Sci. Eng. A vol. 428, no. 1–2, pp. 116–123, 2006

[35]   Z. Huang, Q. Hou, and P. Wang, "Microstructure and properties of Cr3C2-modified nickel-based alloy coating deposited by plasma transferred arc process," Surf. Coatings Technol., vol. 202, no. 13, pp. 2993–2999, 2008

[36]   A. Gatto, E. Bassoli, and M. Fornari, "Plasma Transferred Arc deposition of powdered high performances alloys: Process parameters optimization as a function of alloy and geometrical configuration," Surf. Coatings Technol., vol. 187, no. 2–3, pp. 265–271, 2004

[37]   L. Łatka and P. Biskup, "Development in PTA Surface Modifications – A Review," Adv. Mater. Sci., vol. 20, no. 2, pp. 39–53, 2020

[38]   J. G. Mercado Rojas, T. Wolfe, B. A. Fleck, and A. J. Qureshi, "Plasma transferred arc additive manufacturing of Nickel-metal matrix composites," Manuf. Lett., vol. 18, pp. 31–34, 2018

[39]   A. Zikin, I. Hussainova, C. Katsich, E. Badisch, and C. Tomastik, "Advanced chromium carbide-based hardfacings," Surf. Coatings Technol., vol. 206, no. 19–20, pp. 4270–4278, 2012

[40]   Oerlikon Metco. Material Product Data Sheet Monocrystalline Tungsten Carbide / Nickel Chromium Boron Silicon Powder for Plasma Transferred Arc (PTA). Tech. rep. Oerlikon Metco, pp. 1–4, 2019. URL: https://www.oerlikon. com/ecomaXL/files/metco/oerlikon DSM-0246.0 PlasmaDur MTC NiCrBSi. pdf%5C&download=0

[41]   D. B. Goldman, "Vignette and exposure calibration and compensation," IEEE Trans. Pattern Anal. Mach. Intell., vol. 32, no. 12, pp. 2276–2288, 2010

[42]   H. Q. Sun and Y. J. Luo, "Adaptive watershed segmentation of binary particle image," J. Microsc., vol. 233, no. 2, pp. 326–330, 2009

[43]   Liew, K. H., Urip, E., Yang, S. L., & Marek, C. J. "An Interactive Microsoft® Excel Program for Tracking a Single Evaporating Droplet in Crossflow," NASA, NASA/TM—2004-212910, 2004

[44]   X. Liu, X. Zhang, and J. Min, "Maximum spreading of droplets impacting spherical surfaces," Phys. Fluids, vol. 31, no. 9, 2019

[45]   Proulx. P, "Plasma-particle heat transfer", Springer International Publishing AG, 2018

[46]   M. Y. Leong, V. G. McDonell, and G. S. Samuelsen, "Mixing of an Airblast-Atomized Fuel spray injected into a crossflow of air," NASA/Cr-2000-210467, 2000, URL: http://www.sti.nasa.gov

[47]   K. Bobzin and M. Öte, "Modeling Plasma–Particle Interaction in Multi-Arc Plasma Spraying," J. Therm. Spray Technol., vol. 26, no. 3, pp. 279–291, 2017

[48]   Pasandideh-Fard, M., et al. "Deposition of tin droplets on a steel plate: simulations and experiments," International Journal of Heat and Mass Transfer, vol. 41, no19, 2929-2945,1998

[49]   S. Chandra and C. T. Avedisian, "On the collision of a droplet with a solid surface," Proc. R. Soc. A Math. Phys. Eng. Sci., vol. 432, no. 1884, pp. 13–41, 1991

[50]   A. Ahmed, A. J. Qureshi, B. A. Fleck, and P. R. Waghmare, "Effects of magnetic field on the spreading dynamics of an impinging ferrofluid droplet," J. Colloid Interface Sci., vol. 532, pp. 309–320, 2018

[51]   R. Bhola and S. Chandra, "Parameters controlling solidification of molten wax droplets falling on a solid surface," J. Mater. Sci., vol. 34, no. 19, pp. 4883–4894, 1999

[52]   Mills A.F., "Heat Transfer", Irwin Press: Boston, 1992

[53]   F. Ben Ettouil, O. Mazhorova, B. Pateyron, H. Ageorges, M. El Ganaoui, and P. Fauchais, "Predicting dynamic and thermal histories of agglomerated particles injected within a d.c. plasma jet," Surf. Coatings Technol., vol. 202, no. 18, pp. 4491–4495, 2008

[54]   Mostaghimi, J., and S. Chandra. "Droplet impact and solidification in plasma spraying." Handbook of Thermal Science and Engineering, 2967-3008, 2018

[55]   O. B. Kovalev, I. O. Kovaleva, and I. Y. Smurov, "Numerical investigation of gas-disperse jet flows created by coaxial nozzles during the laser direct material deposition," J. Mater. Process. Technol., vol. 249, pp. 118–127, 2017

[56]   Cedelle, J., et al. "Study of droplet behaviour at impact in plasma spraying." High Temperature Material Processes: An International Quarterly of High-Technology Plasma Processes 8, no. 3, 2004

[57]   S. Fathi, P. Dickens, and F. Fouchal, "Regimes of droplet train impact on a moving surface in an additive manufacturing process," J. Mater. Process. Technol., vol. 210, no. 3, pp. 550–559, 2010

[58]   J. Shimizu, E. Ohmura, Y. Kobayashi, S. Kiyoshima, and H. Eda, "Molecular dynamics simulation of flattening process of a high-temperature, high-speed droplet - Influence of impact parameters," J. Therm. Spray Technol., vol. 16, no. 5–6, pp. 722–728, 2007

[59]   Y. Zhang, S. Matthews, A. T. T. Tran, and M. Hyland, "Effects of interfacial heat transfer, surface tension and contact angle on the formation of plasma-sprayed droplets through simulation study," Surf. Coatings Technol., vol. 307, pp. 807–816, 2016

[60]   S. Schiaffino and A. A. Sonin, "Molten droplet deposition and solidification at low Weber numbers," Phys. Fluids, vol. 9, no. 11, pp. 3172–3187, 1997

[61]   A. Ahmed, B. A. Fleck, and P. R. Waghmare, "Maximum spreading of a ferrofluid droplet under the effect of magnetic field," Phys. Fluids, vol. 30, no. 7, 2018

[62]   H. Tabbara and S. Gu, "Modelling of impingement phenomena for molten metallic droplets with low to high velocities," Int. J. Heat Mass Transf., vol. 55, no. 7–8, pp. 2081–2086, 2012

4 Conclusion and Future work

4.1 Summary

In this research, the PTA-AM process parameter's influence on the bead quality is investigated using in-situ image processing methodology. The dependency of bead quality on the PTA-AM's process parameters is signified using analysis of variance (ANOVA) and statistical t-test. Furthermore, powder flow behaviour under the plasma arc region is investigated. Based on this assessment, a parametric study has been conducted to predict the spreading and solidification dynamics during molten particles' impingement on the substrate.

Chapter 2 discusses the effects of PTA-AM-based process parameters such as stand-off distance (SOD), powder flow (powder particle count) and plasma arc current on the bead quality and its geometry variation. The bulleted summary of each this chapter is as follows:

- It is inspected that the stable deposition of the bead depends on the SOD value. The variation in SOD value shifts the merging point of the powder flow streams under the plasma arc region, which could be responsible for the deviation in bead deposition. Present observation depicted that at the SOD of 7 mm, the powder streams from two separate nozzles correctly merged at the interaction point in the plasma arc region. At the SOD of 9.44 mm, two powder streams formed the saddle-shaped powder distribution under the plasma arc region, significantly impacting the quality of bead deposition. The validation of these results has been done with the work of Rojas et al [56], where the optimized SOD is determined as 7 mm, which prints the stable bead with minimum deviation.

- As it is investigated that powder flow distribution influences the stability of the bead, this study examined the uniformity of the powder stream distribution for different sample experiments conducted at a constant powder flow rate. The results showed that the powder stream distribution is uniform for all the sample experiments operated under the 60 A and 100 A, and it defines that the PTA-AM system is less susceptible to external disturbances.

- Using image analysis on in-situ high-speed images, this study extracted the information of total powder particle count and the bead height. The degree of dependency of bead height variation on total powder particle count is determined using the linear regression model. The ANOVA and statistical t-test have confirmed the significance of the correlation between total particle count and bead height variation.

- This study also examined the effect of plasma arc current on the bead geometry (height and width). It is determined that as the plasma arc current increased by 40% (60A to 100 A), the mean bead width is increased by 85%, and the mean bead height is decreased by 24%. It is also noticed that bead width is more stable with minimum deviation for the plasma current of 60 A as compared to 100 A.

In Chapter 3, we investigated the powder flow behaviour, one of the critical parameters in the PTA-AM process that governs the quality of bead deposition, which eventually decides the quality of the 3D printed part. The bulleted summary of each this chapter is as follows:

- This study determined the deviations in particles trajectories and velocities due to variation in the plasma arc since these in-flight particle dynamics are responsible for their phase transformation during travelling in the plasma arc region. The phase of particles (fully or partially melted) and their metallurgical bond with the molten pool decide the geometrical

and dimensional properties of the build. Also, it is studied that the surface finish and geometry of the bead layer fluctuate due to the impact dynamics of the molten droplets, which depend not only on the plasma arc current but also on the particle location at the nozzle exit.

- Based on the data of powder motion dynamics, this work conducted a parametric study, where the maximum spreading of a molten droplet and its degree of reduction under the solidification effect is predicted. It has been concluded that molten droplets could flatten at least 1.5 to 2.1 times their original diameter of molten drop.

- The parametric effect of equilibrium contact angle on the maximum spreading of the droplet has evaluated that for the $\theta_e < 120°$, the substrate wettability properties (θ_e) play a considerable role in changing the molten droplet's spreading diameter. However, as the $\theta_e > 120°$, it showed that substrate wettability has a minor impact on spreading phenomena irrespective of plasma current variation.

- At last, this study has provided the critical solidification value (α), which decides whether the solidification effect arrests the molten droplet from spreading.

4.2 Future work

The main objective of this research work was to develop in-situ image processing techniques for determining the correlations between PTA-AM's processing parameters and bead quality and its geometry. With this agenda, as mentioned in Chapters 2 and 3, the in-situ image processing methodologies have been developed, which successfully delivered the objectives. This work can be further extended for the in-process optimization of processing parameters and to improve the bead quality. The following points are suggested for future work.

- The bead quality deviation is critical, and it would be efficient to detect such an error in real-time so that the process parameter can be adjusted to compensate for an error and improve the bead quality in-process. For this purpose, a closed-loop feedback control system can be developed based on sensors, which detects the deviation from the in-situ images and improve it by adjusting the processing parameters in real-time.

- As worktable travel speed varies, the amount of material deposited per unit length also varies, changing the bead geometry dramatically. In future work, the dependency of the bead geometry on worktable speed can be developed using the proposed in-situ image processing technique.

- This study uses the 2D image streams for powder particle measurements. Since the powder flow distribution is 3D, future work could develop a powder flow analytical model based on 2D images to measure powder utilization efficiency in the molten pool.

- The plasma arc velocity is Gaussian distributed with arc radial distance; however, this study uses the effect of the max-min range of arc velocity on particle motion dynamics. In future work, the Gaussian distribution of powder flow can be included in the particle trajectory model for the precise measurement of individual particles' trajectories and velocities.

- The parametric study of molten droplet spreading, and solidification can be further validated experimentally by analyzing the high-speed images of droplet impact dynamics. With this information, the analytical model can be developed to predict the quality and geometry of the final part.

Bibliography

Aggarwal, A., Chouhan, A., Patel, S., Yadav, D. K., Kumar, A., Vinod, A. R., Prashanth, K. G., & Gurao, N. P. (2020). Role of impinging powder particles on melt pool hydrodynamics, thermal behaviour and microstructure in laser-assisted DED process: A particle-scale DEM – CFD – CA approach. International Journal of Heat and Mass Transfer, 158, 119989. https://doi.org/10.1016/j.ijheatmasstransfer.2020.119989

Akmaliyah, M. (2013). Development and Characterization of Additive Manufacturing of Superalloy Hastelloy X Using a Cost-Effective TIG Technique. Journal of Chemical Information and Modeling, 53(9), 1689–1699.

A. Alberti, B. M. P. Bueno, and A. S. C. M. D. Oliveira, (2016) Additive manufacturing using plasma transferred arc, Int J Adv Manuf. Technol., pp. 1861–1871, doi: 10.1007/s00170-015-7697-7.

Anandkumar, R., Almeida, A., Vilar, R., Ocelík, V., & De Hosson, J. T. M. (2009). Influence of powder particle injection velocity on the microstructure of Al-12Si/SiCp coatings produced by laser cladding. Surface and Coatings Technology, 204(3), 285–290. https://doi.org/10.1016/j.surfcoat.2009.07.025

Arcam Electron beam. URL:http://www.arcam.com/ technology/products/arcam-q10

ASTM International. (2012). F2792-12a: standard terminology for additive manufacturing technologies. Procedia Eng,63, 4–11.

ASTM International. (2015). ASTM52900-15 standard terminology for additive manufacturing—general principles—terminology, West Conshohocken, PA:ASTM International, https://doi.org/10.1520/ISOASTM52900-15.

Babak Kianian. (2017). 3D Printing and Additive Manufacturing State of the Industry, Annual Worldwide Progress Report. URL: https://wohlersassociates.com/2017report.htm

Bhola, R., & Chandra, S. (1999). Parameters controlling solidification of molten wax droplets falling on a solid surface. Journal of Materials Science, 34(19), 4883–4894. https://doi.org/10.1023/A:1004680315199

Bhuvanesh Kumar, M., & Sathiya, P. (2021). Methods and materials for additive manufacturing: A critical review on advancements and challenges. Thin-Walled Structures, 159(July 2020), 107228. https://doi.org/10.1016/j.tws.2020.107228

Bikas, H., Stavropoulos, P., & Chryssolouris, G. (2016). Additive manufacturing methods and modelling approach: A critical review. International Journal of Advanced Manufacturing Technology, 83(1–4), 389–405. https://doi.org/10.1007/s00170-015-7576-2

Branagan, D. J., Marshall, M. C., & Meacham, B. E. (2006). High toughness high hardness iron-based PTAW weld materials. Materials Science and Engineering A, 428(1–2), 116–123. https://doi.org/10.1016/j.msea.2006.04.089

Brett, T., Wolfe, B., Brett, T., & Wolfe, B. (2010). University of Alberta Homogeneity of Metal Matrix Composites Deposited by Plasma Transferred Arc by Department of Chemical and Materials Engineering Examining Committee Dr . Hani Henein, Chemical and Materials Engineering. 364. https://doi.org/10.7939/R3K64Q

Chang, R., Emami, K., Wu, H., & Sun, W. (2010). Biofabrication of a three-dimensional liver micro-organ as an in vitro drug metabolism model. Biofabrication, 2(4). https://doi.org/10.1088/1758-5082/2/4/045004

Comb, J. W., Priedeman, W. R., & Turley, P. W. (1994). FDM Technology Process Improvements. Proceedings of Solid Freeform Fabrication Symposium, 42–49.

Da Silva, A., Volpp, J., Frostevarg, J., & Kaplan, A. F. H. (2021). Acceleration of metal drops in a laser beam. Applied Physics A: Materials Science and Processing, 127(1), 1–13. https://doi.org/10.1007/s00339-020-04177-y

Dass, A., & Moridi, A. (2019). State of the Art in Directed Energy Deposition : From Additive Manufacturing to Materials Design, Coatings, 9(July), p.418. 1–26. https://doi.org/10.3390/coatings9070418.

de Oliveira, U., Ocelík, V., & De Hosson, J. T. M. (2005). Analysis of coaxial laser cladding processing conditions. Surface and Coatings Technology, 197(2–3), 127–136. https://doi.org/10.1016/j.surfcoat.2004.06.029

DebRoy, T., Wei, H. L., Zuback, J. S., Mukherjee, T., Elmer, J. W., Milewski, J. O., Beese, A. M., Wilson-Heid, A., De, A., & Zhang, W. (2018). Additive manufacturing of metallic components – Process, structure and properties. Progress in Materials Science, 92, 112–224. https://doi.org/10.1016/j.pmatsci.2017.10.001

Diaz, V. V., Dutra, J. C., & D'Oliveira, A. S. C. M. (2012). Hardfacing by plasma transfer arc process. Welding International, 26(2), 87–95. https://doi.org/10.1080/09507116.2010.527486

Dinovitzer, M., Chen, X., Laliberte, J., Huang, X., & Frei, H. (2019). Effect of wire and arc additive manufacturing (WAAM) process parameters on bead geometry and microstructure. Additive Manufacturing, 26(October 2018), 138–146. https://doi.org/10.1016/j.addma.2018.12.013

D. S. Engstrom, Binder jetting, Loughbrgh. Univ., 2012. URL:https://www.lboro.ac.uk/research/amrg/about/the7categoriesofadditivemanufacturing/binderjetting/

Fayazfar, H., Salarian, M., Rogalsky, A., Sarker, D., Russo, P., Paserin, V., & Toyserkani, E. (2018). A critical review of powder-based additive manufacturing of ferrous alloys: Process

parameters, microstructure and mechanical properties. Materials and Design, 144, 98–128. https://doi.org/10.1016/j.matdes.2018.02.018

Fayazfar, H., Salarian, M., Rogalsky, A., Sarker, D., Russo, P., Paserin, V., & Toyserkani, E. (2018b). A critical review of powder-based additive manufacturing of ferrous alloys: Process parameters, microstructure and mechanical properties. Materials and Design, 144, 98–128. https://doi.org/10.1016/j.matdes.2018.02.018

Frazier, W. E. (2014). Metal additive manufacturing: A review. Journal of Materials Engineering and Performance, 23(6), 1917–1928. https://doi.org/10.1007/s11665-014-0958-z

Frenk, A., Vandyoussefi, M., Wagniere, J. D., Zryd, A., & Kurz, W. (1997). Analysis of the laser-cladding process for stellite on steel. Metallurgical and Materials Transactions B: Process Metallurgy and Materials Processing Science, 28(3), 501–508. https://doi.org/10.1007/s11663-997-0117-0

F. Peng, B. D. Vogt, and M. Cakmak, "Complex flow and temperature history during melt extrusion in material extrusion additive manufacturing," Addit. Manuf., vol. 22, no. August 2017, pp. 197–206, 2018, doi: 10.1016/j.addma.2018.05.015

Gao, W., Zhang, Y., Ramanujan, D., Ramani, K., Chen, Y., Williams, C. B., Wang, C. C. L., Shin, Y. C., Zhang, S., & Zavattieri, P. D. (2015). The status, challenges, and future of additive manufacturing in engineering. CAD Computer-Aided Design, 69, 65–89. https://doi.org/10.1016/j.cad.2015.04.001

Garcia-Gonzalez, D., Garzon-Hernandez, S., & Arias, A. (2018). A new constitutive model for polymeric matrices: Application to biomedical materials. Composites Part B: Engineering, 139(December 2017), 117–129. https://doi.org/10.1016/j.compositesb.2017.11.045

Gartner. (2014). Hype Cycle for 3D Printing.

Gatto, A., Bassoli, E., & Fornari, M. (2004). Plasma Transferred Arc deposition of powdered high performances alloys: Process parameters optimization as a function of alloy and geometrical configuration. Surface and Coatings Technology, 187(2–3), 265–271. https://doi.org/10.1016/j.surfcoat.2004.02.013

Gibson, I., Rosen, D., & Stucker, B. (2015). Directed Energy Deposition Processes. In: Additive Manufacturing Technologies, pp. 245-268, Springer, New York, NY.

Gokuldoss, P. K., Kolla, S., & Eckert, J. (2017). Additive manufacturing processes: Selective laser melting, electron beam melting and binder jetting-selection guidelines. Materials, 10(6). https://doi.org/10.3390/ma10060672

Govekar, E., Jeromen, A., Kuznetsov, A., Kotar, M., & Kondo, M. (2018). Annular laser beam-based direct metal deposition. Procedia CIRP, 74, 222–227. https://doi.org/10.1016/j.procir.2018.08.099

Griffith, M. L., Harwell, L. D., Romero, J., Schlienger, E., Atwood, C. L., & Smugeresky, J. E. (1997). Multi-material processing by LENS. Solid Freeform Fabrication Symposium, 387–393. http://sffsymposium.engr.utexas.edu/Manuscripts/1997/1997-45-Griffith.pdf

Gulyaev, I. P., Kovalev, O. B., Pinaev, P. A., & Grachev, G. N. (2020). Optical diagnostics of radiation interaction with the powder stream laterally transported during laser cladding. Optics and Lasers in Engineering, 126(June 2019), https://doi.org/10.1016/j.optlaseng.2019.105877

Guo, N., & Leu, M. C. (2013). Additive manufacturing: Technology, applications and research needs. Frontiers of Mechanical Engineering, 8(3), 215–243. https://doi.org/10.1007/s11465-013-0248-8

Harrysson, O. L. A., Cansizoglu, O., Marcellin-Little, D. J., Cormier, D. R., & West, H. A. (2008). Direct metal fabrication of titanium implants with tailored materials and mechanical properties using electron beam melting technology. Materials Science and Engineering C, 28(3), 366–373. https://doi.org/10.1016/j.msec.2007.04.022

Herderick, E. (2011). Additive manufacturing of metals: A review. Materials Science and Technology Conference and Exhibition 2011, MS and T'11, 2(176252), 1413–1425.

Herzog, D., Seyda, V., Wycisk, E., & Emmelmann, C. (2016). Additive manufacturing of metals. Acta Materialia, 117, 371–392. https://doi.org/10.1016/j.actamat.2016.07.019

Huang, S. H., Liu, P., Mokasdar, A., & Hou, L. (2013). Additive manufacturing and its societal impact: A literature review. International Journal of Advanced Manufacturing Technology, 67(5–8), 1191–1203. https://doi.org/10.1007/s00170-012-4558-5

Huang, Z., Hou, Q., & Wang, P. (2008). Microstructure and properties of Cr3C2-modified nickel-based alloy coating deposited by plasma transferred arc process. Surface and Coatings Technology, 202(13), 2993–2999. https://doi.org/10.1016/j.surfcoat.2007.10.033

Hull, C. W. (1984). Apparatus for Production of Three-Dimensional Objects By Stereo Thography. Patent, 19, 16.

Ibrahim, S. (2020). Plasma Transferred Arc Additive Manufacturing Using the 17-4 Precipitation Hardened Stainless Steel, University of Alberta.

Jafari, D., Vaneker, T. H. J., & Gibson, I. (2021). Wire and arc additive manufacturing: Opportunities and challenges to control the quality and accuracy of manufactured parts. Materials and Design, 202, 109471. https://doi.org/10.1016/j.matdes.2021.109471

Jose Guadalupe Mercado Rojas. (2021). Design and system identification for a plasma transferred arc additive manufacturing technology. The University of Alberta.

Kenel, C., Grolimund, D., Li, X., Panepucci, E., Samson, V. A., Sanchez, D. F., Marone, F., & Leinenbach, C. (2017). In situ investigation of phase transformations in Ti-6Al-4V under additive

manufacturing conditions combining laser melting and high-speed micro-X-ray diffraction. Scientific Reports, 7(1), 1–10. https://doi.org/10.1038/s41598-017-16760-0

Klingelnberg, J. (2016). Manufacturing Process. In Bevel Gear. Elsevier Inc. https://doi.org/10.1007/978-3-662-43893-0_6

Körner, C. (2016). Additive manufacturing of metallic components by selective electron beam melting - A review. International Materials Reviews, 61(5), 361–377. https://doi.org/10.1080/09506608.2016.1176289

Kumar, A., Mandal, S., Barui, S., Vasireddi, R., Gbureck, U., Galinsky, M., & Basu, B. (2016a). Low-temperature additive manufacturing of three-dimensional scaffolds for bone tissue engineering applications: Processing related challenges and property assessment. Materials Science and Engineering R: Reports, 103, 1–39. https://doi.org/10.1016/j.mser.2016.01.001

Kumar, A., Mandal, S., Barui, S., Vasireddi, R., Gbureck, U., Galinsky, M., & Basu, B. (2016b). Low-temperature additive manufacturing of three-dimensional scaffolds for bone tissue engineering applications: Processing related challenges and property assessment. Materials Science and Engineering R: Reports, 103, 1–39. https://doi.org/10.1016/j.mser.2016.01.001

Lakshminarayanan, A. K., Balasubramanian, V., Varahamoorthy, R., & Babu, S. (2008). Predicting the dilution of plasma transferred arc hardfacing of stellite on carbon steel using response surface methodology. Metals and Materials International, 14(6), 779–789. https://doi.org/10.3365/met.mat.2008.12.779

Łatka, L., & Biskup, P. (2020). Development in PTA Surface Modifications – A Review. Advances in Materials Science, 20(2), 39–53. https://doi.org/10.2478/adms-2020-0009

Lee, J. Y., Nagalingam, A. P., & Yeo, S. H. (2021a). A review on the state-of-the-art of surface finishing processes and related ISO/ASTM standards for metal additive manufactured components. Virtual and Physical Prototyping, 16(1), 68–96. https://doi.org/10.1080/17452759.2020.1830346

Lee, J. Y., Nagalingam, A. P., & Yeo, S. H. (2021b). A review on the state-of-the-art of surface finishing processes and related ISO/ASTM standards for metal additive manufactured components. Virtual and Physical Prototyping, 16(1), 68–96. https://doi.org/10.1080/17452759.2020.1830346

Liu, H., He, X. L., Yu, G., Wang, Z. Bin, Li, S. X., Zheng, C. Y., & Ning, W. J. (2015). Numerical simulation of powder transport behaviour in laser cladding with coaxial powder feeding. Science China: Physics, Mechanics and Astronomy, 58(10). https://doi.org/10.1007/s11433-015-5705-4

Liu, S., Zhang, Y., & Kovacevic, R. (2015). Numerical Simulation and Experimental Study of Powder Flow Distribution in High Power Direct Diode Laser Cladding Process. 199–218. https://doi.org/10.1007/s40516-015-0015-2

Lott, P., Schleifenbaum, H., Meiners, W., Wissenbach, K., Hinke, C., & Bültmann, J. (2011). Design of an optical system for the in situ process monitoring of Selective Laser Melting (SLM). Physics Procedia, 12(PART 1), 683–690. https://doi.org/10.1016/j.phpro.2011.03.085

Manyika, J., Chui, M., Bughin, J., Dobbs, R., Bisson, P., & Marrs, A. (2013). Disruptive technologies: Advances that will transform life, business, and the global economy. McKinsey Global Institute, 180, 17–21.

Mercado Rivera, F. J., & Rojas Arciniegas, A. J. (2020). Additive manufacturing methods: techniques, materials, and closed-loop control applications. International Journal of Advanced Manufacturing Technology, 109(1–2), 17–31. https://doi.org/10.1007/s00170-020-05663-6

Mercado Rojas, J. G., Wolfe, T., Fleck, B. A., & Qureshi, A. J. (2018). Plasma transferred arc additive manufacturing of Nickel-metal matrix composites. Manufacturing Letters, 18, 31–34. https://doi.org/10.1016/j.mfglet.2018.10.001

Moghazi, S. N. El, Wolfe, T., Ivey, D. G., & Henein, H. (2020). Plasma transfer arc additive manufacturing of 17-4 PH : assessment of defects. 2301–2313.

Mueller, B., & Kochan, D. (1999). Laminated object manufacturing for rapid tooling and patternmaking in the foundry industry. Computers in Industry, 39(1), 47–53. https://doi.org/10.1016/S0166-3615(98)00127-4

Najmon, J. C., Raeisi, S., & Tovar, A. (2019). Review of additive manufacturing technologies and applications in the aerospace industry. In Additive Manufacturing for the Aerospace Industry. Elsevier Inc. https://doi.org/10.1016/B978-0-12-814062-8.00002-9

Ngo, T. D., Kashani, A., Imbalzano, G., Nguyen, K. T. Q., & Hui, D. (2018). Additive manufacturing (3D printing): A review of materials, methods, applications and challenges. Composites Part B: Engineering, 143(December 2017), 172–196. https://doi.org/10.1016/j.compositesb.2018.02.012

Optomec. URL:http://www.optomec.com/1/6 scale mixing nozzle for gas turbine exhaust for Bell helicopter

Pasandideh-Fard, M., & Mostaghimi, J. (1995). On the spreading and solidification of molten particles in a plasma spray process effect of thermal contact resistance. Plasma Chemistry and Plasma Processing, 16(1), S83–S98. https://doi.org/10.1007/BF01512629

Parupelli, SantoshKumar, and Salil Desai. "A comprehensive review of additive manufacturing (3d printing): processes, applications and future potential." American journal of applied sciences 16, no. 8, 2019

Peltola, S. M., Melchels, F. P. W., Grijpma, D. W., & Kellomäki, M. (2008). A review of rapid prototyping techniques for tissue engineering purposes. Annals of Medicine, 40(4), 268–280. https://doi.org/10.1080/07853890701881788

Peng, F., Vogt, B. D., & Cakmak, M. (2018). Complex flow and temperature history during melt extrusion in material extrusion additive manufacturing. Additive Manufacturing, 22(August 2017), 197–206. https://doi.org/10.1016/j.addma.2018.05.015

Peng, T., Kellens, K., Tang, R., Chen, C., & Chen, G. (2018). Sustainability of additive manufacturing: An overview on its energy demand and environmental impact. Additive Manufacturing, 21(June 2017), 694–704. https://doi.org/10.1016/j.addma.2018.04.022

Perez-Soriano, E. M., Ariza, E., Arevalo, C., Montealegre-Melendez, I., Kitzmantel, M., & Neubauer, E. (2020). Processing by additive manufacturing based on plasma transferred arc of Hastelloy in air and argon atmosphere. Metals, 10(2). https://doi.org/10.3390/met10020200

Pettersson, V. (2018). Study of the effect of process parameters in laser blown powder with superalloys: Varying laser power and scanning speed, analyzing material properties, MSc thesis. Department of Mechanical Engineering, Karlstads University, 2018, p. 80. URL:https://www.diva-portal.org/smash/get/diva2:1238212/FULLTEXT01.pdf

Pham, D. T., & Ji, C. (2000). Design for stereolithography. Proceedings of the Institution of Mechanical Engineers, Part C: Journal of Mechanical Engineering, 214(5), 635–640. https://doi.org/10.1243/0954406001523650

Prakash, K. S., Nancharaih, T., & Rao, V. V. S. (2018). Additive Manufacturing Techniques in Manufacturing -An Overview. Materials Today: Proceedings, 5(2), 3873–3882. https://doi.org/10.1016/j.matpr.2017.11.642

Rodrigues, T. A., Duarte, V., Miranda, R. M., Santos, T. G., & Oliveira, J. P. (2019). Current status and perspectives on wire and arc additive manufacturing (WAAM). Materials, 12(7). https://doi.org/10.3390/ma12071121

Rodriguez, N., Vázquez, L., Huarte, I., Arruti, E., Tabernero, I., & Alvarez, P. (2018). Wire and arc additive manufacturing: a comparison between CMT and TopTIG processes applied to stainless steel. Welding in the World, 62(5), 1083–1096. https://doi.org/10.1007/s40194-018-0606-6

Rojas, J. G. M., Ghasri-Khouzani, M., Wolfe, T., Fleck, B., Henein, H., & Qureshi, A. J. (2021). Preliminary geometrical and microstructural characterization of WC-reinforced NiCrBSi matrix composites fabricated by plasma transferred arc additive manufacturing through Taguchi-based experimentation. The International Journal of Advanced Manufacturing Technology. https://doi.org/10.1007/s00170-020-06388-2

Saboori, A., Aversa, A., Marchese, G., Biamino, S., Lombardi, M., & Fino, P. (2019). Application of directed energy deposition-based additive manufacturing in repair. Applied Sciences (Switzerland), 9(16). https://doi.org/10.3390/app9163316

Sachs, E., Cima, M., Williams, P., Brancazio, D., & Cornie, J. (1992). Three-dimensional printing: Rapid tooling and prototypes directly from a CAD model. Journal of Manufacturing Science and Engineering, Transactions of the ASME, 114(4), 481–488. https://doi.org/10.1115/1.2900701

Schopphoven, T., Pirch, N., Mann, S., Poprawe, R., Häfner, C. L., & Schleifenbaum, J. H. (2020). Statistical/numerical model of the powder-gas jet for extreme high-speed laser material deposition. Coatings, 10(4). https://doi.org/10.3390/coatings10040416

Sergachev, D. V., Kovalev, O. B., Grachev, G. N., Smirnov, A. L., & Pinaev, P. A. (2020). Diagnostics of powder particle parameters under laser radiation indirect material deposition. Optics and Laser Technology, 121(August 2019), 105842. https://doi.org/10.1016/j.optlastec.2019.105842

Sergachev, D. V., Mikhal'chenko, A. A., Kovalev, O. B., Kuz'min, V. I., Grachev, G. N., & Pinaev, P. A. (2014). Laser-optic measurements of the velocity of particles in the powder stream at coaxial laser cladding. Physics Procedia, 56(C), 193–203. https://doi.org/10.1016/j.phpro.2014.08.163

Sheydaeian, E., & Toyserkani, E. (2018). A new approach for fabrication of titanium-titanium boride periodic composite via additive manufacturing and pressure-less sintering. Composites Part B: Engineering, 138(November 2017), 140–148. https://doi.org/10.1016/j.compositesb.2017.11.035

Shinoda, K., Koseki, T., & Yoshida, T. (2006). Influence of impact parameters of zirconia droplets on splat formation and morphology in plasma spraying. Journal of Applied Physics, 100(7). https://doi.org/10.1063/1.2355446

Singh, A., Kapil, S., & Das, M. (2020). A comprehensive review of the methods and mechanisms for powder feedstock handling in directed energy deposition. Additive Manufacturing, 35(May), 101388. https://doi.org/10.1016/j.addma.2020.101388

T. Wohlers. (2016). Wohlers Report 2016: Executive Summary, Wohlers Associates Inc., Fort Collins, 2016.

Tabernero, I., Lamikiz, A., Martínez, S., Ukar, E., & López De Lacalle, L. N. (2012). Modelling of energy attenuation due to powder flow-laser beam interaction during laser cladding process. Journal of Materials Processing Technology, 212(2), 516–522. https://doi.org/10.1016/j.jmatprotec.2011.10.019

Taminger, K., & Hafley, R. (2003). Electron beam freeform fabrication: a rapid metal deposition process. Proceedings of the 3rd Annual Automotive Composites Conference, January 2003, 9–10. http://www.ntrs.nasa.gov/archive/nasa/casi.ntrs.nasa.gov/20040042496_2004036110.pdf

Tan, H., Zhang, F., Wen, R., Chen, J., & Huang, W. (2012). Experiment study of powder flow feed behaviour of laser solid forming. Optics and Lasers in Engineering, 50(3), 391–398. https://doi.org/10.1016/j.optlaseng.2011.10.017

Tchikango Siagam, A., Brenner, G., Giese, P., & Wesling, V. (2008). Numerical and experimental study of particle motion in plasma arc welding. Fluid Dynamics and Materials Processing, 4(2), 77–83. https://doi.org/10.3970/fdmp.2008.004.077

Terry T Wohlers; Tim Caffrey. (2014). 3D printing and additive manufacturing state of the industry annual worldwide progress report. Wohlers Report.

Toyserkani, E., Khajepour, A., & Corbin, S. (2004). 3-D finite element modelling of laser cladding by powder injection: Effects of laser pulse shaping on the process. Optics and Lasers in Engineering, 41(6), 849–867. https://doi.org/10.1016/S0143-8166(03)00063-0

Vandenbroucke, B., & Kruth, J. P. (2006). Selective laser melting of biocompatible metals for rapid manufacturing of medical parts. 17th Solid Freeform Fabrication Symposium, SFF 2006, 148–159.

Vardelle, M., Vardelle, A., Leger, A. C., Fauchais, P., & Gobin, D. (1995). Influence of particle parameters at the impact on splat formation and solidification in plasma spraying processes. Journal of Thermal Spray Technology, 4(1), 50–58. https://doi.org/10.1007/BF02648528

Wang, H., Jiang, W., Valant, M., & Kovacevic, R. (2003). Microplasma powder deposition as a new solid freeform fabrication process. Proceedings of the Institution of Mechanical Engineers, Part B: Journal of Engineering Manufacture, 217(12), 1641–1650. https://doi.org/10.1243/095440503772680578

Webster, S., Wolff, S., Bennett, J., Sun, T., Cao, J., & Ehmann, K. (2021). Porosity Formation and Meltpool Geometry Analysis Using High-speed, in situ Imaging of Directed Energy Deposition. 25(Suppl 2), 2556–2557. https://doi.org/10.1017/S1431927619013515

Wen, S. Y., Shin, Y. C., Murthy, J. Y., & Sojka, P. E. (2009). Modelling of coaxial powder flow for the laser direct deposition process. International Journal of Heat and Mass Transfer, 52(25–26), 5867–5877. https://doi.org/10.1016/j.ijheatmasstransfer.2009.07.018

Wolff, S. J., Webster, S., Parab, N. D., Aronson, B., Gould, B., Greco, A., & Sun, T. (2021). In-situ Observations of Directed Energy Deposition Additive Manufacturing Using High-Speed X-ray Imaging. Jom, 73(1), 189–200. https://doi.org/10.1007/s11837-020-04469-x

Wolff, S. J., Wu, H., Parab, N., Zhao, C., Ehmann, K. F., & Sun, T. (2019). In - situ high-speed X-ray imaging of piezo-driven directed energy deposition additive manufacturing. Scientific Reports, June 2018, 1–14. https://doi.org/10.1038/s41598-018-36678-5

Wong, K. V., & Hernandez, A. (2012). A Review of Additive Manufacturing. ISRN Mechanical Engineering, 2012, 1–10. https://doi.org/10.5402/2012/208760

Xibao, W., & Hua, L. (1998). Metal powder thermal behaviour during the plasma transferred-arc surfacing process. Surface and Coatings Technology, 106(2–3), 156–161. https://doi.org/10.1016/S0257-8972(98)00521-0

Xu, J., Gu, X., Ding, D., Pan, Z., & Chen, K. (2018). A review of slicing methods for directed energy deposition-based additive manufacturing. Rapid Prototyping Journal, 24(6), 1012–1025. https://doi.org/10.1108/RPJ-10-2017-0196

Zekovic, S., Dwivedi, R., & Kovacevic, R. (2007). Numerical simulation and experimental investigation of gas-powder flow from radially symmetrical nozzles in a laser-based direct metal deposition. International Journal of Machine Tools and Manufacture, 47(1), 112–123. https://doi.org/10.1016/j.ijmachtools.2006.02.004

Zhang, Y., Jarosinski, W., Jung, Y. G., & Zhang, J. (2018). Additive manufacturing processes and equipment. In Additive Manufacturing: Materials, Processes, Quantifications and Applications. Elsevier Inc. https://doi.org/10.1016/B978-0-12-812155-9.00002-5

Zhang, Y., Wu, L., Guo, X., Kane, S., Deng, Y., Jung, Y. G., Lee, J. H., & Zhang, J. (2018). Additive Manufacturing of Metallic Materials: A Review. Journal of Materials Engineering and Performance, 27(1), 1–13. https://doi.org/10.1007/s11665-017-2747-y

Zikin, A., Ilo, S., Kulu, P., Hussainova, I., Katsich, C., & Badisch, E. (2012). Plasma transferred arc (PTA) hardfacing of recycled hard metal reinforced nickel-matrix surface composites. Medziagotyra, 18(1), 12–17. https://doi.org/10.5755/j01.ms.18.1.1334